Charles University

Faculty of Science

Department of Physical and Macromolecular Chemistry

Study program: Macromolecular Chemistry

Doctoral Thesis

Macromolecular avenues for the creation of bio-inspired hierarchically structured surfaces

MSc. Yu-Min Wang

Supervisor: Ing. Ognen Pop-Georgievski, Ph.D.

Advisor: Ing. Andrés de los Santos Pereira, Ph.D.

Institute of Macromolecular Chemistry,

Academy of Sciences of the Czech Republic

Prague 2024

Univerzita Karlova

Přírodovědecká fakulta

Katedra fyzikální a makromolekulární chemie

Studijní program: Makromolekulární chemie

DISERTAČNÍ PRÁCE

Makromolekulární cesty k přípravě bio-inspirovaných hierarchicky strukturovaných povrchů

MSc. Yu-Min Wang

Školitel: Ing. Ognen Pop-Georgievski, Ph.D.

Konzultanti: Ing. Andrés de los Santos Pereira, Ph.D.

Ústav makromolekulární chemie,

Akademie věd České republiky, v.v.i

Praha 2024

Tímto prohlašuji, že jsem tuto disertační práci zpracovala samostatně pod vedením Ing. Ognen Pop-Georgievski, PhD. a že jsem uvedla všechny použité informační zdroje a literaturu.

Tato práce ani její podstatná část nebyla předložena k získání jiného nebo stejného akademického titulu.

Hereby I declare that this Thesis describes my original work that has been done by myself under the supervision of Dr. Ognen Pop-Georgievski. To the best of my knowledge, I have cited all used information sources and relevant literature.

This work has not been submitted to obtain any other degree, diploma, or qualification.

MSc. Yu-Min Wang

Acknowledgement

I am profoundly grateful to my supervisor, Dr. Ognen Pop-Georgievski, and my advisor, Dr. Andres de los Santos Pereira, for their invaluable guidance and mentorship throughout my PhD thesis research. Their expertise and unwavering support have been instrumental in advancing my skills and knowledge in my field of study.

I extend my sincere appreciation to my colleagues at the Institute of Macromolecular Chemistry, Czech Academy of Sciences. Special thanks go to Dr. Jan Svoboda for his assistance with XPS analysis, Dr. Radoslava Sivkova for her help with FTIR measurement, and my classmate, Ms. Iryna Romanenko, and Mr. Diego Dorado Daza for their invaluable support in the laboratory.

For the projects involving single-molecular force spectroscopy, electro-kinetics and neutron-reflectometry, I am indebted to Dr. Anna Kálosi, Dr. Juriy Halahovets, Dr. Ralf Zimmerman and Dr Tzu-Yen Huang for their support in conducting detailed and comprehensive measurements and analyses. Ms. Wan-Ting Hsu, Dr. Ilya Kotelnikov and Dr. Vladimir Proks are acknowledged for their help with the PNA's synthesis. Dr. Tomáš Riedel is acknowledged for performing the blood compatibility tests.

Additionally, for the 3D printing project, I express my gratitude to prof. Sandra Van Vlierberghe and her group members at the Polymer Chemistry and Biomaterials Group in Ghent University for their support during my internship. I acknowledge prof. Dan Jirak for the MRI analysis and imaging of performed materials.

I also wish to acknowledge the contributions of Dr. Maxym Buryi and Dr. Neda Neykova from the Institute of Physics, Czech Academy of Sciences, towards enhancing our understanding of inorganic materials through their collaboration on the project of sensing materials. Their expertise and collaboration have been invaluable to the progress of our research.

The results obtained during my PhD studies were financially supported by Charles University Grant Agency (GAUK; Project No. 2600-243-251963), Czech Science Foundation (GACR; Contract No. 22-02836S S and 22-27329S), and the project "National Institute for Cancer Research (Programme EXCELES, ID Project No. LX22NPO5102) - funded by the European Union - Next Generation EU".

Table of Contents

List of Abbreviations and Symbols

AFM-SMFS	Atomic force microscopy based single molecule force spectroscopy
AIBN	Azobisisobutyronitrile
AOI	Angle of incidence
ATRP	Atom transfer radical polymerization
BiPy	Bipyridyl
Br-silane	(11-(2-Bromo-2-methyl)propionyloxy)undecyltrichlorosilane
CAD	Computer-aided design
CBMAA	(3-Methacryloylamino-propyl)-(2-carboxy-ethyl)-dimethyl-ammonium (carboxybetaine methacrylamide)
CRP	Controlled radical polymerization
CTA	Chain-transfer agent
CuBr	Copper(I) bromide
D	Packing distance
DCM	Dichloromethane
DI	Deionized
DFEA	*N*-(2,2-difluoroethyl)acrylamide
DMF	Dimethylformamide
DP	Degree of polymerization
DLP	Digital Light Processing
DMSO	Dimethyl sulfoxide
dn/dc	Refractive index increment
$Đ$	Dispersity
GAATR	Grazing angle attenuated total reflection
Fbg	Human fibrinogen
FTIR	Fourier-transform infrared spectroscopy
GASR	Grazing angle specular reflection
GF	Grafting-from
GS	Good solvent

GT	Grafting-to
h_{dry}	Thickness at dry state
$h_{swollen}$	Thickness at swollen state
HBP	Human blood plasma
HCl	Hydrochloric acid
HEMA	2-hydroxyethyl methacrylate
HPMA	N-(2-hydroxypropyl) methacrylamide
HSA	Human serum albumin
l_c	Contour length
LiCl	Lithium chloride
l_p	Persistence length
MACl	Methacryloyl chloride
MEA	Multiple environment approach
$M_{n,\,sur}$	Surface number average molar mass
$M_{n,\,sol}$	Solution number average molar mass
N_A	Avogadro constant
NaN_3	Sodium azide
$NaHCO_3$	Sodium hydrogen carbonate
Na_2SO_4	Sodium sulfate
NMR	Nuclear magnetic resonance
NMP	Nitroxide-mediated polymerization
PBS	Phosphate-buffered saline
PET-RAFT	Photoinduced electron/energy transfer RAFT polymerization
PNAs	Peptide nucleic acids
PS	Poor solvent
R_g	Radius of gyration
RAFT	Reversible addition-fragmentation chain-transfer
SAMs	Self-assembled monolayers
SE	Spectroscopic ellipsometry

SEC-MALS	Size exclusion chromatography equipped with multiple angle laser light scattering
SI	Surface-initiated
SPR	Surface plasmon resonance
σ	Grafting density
TEA	Triethylamine
THF	Tetrahydrofuran
TCP	tissue culture plate
UV	Ultraviolet
VA-044	4,4-azobis[2-(imidazolin-2-yl) propane] dihydrochloride
WLC	Worm-like chain
XPS	X-ray photoelectron spectroscopy
3D printing	Three-dimensional printing

Abstract

Biomedical applications often rely on surface adherent architectures such as polymer brushes to prevent adverse nonspecific interactions between materials used in biomedicine and contacting biological fluids. Commonly, “grafting-to” (GT) and “grafting-from” (GF) methods are used to attain the polymer brush architecture on various surfaces. This study investigates the grafting density and antifouling effectiveness of poly[*N*-(2-hydroxypropyl) methacrylamide] (poly(HPMA)) brushes synthesized via reversible addition-fragmentation chain-transfer (RAFT) polymerization, employing both GT and GF techniques.

To determine the molar masses of solution-born and GF poly(HPMA), size exclusion chromatography (SEC) equipped with multiple angle laser light scattering (MALS) and atomic force microscopy (AFM)-based single-molecule force spectroscopy (SMFS) were combined and thoroughly used. Furthermore, the impact of solvent effects on polymer brush propagation kinetics during the concomitant surface-initiated- (SI-) RAFT process between surface and solution was investigated. Experimental findings revealed discrepancies between GF and solution-born poly(HPMA) chains. Notably, solvent composition influenced both the propagation rate and the inferred grafting density of surface-grafted poly(HPMA) due to variations in polymer swelling states attributed to hydrogen bonding.

Building upon established methodologies involving SEC-MALS and AFM-SMFS, along with investigations into the effects of solvent properties on SI-RAFT polymerization, this thesis expands further. Notable additions include: (1) probing the density profile distribution of polymer brushes utilizing neutron reflectometry and electrokinetic methods; (2) exploring the effects of various physical parameters of polymer brushes on hemocompatibility, such as controlling the degree of polymerization and initial grafting density, alongside developing hierarchical structures and biomarker conjugation; (3) advancing biomaterial development through the fabrication of hybrid materials containing antifouling polymer segments via digital light processing to synthesize MRI traceable hydrogel materials of high biocompatibility, thus broadening avenues in biomaterials research.

Abstrakt

Pro potlačení nežádoucích nespecifických interakcí mezi materiály používanými v biomedicínských aplikacích a biologickými tekutinami se často využívá pokrytí jejich povrchu polymerními kartáči. Modifikaci je možnou provést metodou "roubování na" (GT) nebo "roubování z" (GF). Tato práce se zabývá studiem hustoty roubování a účinnosti proti zanášení u poly[*N*-(2-hydroxypropyl) methakrylamidových] (poly(HPMA)) kartáčů syntetizovaných pomocí polymerace s vratným adičně-fragmentačním přenosem řetězce (RAFT) s využitím technik GT i GF.

Ke stanovení molárních hmotností poly(HPMA) připraveného v roztoku a na povrchu byla kombinována a důkladně využita rozměrově vylučovací chromatografie (SEC) vybavená více úhlovým detektorem rozptylu světla (MALS) a silová spektroskopie jedné molekuly (SMFS) založená na mikroskopii atomárních sil (AFM). Dále byl zkoumán vliv rozpouštědla na kinetiku růstu polymerních kartáčů během povrchově iniciované polymerizace (SI-RAFT). Byly experimentálně zjištěny rozdíly mezi řetězci poly(HPMA) narostlými z povrchu a vzniklými v roztoku. Zejména složení rozpouštědla ovlivnilo rychlost propagace i odvozenou hustotu roubování z povrchu narostlého poly(HPMA) v důsledku změn v botnání polymeru, které se připisují vodíkovým vazbám.

Tato práce využívá kombinace metod SEC-MALS a AFM-SMFS pro studium polymerace SI-RAFT se zahrnutím vlivu rozpouštědla a dále na ně navazuje. Významné rozšíření zahrnuje: (1) studium rozložení hustotního profilu polymerních kartáčů pomocí neutronové reflektometrie a elektrokinetických metod; (2) zkoumání vlivu různých fyzikálních parametrů polymerních kartáčů na hemokompatibilitu, jako je stupeň polymerizace a počáteční hustota roubování, změna jejich hierarchické struktury a konjugace biomarkerů; (3) pokrok v přípravě hybridních biomateriálů obsahujících polymerní kartáče pomocí 3D tisku za účelem syntézy hydrogelových materiálů s vysokou biokompatibilitou sledovatelných magnetickou rezonancí.

List of publications and contributions at conferences

Publications included into this Thesis

1. **Wang, Y.**; Kálosi, A.; Halahovets, Y.; Romanenko, I.; Slabý, J.; Homola, J.; Svoboda, J.; de los Santos Pereira, A.; Pop-Georgievski, O. Grafting density and antifouling properties of poly[*N*-(2-hydroxypropyl) methacrylamide] brushes prepared by "grafting to" and "grafting from". *Polym. Chem.*, 2022, *13, 3815-3826* (Impact Factor: 4.6)

   https://doi.org/10.1039/D2PY00478J

2. **Wang, Y.**; Kálosi, A.; Halahovets, Y.; Beneš, H.; de los Santos Pereira, A.; Pop-Georgievski, O. Solvent Effects on Surface-grafted and Solution-born poly[*N*-(2-hydroxypropyl) methacrylamide] during Surface-initiated RAFT Polymerization. *Polymer Chemistry,* 2024 (Impact Factor: 4.6)

   Manuscript under major revision (PY-ART-02-2024-000177)

Publication not included into this Thesis

1. Buryi, M.; Neykova, N.; Brik, M. G.; **Wang, Y.**; Remeš, Z.; Ridzoňová, K.; Babin, V.; Davydova, M.; Drahokoupil, J.; Chertopalov, S.; Landová, L.; Pop-Georgievski, O. Hydrothermally grown molybdenum doped ZnO nanorod arrays. The concept of novel ultrafast nanoscintillator. *Optical Materials*, 2023, 145, 114445 (Impact Factor: 3.9)

   https://doi.org/10.1016/j.optmat.2023.114445

2. Buryi, M.; Babin, V.; Neykova, N.; **Wang, Y.**; Remeš, Z.; Ridzoňová, K.; Dominec, F.; Davydova, M.; Drahokoupil, J.; Chertopalov, S.; Landová, L.; Pop-Georgievski, O. Changes to Material Phase and Morphology Due to High-Level Molybdenum Doping of ZnO Nanorods: Influence on Luminescence and Defects. *Materials*, 2023, 16 (9), 3294 (Impact Factor: 3.4)

   https://doi.org/10.3390/ma16093294

Contributions at international conferences

Poster presentations:

1. **Wang, Y.**; Kálosi, A.; Halahovets, Y.; Romanenko, I.; Slabý, J.; Homola, J.; Svoboda, J.; de los Santos Pereira, A.; Pop-Georgievski, O. Grafting-To vs. Grafting-From: The Influence of Methodological Approach to the Antifouling Brushes of poly[N-(2-Hydroxypropyl) Methacrylamide], European Polymer Congress, Czechia, 2022

2. **Wang, Y.**; Kálosi, A.; Halahovets, Y.; Romanenko, I.; Slabý, J.; Homola, J.; Svoboda, J.; de los Santos Pereira, A.; Pop-Georgievski, O. Poly[N-(2-Hydroxypropyl) Methacrylamide] Brushes Prepared by Grafting-to and Grafting-from: The Influence of Grafting Methods to Antifouling Properties, Bordeaux Polymer Conference, France, 2022

3. **Wang, Y.**; Kálosi, A.; Halahovets, Y.; Romanenko, I.; Slabý, J.; Homola, J.; Svoboda, J.; de los Santos Pereira, A.; Pop-Georgievski, O. Grafting-To vs. Grafting-From: Grafting Density and Fouling Resistance of Poly(HPMA) Brushes, 17th Dresden Polymer Discussion, Germany, 2021

1. Introduction

1.1. Motivation

The interaction between artificial materials/devices and biological environment (referred to as "fouling") is a critical consideration in the research of medical devices and biomaterials. The phenomenon of fouling poses significant challenges and potential risks when medical devices and biomaterials materials come into contact with biological fluids like urine, blood, or blood plasma, involving the adsorption of biomolecules, cell adhesion, and the formation of biofilms (see Figure 1).

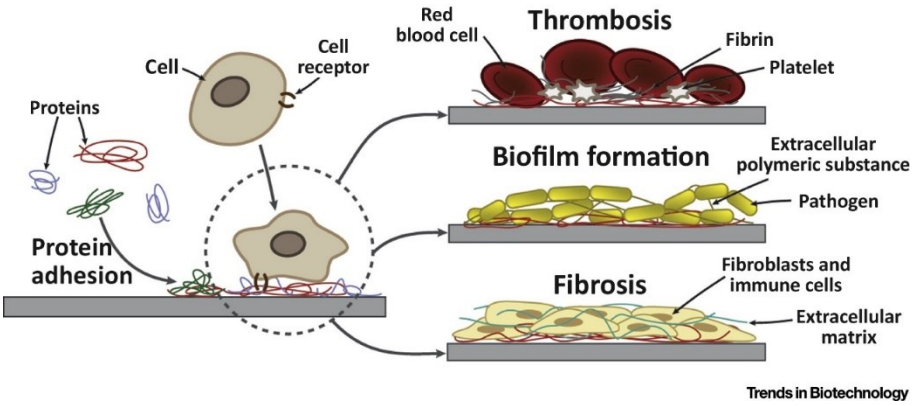

Figure 1: Illustration of the biological fouling of materials in medical devices, along with potential responses, including thrombosis, biofilm formation, and fibrosis. [1]

Controlling or even completely suppressing fouling is crucial in the development of various medical technologies, including microfluidic devices, artificial implants, biosensors, and drug delivery systems. In particular medical applications, the complications arising from fouling can be severe, including infections, inflammation, blood clotting, and thrombus formation (see Figure 2). These complications not only endanger patient lives but also jeopardize the efficacy and safety of the medical devices. To mitigate these risks, materials that efficiently inhibit the non-specific binding from biological environment (referred to as "antifouling materials") are urgently desired and needed. By developing materials with improved resistance to fouling, the performance, safety and endurance of medical devices can be significantly enhanced.

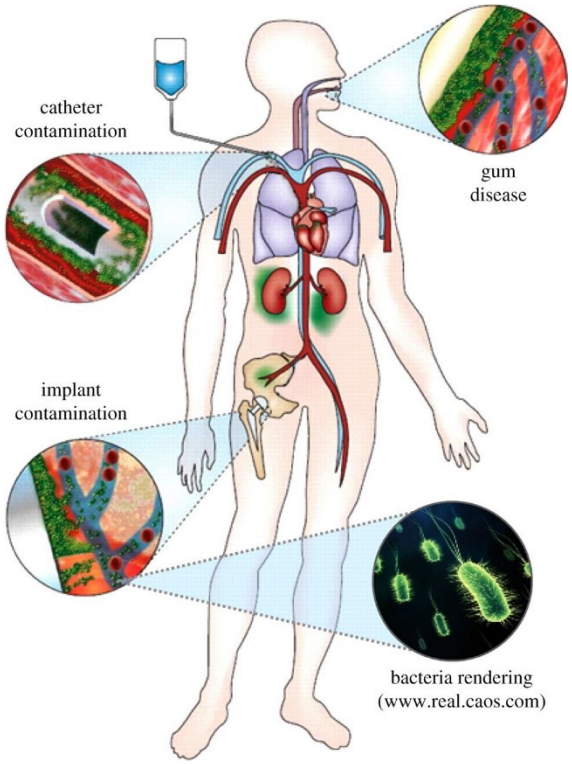

Figure 2: Diagram identifying body regions prone to infectious biofilms. [2]

Antifouling coatings play a crucial role in diverse biomaterials and clinical applications. They are important for preventing the adhesion of biological substances ensuring the effectiveness and safety of numerous medical devices and implants. [3] Specifically, within the domain of implants and prosthetics, these materials are utilized to prevent the attachment of cells and proteins, thereby lowering the risk of complications such as infections and inflammation. The application of antifouling coatings substantially improves the biocompatibility of implanted devices, thereby facilitating their successful integration within the body.

Aside from implants, catheters, and different medical tubes, antifouling materials also prove advantageous in their incorporation. These materials play a crucial role in reducing the accumulation of biological substances, thereby reducing the risk of blockages, infections, and complications that may arise from prolonged usage. Moreover, antifouling technologies are utilized in dental implants and devices located in the oral cavity to prevent the attachment of bacteria and other contaminants. This, in turn, contributes to oral health and prolongs the durability of dental prosthetics. Additionally, antifouling materials also find application in diagnostic tools, including biosensors, microfluidic devices, lab-on-chip, and imaging equipment. Coating surfaces

with antifouling materials prevents the interference of biological substances, ensuring the accuracy and reliability of diagnostic results. Drug delivery systems can also benefit from antifouling coatings, preventing unwanted binding of proteins or cells and facilitating efficient and targeted pharmaceutical delivery. Ophthalmic devices, wound dressings, and surgical instruments round out the spectrum of medical applications, with antifouling properties contributing to a clean healing environment, reduced risk of infections, and enhanced instrument hygiene during medical procedures. The incorporation of antifouling materials in these diverse medical applications underscores their significance in advancing patient care, device functionality, and overall healthcare outcomes.

Various strategies are employed to create antifouling materials, including surface modifications, polymer coatings, the use of biomimetic approaches and/or synthesis of bulk non-fouling material, such as hydrogels. For instance, hydrophilic materials are particularly promising in preventing fouling by repelling proteins and biomolecules due to the free energy associated with the fouling process. The enthalpic barrier, which refers to the energy penalty experienced when water molecules are removed from a hydrophilic layer upon protein adsorption, plays a critical role in deterring the attachment of biomolecules. This property generally makes hydrophilic organic surfaces less prone to fouling.

Self-assembled monolayers (SAMs) with hydrophilic headgroups are one of such examples of surface modifications that have shown efficacy in reducing the adsorption of individual proteins from simpler model solutions. [4-6] SAMs are organized molecular assemblies formed spontaneously on a substrate, presenting a tailored surface. However, their antifouling effectiveness may diminish when facing the complexity and high protein content of blood plasma or other biological fluids. The challenges associated with using hydrophilic coatings of SAMs in complex biological environments like blood plasma are substantial and multifaceted arising from diverse array of proteins, protein adsorption competition, and dynamic nature of biological fluids. [6, 7]

Surface-grafted polymer chains (referred to as polymer coatings) have emerged as one of the most effective strategies to combat fouling from blood plasma. [8-13] These polymer coatings offer advantages in terms of versatility, tunability, and ability to create surfaces with tailored properties. Generally, polymer coatings can be applied through various techniques like direct surface grafting via physisorption or chemisorption, layer-by-layer deposition, or surface-initiated (SI)

polymerization to create surfaces resistant to fouling. In particular, SI polymerization allows polymer chains to form directly from the surface which offers excellent control over the coating's thickness, structure, and other physical properties, providing a robust and tailored antifouling surface. [14]

The objective of this thesis is to develop grafting methods and surface initiated (SI) polymerizations, comprehend their physical and chemical intricacies, aiming to establish robust and enduring antifouling strategies for medical devices that come into contact with blood. Through a detailed examination of these mechanisms, influencing factors, and characterization techniques, this research seeks to develop polymer coatings that effectively resist protein adsorption, deter cell attachment, and hinder biofilm formation on surfaces of blood-interacting medical devices. Moreover, the research on antifouling materials is positioned as a promising strategy for biomaterials in clinical applications. Beyond the application of antifouling coatings, an emerging trend involves the fusion of biomimetics with antifouling capabilities, introducing a novel approach to the broad field of biomedicine.

1.2. Surface-grafted polymer chains (Polymer coatings)

Grafting polymer chains onto surfaces is a prevalent method to create antifouling materials. The immobilization of polymer chains to a surface create an entropic barrier that inhibits the adhesion of biomolecules like proteins, bacteria, or other organisms. The entropic barrier is connected to the restricted conformational freedom of the surface-grafted polymer chains upon biomolecule adsorption, and thus the adsorption processes encounters reduced available space due to the constrained movement of the chains. [15-17] As a result, the biomolecule finds it thermodynamically unfavored to adhere to the polymer surface which effectively reduces or prevents the fouling. [18-23]

This entropic penalty acts as a deterrent against fouling. Thus, by increasing the energy required for biomolecules to overcome the entropic barrier and adhere to the surface, we can achieve better fouling prevention. Therefore, the design of antifouling materials often involves controlling the physical and macromolecular properties of these immobilized polymer chains to optimize the entropic barrier and enhance their effectiveness in repelling or resisting fouling by biomolecules. Moreover, combining the entropic barrier with the enthalpy barrier in the presence of hydrophilic polymer chains could form a multifaceted defense mechanism against fouling. The careful tuning of polymer properties and understanding the thermodynamics involved are essential for the

successful design of effective antifouling materials. [24-27]

1.2.1. Grafting methods

In general, grafting methods for attaching polymer chains to surfaces can be broadly categorized into two main approaches: “grafting-to” and “grafting-from” methods. These methods differ in how the polymer chains are attached or introduced to the surface (see Figure 3). [28-32]

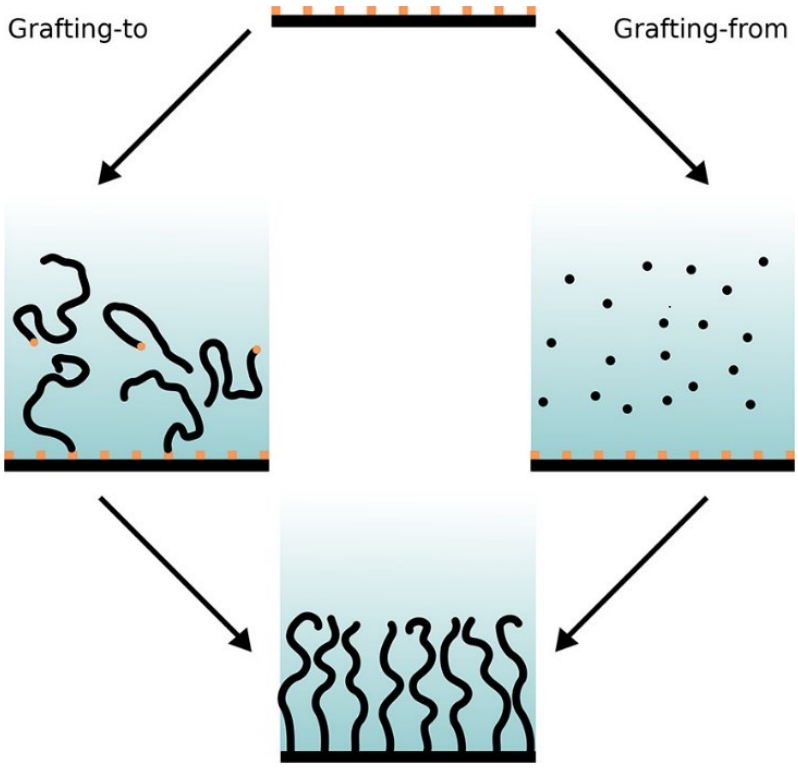

Figure 3. Illustration of the two broad strategies to synthesize surface-grafted polymer chains as grafting-to (left) and grafting-from (right). [33]

1) Grafting-to approach:

In this approach, pre-synthesized polymer chains with reactive end-groups are physically attached or chemically immobilized onto the surface. This method involves the direct attachment of pre-synthesized polymers onto the surface, forming a layer of polymer chains. Common techniques for this process include the use of direct grafting of polymer chains through functional groups (such as: thiol or silane) [34], click reactions, supramolecular chemistry, and pre-coating with anchoring layers (such as: polydopamine, polyglycidyl methacrylate, isocyanates, etc). [35-38]

The advantages of this method are having the known molar mass and dispersity of the pre-made polymer chains and the relatively simple grafting process compared to the grafting-from method. However, the structure of the surface-grafted polymer chains may not be as densely packed as those obtained from the grafting-from method (explained at Section 1.2.1(2)).

2) Grafting-from approach:

Contrary to the grafting-to method, the grafting-from approach involves initiating the polymerization reaction directly from the surface. Here, the surface itself acts as a substrate for the initiation of polymerization. Typically, this involves anchoring initiators or reactive molecules onto the surface, followed by the initiation of polymerization reactions. [10] Polymer chains are then formed directly from these initiator sites, resulting in chains that are covalently attached to the surface. Grafting-from method often leads to surface-grafted polymer chains that are densely packed and have a well-defined structure.

Nevertheless, the grafting-from method typically involves a more stringent and controlled process compared to the grafting-to method. The condition for the initiation and subsequent polymerization needs to be carefully controlled to achieve the desired structure and properties of the surface-grafted polymer chains synthesized via GF. Techniques utilized in SI polymerization often hinge on controlled radical polymerizations (CRP) like nitroxide-mediated polymerization (NMP), [39-41] atom-transfer radical polymerization (ATRP), [42-47] and RAFT polymerization[48-53]. Notably, SI-RAFT polymerization is garnering heightened interest owing to its favorable characteristics, including outstanding monomer compatibility and the absence of metal catalysts that could be toxic to cells. This makes it particularly advantageous for applications in biomaterials.

However, using SI polymerization proves to be more challenging than the grafting-to process, primarily due to the stringent regulation of conditions. Additionally, obtaining the molar mass and dispersity of surface-grafted polymer chains prepared by SI polymerization can be challenging. This arises from the difficulty of collecting a sufficient amount of GF polymer chains after cleavage from the supporting substrate for size exclusion chromatography (SEC) measurement due to the limited quantities of polymer that can be obtained from the thin layer. The challenges associated with measuring the molar mass and dispersity highlight the need for

specialized techniques or adaptations when characterizing surface-grafted polymers prepared by grafting-from method.

In the face of these challenges, the grafting-from method remains pivotal in scenarios where the attainment of a precisely regulated and densely layered polymer surface is essential. Therefore, the implementation of a combination of analytical methods, such as single-molecule force spectroscopy (SMFS), electrokinetics (EK), and neutron reflectometry (NR), becomes paramount. This approach proves instrumental in surmounting measurement hurdles and gaining valuable insights into the intrinsic characteristics of surface-grafted polymers prepared via SI-RAFT.

As a short summary we can say that each of the mentioned grafting methods has its advantages and limitations. The grafting-to method allows for better control over the chemical and macroscopic characteristics of the polymer chains before attachment to the surface. On the other hand, the grafting-from method often provides better control over the density, length, and orientation of the grafted polymer chains on the surface. In practical applications, the trade-off between the simplicity of the grafting process and the desired structure of the grafted polymer chains should be carefully considered. Both methods have their advantages and limitations, and the selection depends on the specific goals and constraints of the intended use.

1.2.2. Structure and physical parameters

The conformations of surface-grafted polymer chains can be classified into different structures based on their physical parameters. [54-57] The terms “pancake-like”, “mushroom-like”, and “brush-like” are used to describe these conformations, and they are defined by the distance between two adjoining/neighboring chains (referred to as “packing distance”, D) and the density of polymer chains per area (referred to as “grafting density”, σ) on the surface. The grafting density (calculated by Equation 1) and the packing distance between grafting sites supposing hexagonal packing (calculated by Equation 2) were estimated utilizing the layer thickness in the dry state (h), the bulk density (ρ), the Avogadro constant (N_A), and the number-average molar mass of surface-grafted polymer chains (M_n).

$$\sigma = \frac{h\rho N_A}{M_n} \qquad \text{(Equation 1)}$$

$$D = \sqrt{\frac{2}{\sqrt{3}\sigma}}$$ (Equation 2)

1) Pancake-like and Mushroom-like:

The formula $\frac{D}{2R_g}$ is commonly used to define the structure of surface-grafted polymer chains which the R_g represents the radius of gyration. When $\frac{D}{2R_g} > 1.0$, it indicates that the packing distance between the polymer chains is significantly larger than its radius of gyration. This condition implies that the polymer chains are relatively flat in a "pancake-like" or "pancake-like" shape. Consequently, they retain a more disordered, entangled state, which maximizes their entropy.

When a small number of polymer chains are attached to a surface, there is considerable spacing between them. This sparse arrangement allows the chains to adopt a flat orientation, resembling a structure either "pancake-like" or "mushroom-like". The distinction between these two configurations can be discerned through the interaction or interference among the surface-grafted chains. In the "pancake-like" conformation, the density of surface-grafted polymer chains is insufficient to support them standing away from the surface. Consequently, there is a significant interaction between the surface and grafted chains. In the "mushroom-like" structure, the density of surface-grafted polymer chains is higher than in the "pancake-like" scenario. However, the chains are still unable to fully extend away from the surface, preventing substantial overlap or interpenetration between neighboring chains. This arrangement gives the appearance of a mushroom-like shape, with the chains extending outward from the surface while maintaining noticeable interaction with nearby chains.

2) Mushroom-to-brush transition:

The condition of $\frac{D}{2R_g} = 1.0$ represents a critical point known as the mushroom-to-brush transition. It implies that the packing distance between the polymer chains is equal to twice its radius of gyration. At this point, the chains undergo a transition from a mushroom-like conformation to a brush-like conformation when considering their arrangement and interaction near the surface.

3) Brush-like:

When the value of $\frac{D}{2R_g} < 1.0$, it indicates that the chains are stretched away from the surface and tend to adopt a brush-like conformation. In this scenario, the chains experience less spatial expansion or lateral extension relative to their radius of gyration.

The brush conformation occurs when the density of surface-grafted polymer chains is high enough to prevent significant chain overlap or interpenetration. In this conformational structure, the chains extend away from the surface, resembling the bristles of a brush. Each chain remains relatively independent and experiences minimal interaction with neighboring chains due to the dense and extended configuration.

These classifications are primarily based on parameters such as grafting density, chain length, and the packing distance between neighboring chains (see Figure 4). The physical characteristics and behavior of these surface-grafted polymer chains, including their ability to resist fouling or interact with biomolecules, can vary significantly based on their conformation. The choice of conformation is often tailored to achieve specific surface properties and functionalities required for various applications, such as antifouling surfaces, biomaterials, or marine coatings.

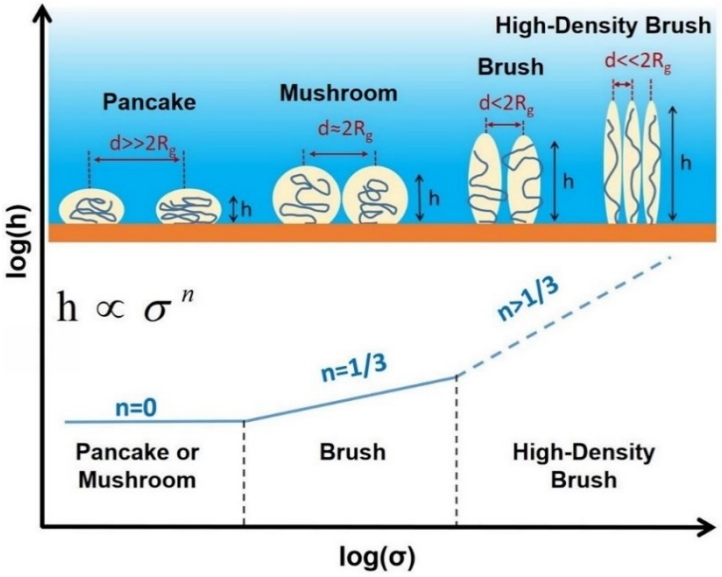

Figure 4. Illustration of the conformations of surface-grafted polymer chains and the relationship between the chain conformation and their physical parameters described using the hypothesis of Alexander-de Gennes. [58]

1.2.3. Influencing factors

The physical properties of polymer chains grafted onto surfaces undergo complex molding influenced by a variety of factors, particularly within the context of different grafting methodologies. The specific choice of grafting method plays a crucial role in determining how various influencing factors impact the characteristics of these grafted polymer chains. In essence, the method chosen for grafting directly shapes and defines the outcome of the interactions between the polymer chains and the surface, reflecting a nuanced interplay of numerous contributing elements.

In the "grafting-to" method, it is crucial to consider limitations arising from both kinetic and thermodynamic aspects. As the surface coverage by pre-synthesized polymer chains increases, there is a notable concentration disparity between the interface and the solution, with a significantly higher concentration of polymer chains at the interface. This increased concentration poses a challenge for additional polymer chains in the solution, as they must diffuse against a concentration gradient created by the already-grafted chains on the surface. This results in a noticeable slowdown of the grafting process. Thermodynamic constraints come into play when attempting to attach extra chains to a densely packed surface. Specifically, as the grafting density of the surface-grafted polymer chains increases, they are compelled to adopt a stretched conformation due to strong excluded volume interactions, which is thermodynamically unfavorable. Consequently, this grafting-to method commonly yields a relatively thinner film, particularly with a longer reaction time needed for the film to be formed. In a broader sense, improving the process involves reducing the steric hindrance between the individual pre-synthesized polymers. This can be potentially achieved by adjusting factors such as reaction temperature, solvent conditions (whether they are good or poor solvents), the inter/intra-interactions among polymer chains and surface, and the execution of the reaction through a melt process. [34, 35, 37, 38, 59]

On the other hand, in the "grafting-from" approach, the density of initiator molecules, polymerization conditions, and monomer properties play pivotal roles in determining chain length, density, and overall layer physical parameters. Additional contributors include substrate material, surface pre-modification, and chain growth process, which impact the interaction between the substrate and grafted polymer chains. Factors like density of grafting sites, solvent condition, and

swelling behavior also wield influence over the ultimate conformation and properties of the grafted layer. [60-62] The attainment of desired physical characteristics mandates meticulous consideration and optimization of these multifaceted factors throughout the grafting process. Such a nuanced approach is imperative for tailoring surface-grafted polymer chains to specific applications, encompassing features like antifouling properties, biocompatibility, lubrication, and wettability.

1.3. Outline of RAFT polymerization

RAFT polymerization, a type of reversible-deactivation radical polymerization, belongs to a category of techniques that utilize a RAFT agent (as known as chain-transfer agent, CTA), specifically a thiocarbonylthio compound. This method provides control over the molecular weight and dispersity (*Đ*) in free-radical polymerization processes. Discovered in 1998 at the Commonwealth Scientific and Industrial Research Organisation in Australia, RAFT polymerization is part of a broader class of living or controlled radical polymerization (CRP) techniques, including ATRP and NMP. [63-65] Utilizing thiocarbonylthio compounds like dithioesters, , and xanthates, RAFT polymerization mediates polymerization through a reversible chain-transfer process. [66-69] Similar to other CRP techniques, RAFT polymerizations can be conducted under conditions favoring low dispersity (narrow molecular weight distribution) and a predetermined molecular weight. This method proves useful for designing polymers with intricate architectures such as linear block copolymers, comb-like structures, stars, brush polymers, dendrimers, and cross-linked networks. RAFT polymerization is recognized for its broad compatibility with a diverse array of monomers, surpassing other CRP methods. These monomers encompass (meth)acrylates, (meth)acrylamides, acrylonitrile, styrene and its derivatives, butadiene, vinyl acetate, and *N*-vinylpyrrolidone. Notably, RAFT polymerization exhibits flexibility in terms of reaction parameters, such as temperature and impurity levels, in comparison to NMP or ATRP.

The RAFT mechanism is illustrated in Figure 5. After activation (step I), radical species combine with the CTA to establish an equilibrium between active and dormant species (steps III and V). The chain transfer steps, fundamental to the RAFT mechanism, are degenerate, involving a reversible transfer of the functional chain end-group (typically a thiocarbonylthio group, Z-C(=S)S-R) between dormant chains (referred to as macroCTA) and propagating radicals. In an efficient process, the rate of the addition/fragmentation equilibrium exceeds that of propagation,

resulting in less than one monomer unit added per activation cycle. Consequently, all chains exhibit a similar degree of polymerization (DP) at any given time. The overall process involves the insertion of monomers between the R- and Z-C(=S)S-groups of a RAFT agent, forming the α and ω end-group for the majority of the resulting polymeric chains.

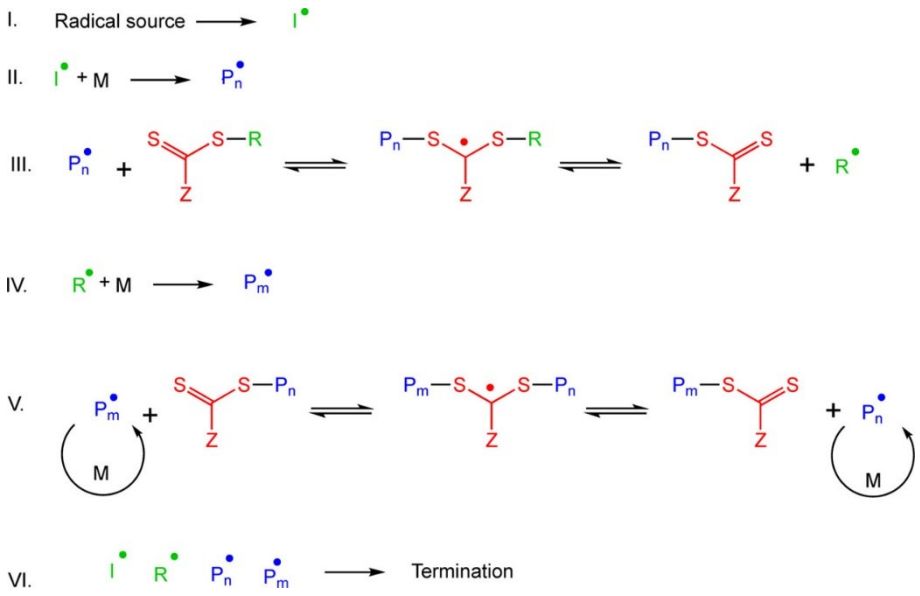

Figure 5. Suggested mechanism for reversible addition–fragmentation chain-transfer polymerization. [70]

The selection of the Z and R groups in a RAFT agent involves careful consideration. The Z group plays a crucial role in influencing the stability of the S=C bond and the adduct radical (Polymer-S-C•(Z)-S-Polymer, as presented at step V in Figure 5). These factors impact the positions and rates of elementary reactions in both the pre- and main-equilibrium phases. The R group must possess the ability to stabilize a radical, favoring the right-hand side of the pre-equilibrium, yet remain unstable enough to initiate the growth of a new polymer chain. Consequently, designing a RAFT agent requires thoughtful consideration of the monomer and temperature, as these parameters strongly influence the kinetics and thermodynamics of the RAFT equilibria.

1.4. Biomaterials

Biomaterials encompass a diverse array of materials accurately engineered to interact with biological systems for medical and/or healthcare purposes. These materials, whether synthetic or natural, are designed to fulfill specific functions within living tissues and find applications across various medical disciplines. Key attributes of biomaterials include biocompatibility, ensuring that they do not provoke adverse reactions within the body, and bioactivity, enabling them to seamlessly engage with biological systems. Whether serving structural roles by replacing or augmenting tissues and organs, contributing to drug delivery systems, or aiding in the development of diagnostic tools, biomaterials play a pivotal role in advancing medical science.

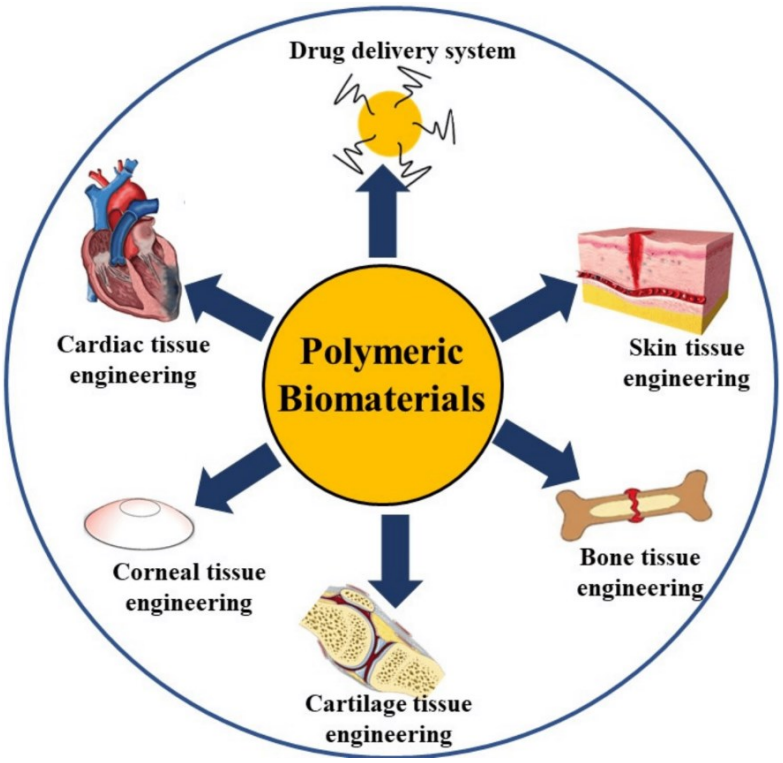

Figure 6. Illustration of diverse applications of polymeric biomaterials across various biomedical fields. [71]

Examples of biomaterials are manifold. Metal alloys like titanium and stainless steel, prized for their strength and compatibility with the human body, are prevalent in orthopedic implants. Polymers, such as polylactic acid (PLA) and polyglycolic acid (PGA), serve diverse purposes,

from sutures to drug delivery systems (see Figure 6). Additionally, ceramics like hydroxyapatite, a component of bone, and bioactive glass find applications in dental implants, bone grafts, and related medical interventions. Various composite hydrogels and cryogels assembled from ceramics and polymers present promising avenues to unite beneficial properties of both material types. These materials, alongside natural biomolecules like collagen and hyaluronic acid, contribute to the rapidly evolving field of tissue engineering applications and cosmetic procedures. The aim of biomaterial engineering is to advance medical procedures by exploring novel biomaterials and innovative applications, with a focus on improving outcomes, minimizing adverse reactions, and enhancing the overall effectiveness of medical treatments.

Furthermore, combining antifouling properties with biomaterials presents a range of advantages, particularly in fields such as medicine, tissue engineering, and biomedical application. The incorporation of antifouling characteristics in biomaterials serves as a pivotal strategy to thwart the accumulation of unwanted substances, including bacteria and fungi, on the material surface. This is particularly vital in medical contexts, where preventing infections around implants and devices is critical for patient safety. The enhanced resistance to fouling not only contributes to infection prevention but also extends the lifespan of biomaterials, ensuring their prolonged functionality within the body. Moreover, improved biocompatibility and ease of cleaning further underscore the significance of integrating antifouling properties, offering benefits that range from maintaining the original performance of biomaterials to reducing environmental impact in various applications.

An additional layer of significance lies in the versatility of antifouling strategies, ranging from surface modifications to coatings, each tailored to meet the specific needs of diverse biomaterials. As a result, these advancements contribute to the development of biomaterials that not only interact seamlessly with the body but also exhibit resilience against external contaminants. In both medical and industrial settings, this combination of antifouling properties and biomaterials not only enhances the overall performance and longevity of devices but also aligns with broader goals of improving patient outcomes and minimizing environmental impact.

The interconnection between biomaterials and the extracellular matrix (ECM) is fundamental in the realms of tissue engineering and regenerative medicine. A critical aspect of this relationship involves biomaterials replicating the composition of the ECM, with natural biomaterials such as

collagen and hyaluronic acid often chosen for their likeness to native tissue environments. This design strategy aims to create biomaterials that establish microenvironments closely resembling those found in natural tissues, fostering better integration with host tissues. Furthermore, biomaterials are engineered to facilitate cellular interactions by mimicking the signaling cues present in the ECM. This involves guiding cell attachment, migration, and differentiation, thereby influencing tissue regeneration processes.

The synergy between biomaterials and the ECM is particularly evident in tissue engineering applications which often focus on the synthesis of various scaffolds. Biomaterials not only provide a temporary support structure but also serve as a platform for cells to adhere, proliferate, and generate their own ECM. The biomaterial scaffold, designed to be biocompatible, plays a crucial role in directing tissue regeneration. As cells gradually replace the biomaterial with their own ECM, the scaffold may degrade, leaving behind a fully-formed, functional tissue. This intricate relationship underscores the importance of biomaterials closely emulating the ECM for the success of diverse biomedical applications, from implantable devices to tissue-engineered constructs.

Recent advancements in biomaterial design have been significantly influenced by the introduction of three-dimensional (3D) printing techniques. [72] The precision and efficiency offered by 3D printing technology have revolutionized the field of biomaterials, allowing for the customized fabrication of complex structures with complex geometries. This manufacturing approach enables the creation of biomaterials tailored to specific applications, such as tissue engineering, drug delivery systems, and medical implants.

3D printing facilitates the layer-by-layer deposition of materials, offering unprecedented control over the spatial distribution and composition of the biomaterial. This level of precision allows researchers and clinicians to design scaffolds and implants that closely mimic the anatomical and functional characteristics of natural tissues. Additionally, the efficiency of 3D printing accelerates the production process, making it more feasible to address individual patients' needs through personalized medicine. In conclusion, the integration of 3D printing techniques in biomaterial development has brought about a paradigm shift in the field, offering precise and efficient methods for creating tailored structures with applications ranging from regenerative medicine to advanced medical devices.

1.5. Extracellular matrix and its mimetics

The extracellular matrix (ECM) is a pivotal element within the structural framework of tissues and organs, existing outside the confines of cells. This intricate network comprises a diverse array of proteins, glycoproteins, and polysaccharides, collectively forming a dynamic and multifaceted environment. Collagen, elastin, fibronectin, and other molecules are integral components of the ECM, providing not only a physical scaffold but also actively participating in crucial cellular functions.

Collagen fibers, within the ECM, contribute to the tissue's tensile strength, while elastin confers elasticity, allowing tissues to endure mechanical stresses and regain their shape. Glycoproteins like fibronectin facilitate cell adhesion, connecting cells to the ECM and influencing cellular behavior. The dynamic interplay between these ECM components regulates essential processes such as cell signaling, migration, and differentiation. This orchestration of cellular activities by the ECM is fundamental to various biological phenomena, including tissue development, repair, and maintenance of tissue homeostasis.

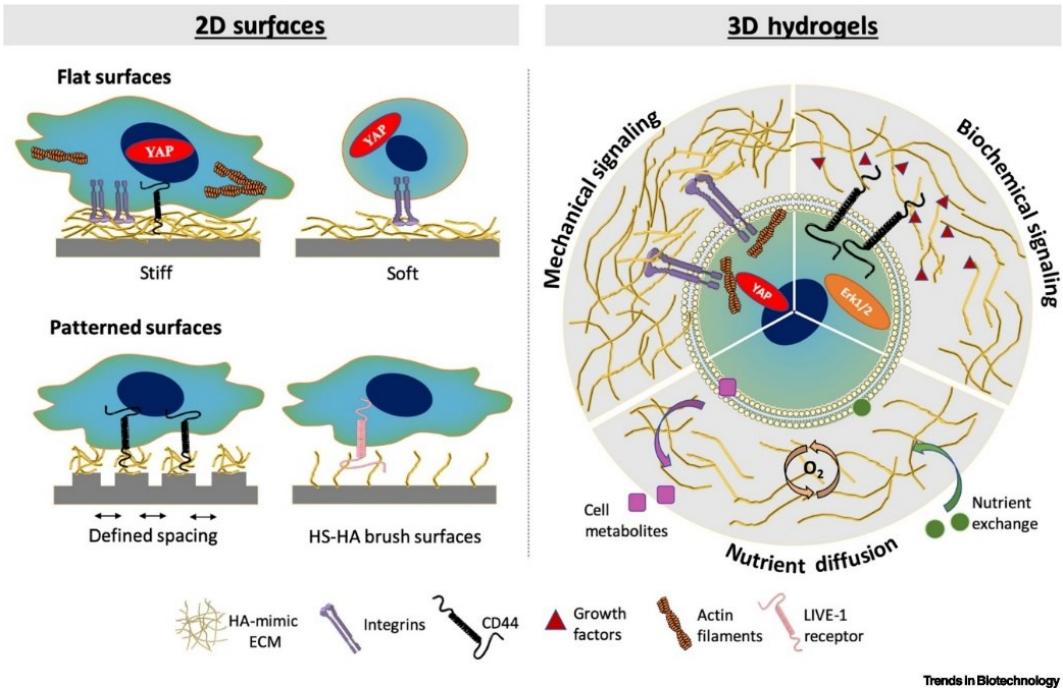

Figure 7. Illustrative diagrams delineate the utilization of 2-dimensional surfaces and 3-dimensional models in the processes of cellular immobilization and encapsulation. [73]

The profound significance of the ECM extends into fields like tissue engineering, where researchers seek to replicate its natural composition to design biomimetic scaffolds. These scaffolds aim to mimic the supportive environment of the ECM, fostering optimal conditions for cell growth and tissue regeneration (see Figure 7). As we delve into the intricate world of the extracellular matrix, its role becomes increasingly apparent in not only maintaining tissue integrity but also in dictating cellular responses in both physiological and pathological conditions.

In this research, the emulation of ECM holds paramount importance, particularly within the fields of biomaterials and tissue engineering. The primary focus of this thesis is to replicate the overall structure and function of the ECM, constructing synthetic scaffolds that accurately mirror its supportive functions while integrating antifouling capabilities. Through strategic modifications involving bioactive agents such as cell growth factors, enzymes, and peptides on the antifouling ECM scaffold, the objective is to instigate selectivity in the growth of specific cells. These pioneering antifouling ECM scaffolds, enhanced with bioagents, exhibit considerable potential for applications in regenerative medicine. The overarching objective is to create environments that not only foster optimal cell growth and tissue regeneration but also contribute to the overall preservation of tissue homeostasis.

1.6. Biomaterial fabrication using 3D printing technology

Fabrication of biomaterials through 3D printing represents a cutting-edge approach in the field of materials science and biomedical engineering. This method involves the layer-by-layer deposition of materials to create three-dimensional structures with high precision and customization. The process typically begins with computer-aided design (CAD) models that guide the 3D printer in generating intricate geometries specific to the intended application of the biomaterial. Several 3D printing methods are employed for fabricating biomaterials, each offering unique advantages in terms of resolution, material compatibility, and speed. Here are some common 3D printing methods used for biomaterial fabrication:

1) Stereolithography (SLA):

SLA utilizes a liquid photopolymer resin that solidifies when exposed to a specific wavelength of light (usually ultraviolet, UV). A laser or projector selectively cures the resin layer by layer, building up the 3D structure. SLA provides high resolution and is suitable for

producing detailed biomaterial constructs.

2) Selective Laser Sintering (SLS):

SLS employs a powdered biomaterial, often a polymer or a biocompatible ceramic. A laser selectively fuses the powder particles layer by layer, forming the desired structure. SLS is versatile and can accommodate various biomaterials, making it suitable for applications where a range of material properties is required.

3) Fused Deposition Modeling (FDM):

FDM is one of the most common 3D printing methods. It involves extruding a thermoplastic biomaterial through a heated nozzle, layer by layer, to build the 3D structure. FDM is known for its simplicity, cost-effectiveness, and ease of use. However, achieving high resolution may be challenging compared to other methods.

4) Inkjet Bioprinting:

Inkjet bioprinting operates similarly to traditional inkjet printing but uses bioinks containing living cells. The printer deposits droplets of bioink layer by layer, creating 3D structures. This method is particularly relevant for tissue engineering applications, as it allows the precise placement of cells within the biomaterial scaffold.

5) Direct Ink Writing (DIW):

DIW is a technique where a viscous bioink is extruded from a nozzle in a controlled manner to create the desired 3D structure. The method is versatile and can accommodate a wide range of biomaterials, including hydrogels and polymer blends. DIW is often used for creating intricate structures with high resolution.

6) Electrospinning:

While not a traditional 3D printing method, electrospinning is a technique that can be used to create biomaterial scaffolds. It involves the controlled deposition of polymer fibers from an electrically charged spinneret. The fibers form a scaffold with a high surface area, suitable for tissue engineering applications.

7) Volumetric Additive Manufacturing (VAM):

In contrast to conventional layer-by-layer techniques, VAM constructs 3D objects in a volumetric manner, facilitating simultaneous and uninterrupted material deposition across the entire build volume. This is accomplished by utilizing light or alternative energy sources to solidify or fuse the complete volume of the printing material, thereby enabling the creation of intricate structures in a single, continuous process.

8) Digital Light Process (DLP):

DLP serves as an alternative to laser-based SLA. The primary distinction between DLP and laser-based SLA lies in the method of layer exposure. DLP employs a digital projector to project UV light or visible light, flashing a singular image of the layer simultaneously across the entire resin, in contrast to the laser scanning approach used in traditional SLA.

These 3D printing methods offer various capabilities and are chosen based on the specific requirements of the biomaterial, the intended application, and the desired properties of the final construct. Advances in 3D printing technology continue to expand the possibilities for creating biomaterials with enhanced complexity and functionality.

One of the key advantages of 3D printing in biomaterial fabrication is its ability to produce complex structures that closely emulate natural tissues. This is particularly beneficial in tissue engineering, where scaffolds can be precisely designed to match the architecture of the target tissue, promoting optimal cell adhesion, proliferation, and differentiation. Additionally, 3D printing allows for the incorporation of multiple materials within a single construct, enabling the fabrication of composite biomaterials with diverse mechanical and biological properties.

The versatility and efficiency of 3D printing have opened up new possibilities in creating patient-specific implants, prosthetics, and drug delivery systems. This technology not only streamlines the manufacturing process but also offers a level of customization that can address individual patient needs. As research in 3D printing for biomaterials continues to advance, it holds great promise for revolutionizing various aspects of regenerative medicine, personalized healthcare, and the development of advanced biomedical devices.

2. Objectives

In the contemporary landscape of biomedicine and tissue engineering, there exists a critical and immediate need for biomaterials that are both versatile and multifunctional in the realm of clinical applications. The expectations extend beyond the pursuit of thorough and efficient materials, systems and treatments, encompassing precisely tailored and even personalized medical devices. In response to this evolving demand, contemporary biomaterials must undergo enhancements in their chemical and physical properties, providing highly tunable platforms to meet individualized needs. The goal, therefore, is to create biomaterials that not only address clinical requirements but also offer the flexibility required for personalized adjustments, reflecting the diverse preferences and needs of modern society.

To achieve this objective, a pivotal amalgamation involves the integration of antifouling biomaterials with regenerative abilities, coupled with the transformative capabilities offered by 3D printing technology. This synergistic approach holds the potential to revolutionize clinical applications by combining the benefits of materials resistant to adverse nonspecific interactions with the precision and customization afforded by advanced 3D printing techniques. By seamlessly merging these elements, the resulting biomaterials stand poised to meet the multifaceted needs of the world's population, providing a harmonious balance between efficacy, personalization, and adaptability in the realm of medical solutions.

Achieving this goal involves a comprehensive investigation into antifouling polymer brushes immobilized on material surfaces, forming the crucial point of this research. The study aims to delve into (1) the intrinsic details of how these polymer brushes can be effectively employed to resist fouling on material surfaces and (2) the broader implications and applications of these antifouling structures and materials within the context of fabrication processes. By scrutinizing the interaction and performance of antifouling polymer brushes in material design, the study endeavors to contribute valuable insights that can enhance the overall efficiency and adaptability of biomaterials in response to the contemporary demand for versatile and customized clinical solutions.

3. Experimental Section

3.1. Materials

Silicon wafers with a ⟨100⟩ orientation and a native silicon oxide layer were procured from Siegert Wafer GmbH (Germany). Additionally, silicon wafers coated with a 150 nm layer of gold (Au) and glass slides intended for surface plasmon resonance measurements, coated with either a 50 nm layer of Au or a combination of 50 nm Au and a 15 nm SiO_2 overlayer, were obtained from the Institute of Photonics and Electronics, Czech Academy of Sciences, Czechia.

The following chemicals were purchased from Sigma-Aldrich: Copper(I) bromide (CuBr, 99.99%), 2,2'-bipyridyl (BiPy, 99%), α-bromoisobutyryl bromide, methacryloyl chloride (MACl), 10-undecen-1-ol, trichlorosilane, 4-cyano-4-(phenylcarbonothioylthio) pentanoic acid (CTA), 1-aminopropan-2-ol, triethylamine (TEA, 99.5%), and hexylamine (99%). 4,4-azobis[2-(imidazolin-2-yl) propane] dihydrochloride (VA-044) and azobisisobutyronitrile (AIBN) were purchased from Wako. TEA underwent distillation over CaH_2 for purification before use. All other reagents were used as received.

Dimethyl sulfoxide (DMSO), toluene, dichloromethane (DCM), tetrahydrofuran (THF), dimethylformamide (DMF), 1, 4-dioxane and methanol were purchased from Acros Organics (extra dry, stored over molecular sieves, and filtered using a 0.22 μm syringe filter before use). Other organic solvents of analytical grade, hydrochloric acid (HCl), sodium hydrogen carbonate ($NaHCO_3$) and anhydrous sodium sulfate (Na_2SO_4) were from Lach-Ner (Czech Republic) at the highest available purity and used as received. Deionized (DI) water was obtained from a Milli-Q purification system (Milli-Q gradient A10, Merck-Millipore).

Human serum albumin (HSA) and human fibrinogen (Fbg) were purchased from Sigma-Aldrich. Pooled human blood plasma (HBP), a mixture from five donors, was sourced from the Institute of Hematology and Blood Transfusion, Czechia.

3.2. Synthesis

3.2.1. Synthesis of precursors

1) (11-(2-bromo-2-methyl)propionyloxy)undecyltrichlorosilane (Br-Silane)

In the first step, a solution composed of 10-undecen-1-ol (15 mL, 75 mmol) and TEA (13.5 mL, 90 mmol) in dry THF (75 mL) underwent a dropwise addition of α-bromoisobutyryl bromide (10.7 mL, 25 mmol) in 30 mL of dry THF at 0 ºC. The resulting reaction mixture was stirred overnight at room temperature. Hexane (150 mL) was then introduced, followed by two washes with 2 N HCl, two washes with brine and water. The mixture was subsequently dried over anhydrous sodium sulfate. After solvent removal under vacuum, the product, 10-undecen-1-yl-2-bromo-2-methylpropionate, underwent purification through vacuum distillation. Then a fully characterization of NMR was performed.

In the second step, 10-undecen-1-yl-2-bromo-2-methylpropionate (8.15 g, 25 mmol) and trichlorosilane (25.3 mL, 250 mmol) were combined in a dry flask filled with argon. Karstedt's catalyst (500 ppm equivalent) was added, and the mixture was stirred for an overnight reaction. The resulting mixture was rapidly passed through a silica column to eliminate the catalyst, and the remaining trichlorosilane was removed by vacuum evaporation. Final purification was achieved through Kugelrohr distillation, and the final product (Br-silane) was obtained. [9, 74]

2) Br-SAM

The silicon substrates underwent a cleaning process, involving two rinses with ethanol and deionized (DI) water, followed by drying under a nitrogen stream. Subsequently, they were activated in a UV/O_3 cleaner for 20 minutes. Immediately afterward, the activated substrates were immersed in a 0.1% v/v solution of Br-silane in anhydrous toluene and kept in a dry environment at room temperature for 3 hours. The silicon substrates, now coated with a self-assembled monolayer of Br-silane (Br-SAM), were washed with toluene, acetone, and two rounds of rinsing with ethanol and DI water. Following the washing steps, the substrates were dried under a nitrogen stream.

3) CTA-SAM

The Br-SAM was introduced into reactors within an argon atmosphere. A stock solution, composed of 66.69 mg of 4-cyano-4-(phenylcarbonothioylthio) pentanoic acid (CTA, 0.239 mmol), 6.10 mg of CuBr (42.5 μmol), and 12.99 mg of BiPy (83.2 μmol) in deoxygenated anhydrous DMSO (10 mL), was added under argon. This solution had been purged with argon for 30 minutes beforehand. The reaction (atom transfer radical addition) proceeded for 24 hours at 30 °C, resulting in the formation of the CTA immobilized substrates (CTA-SAM) (see Scheme 1). [75] Subsequently, the modified CTA-SAM substrates underwent washing steps with methanol, acetone, and twice with ethanol and DI water, followed by drying under a nitrogen stream. [59]

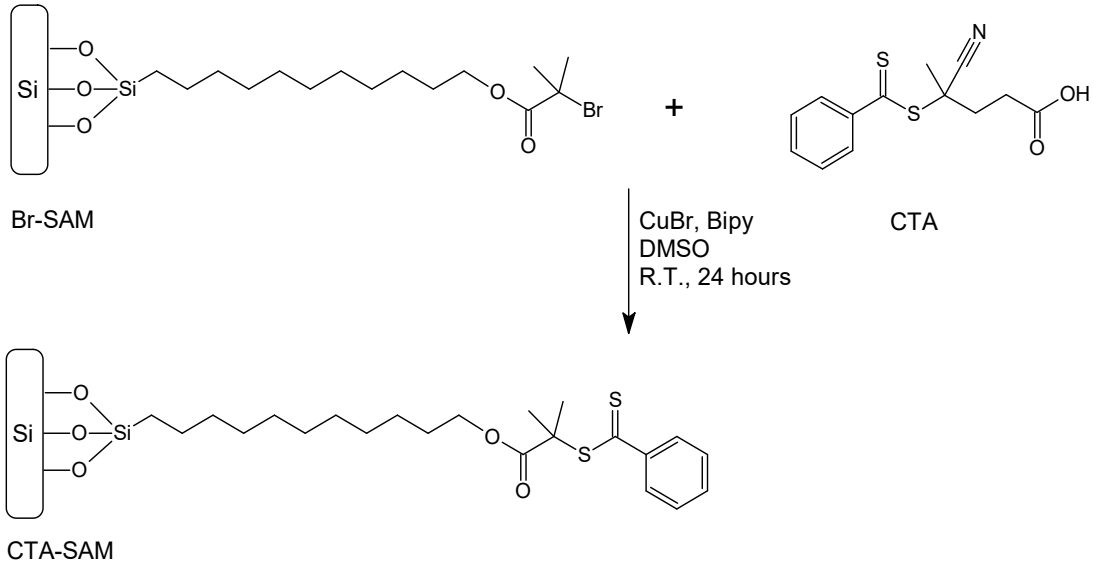

Scheme 1: Chemical structure and reaction mechanism of CTA-SAM preparation. The same avenue can be utilized for the immobilization of CTA-SAM on various metal oxides (including such as ZnO, Al_2O_3,TiO_2, ZrO2, etc.) used in sensing and biomedical applications.

4) *N*-(2-hydroxypropyl) methacrylamide (HPMA)

Anhydrous sodium hydrogen carbonate (33.6 g, 0.34 mol) was suspended in a solution containing 1-aminopropan-2-ol (22.9 g, 0.30 mol) in 85 ml anhydrous dichloromethane (DCM). The suspension was cooled to 0°C, and a solution of methacryloyl chloride (MACl, 31.9 g, 0.29 mol) in 40 ml DCM was added dropwise under cooling and vigorous stirring for over 1 hour. The reaction mixture was stirred for an additional 30 minutes at 15°C. Subsequently, 10 g of

anhydrous sodium sulfate was introduced, the resulting solid was filtered off, and the dry filtrate was concentrated to half of the original volume under evaporator. HPMA was obtained by crystallization from DCM at -20 ℃ and further purified through recrystallization from acetone (see Scheme 2). [76]

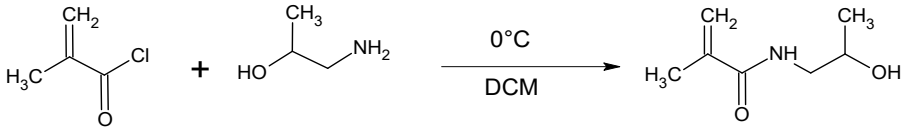

Scheme 2: Chemical structure and reaction mechanism of HPMA.

5) (3-Methacryloylamino-propyl)-(2-carboxy-ethyl)-dimethyl-ammonium (carboxybetaine methacrylamide) (CBMAA)

In 100 mL of dry tetrahydrofuran (THF), dimethylaminopropylmethacrylamide (17 g, 100 mmol) was dissolved and cooled to 0 °C. A small amount of diphenylpicryl hydrazyl was introduced as an inhibitor in the solution. Following that, β-propiolactone (9 g, 125 mmol) was dissolved in 30 mL of dry THF and added dropwise under nitrogen over 3 hours. The reaction was allowed to proceed at 4 °C for 24 hours (see Scheme 3). The resulting white precipitate was filtered and washed with dry THF and ether. The product was then dried under a high vacuum. [48]

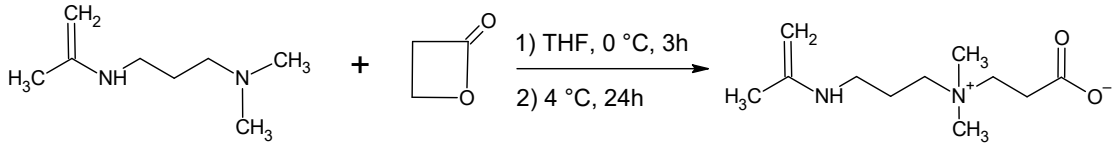

Scheme 3: Chemical structure and reaction mechanism of CBMAA.

3.2.2. Conventional RAFT polymerization of HEMA, HPMA, and CBMAA

The synthesis of polymers from HEMA, HPMA, and CBMAA was achieved through RAFT polymerization. In this procedure, a flask containing the monomer (e.g., HEMA, HPMA, or CBMAA), 4-cyano-4-(phenylcarbonothioylthio) pentanoic acid (CTA), and initiators (AIBN or VA-044), sealed with a septum, underwent a 1-hour argon purge in an ice bath. The feeding ratio between CTA and initiators was applied between 10 and 2. Simultaneously, the selected solvent (e.g., methanol, DMF, DMSO, 1,4-dioxane, water, or a mixture) also underwent a similar 1-hour

argon purge and was then introduced into the flask containing the solids. The resulting mixture was stirred until complete dissolution. RAFT polymerization was initiated by placing the flask with the reaction mixture into a temperature-controlled oil bath at a predetermined temperature (45 °C for VA-044 or 80 °C for AIBN in this study) for a specified duration (ranging from 0.5 hours up to 48 hours) (see Scheme 4). The polymerization was terminated by exposing the reaction vessels to the atmosphere and rapidly cooling the solution in an ice bath. For the isolation of poly(HPMA) and poly(CBMAA), the solution underwent dialysis against DI water with regular renewal for 24 hours, followed by lyophilization. To isolate poly(HEMA), the solution was precipitated in ethyl ether, and the resulting precipitate was collected through centrifuge filtration.

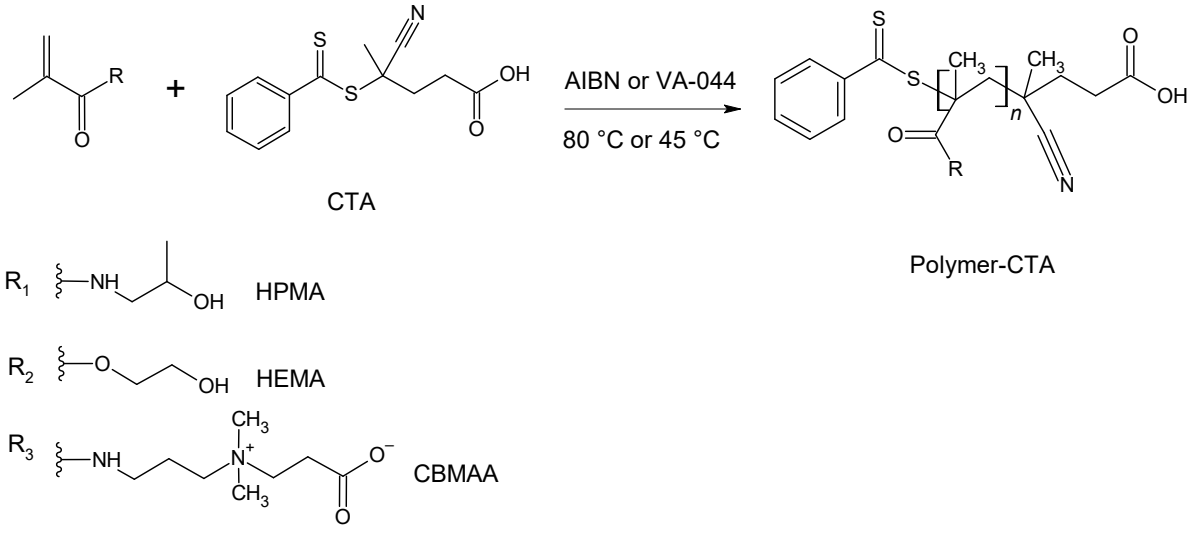

Scheme 4: Chemical structure and reaction mechanism of RAFT polymerization.

3.2.3. Aminolysis process of polymers with end groups containing CTA

Both solution-born and GF polymers were terminated with thiocarbonylthio (S-C=S) end groups after RAFT polymerization. These end groups were subsequently converted to thiol (-SH) groups through aminolysis for atomic force microscopy based single molecule force spectroscopy (AMF-SMFS) measurement. [50, 53, 59, 77] To initiate the aminolysis reaction, anhydrous ethanol and a mixture of hexylamine (20 µL, 0.153 mmol) and TEA (20 µL, 0.143 mmol) were deoxygenated by purging with argon for 10 minutes. The reaction solution was then prepared by adding 5 mL of degassed ethanol into the flask containing the amines. For aminolysis of polymer-CTA recovered from solution, 5 mL of the reaction solution was added under argon to a flask containing 25 mg of the polymer, which had been previously deoxygenated. The reaction proceeded at room

temperature for 3 hours (see Scheme 5). The resulting polymers with thiol moieties (polymer-SH) was recovered after dialysis and lyophilization. For the GF polymer brushes, the aminolysis procedure was similar, except that the substrates coated with polymer brushes were placed in reactors instead of using polymer collected from solution. Subsequently, the substrates coated with polymer-SH brushes were washed with methanol, acetone, and twice with ethanol and DI water. Finally, they were dried under a stream of nitrogen.

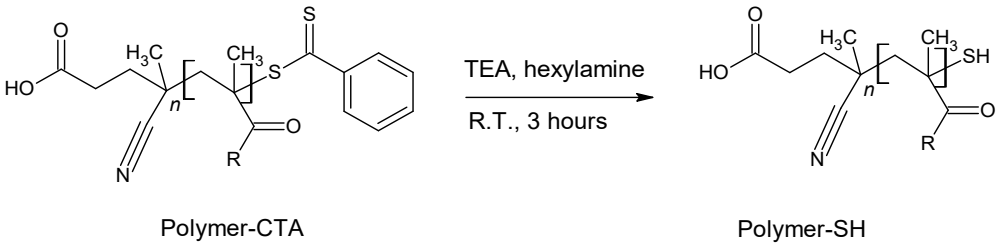

Scheme 5: Chemical structure and reaction mechanism of aminolysis.

3.2.4. Grafting-to method: Good solvent and poor solvent

The initial step involved cleaning the bare gold wafer substrates or surface plasmon resonance (SPR) chips by rinsing them twice with ethanol and DI water, followed by drying under a stream of nitrogen. Subsequently, activation was carried out in a UV/O_3 cleaner for 20 minutes. In parallel, a polymer solution of poly(HPMA)-SH was prepared at a concentration of 1 mg·mL^{-1} in DI water (yielding a transparent solution) under good solvent conditions, or in 0.75 M $Na_2SO_{4(aq)}$ for achieving a cloud point under poor solvent conditions. [78]

Following solution preparation, the freshly cleaned gold wafer substrates or SPR chips were promptly placed in reactors. A solution of poly(HPMA)-SH, prepared under either good or poor solvent conditions, was added to the reactors. The binding between thiol and gold was allowed to occur for 20 hours at 28 °C under an argon atmosphere. Subsequently, the substrate containing surface-grafted polymers were rinsed successively with DI water, acetone, and washed twice with ethanol and DI water, before being dried using a nitrogen stream.

3.2.5. Grafting-from method: Surface-initiated RAFT polymerization

The SI-RAFT polymerization followed a reaction condition similar to conventional RAFT polymerization. In this procedure, a flask sealed with a septum containing the monomer (e.g., HEMA and HPMA), CTA, and initiators (AIBN or VA-044) underwent a 1-hour argon purge in an

ice bath. However, the feeding ratio between CTA and initiator was adjusted to either 2 or 1 which is lower than conventional condition, and a high monomer concentration in the solution was desired (250 mg·mL^{-1} was applied as optimal). The molar ratio between monomer, CTA, and initiator was optimized as 1735:1:1 under conditions using AIBN and 1500:2:1 for VA-044. Simultaneously, the selected solvent (e.g., methanol, DMF, DMSO, 1,4-dioxane, water, or a mixture) also underwent a similar 1-hour argon purge and was then introduced into the flask containing the solids. The resulting mixture was stirred until complete dissolution and subsequently transferred to individual reactors containing CTA-SAM with different density of grafting sites (dilution series) under argon protection, which had been previously sealed and deoxygenated. The initiation of SI-RAFT polymerization occurred by placing the flask with the reaction mixture into a temperature-controlled oil bath at 45 °C for VA-044 condition or 80 °C for AIBN condition for a specified duration, ranging from 0.5 hours up to 48 hours (see Scheme 6). Polymerization was terminated by exposing the reaction vessels to the atmosphere and rapidly cooling the solution in an ice bath. Following this, the polymer-coated substrates via grafting-from underwent washing steps with methanol, acetone, and twice with ethanol and DI water, followed by drying under a nitrogen stream.

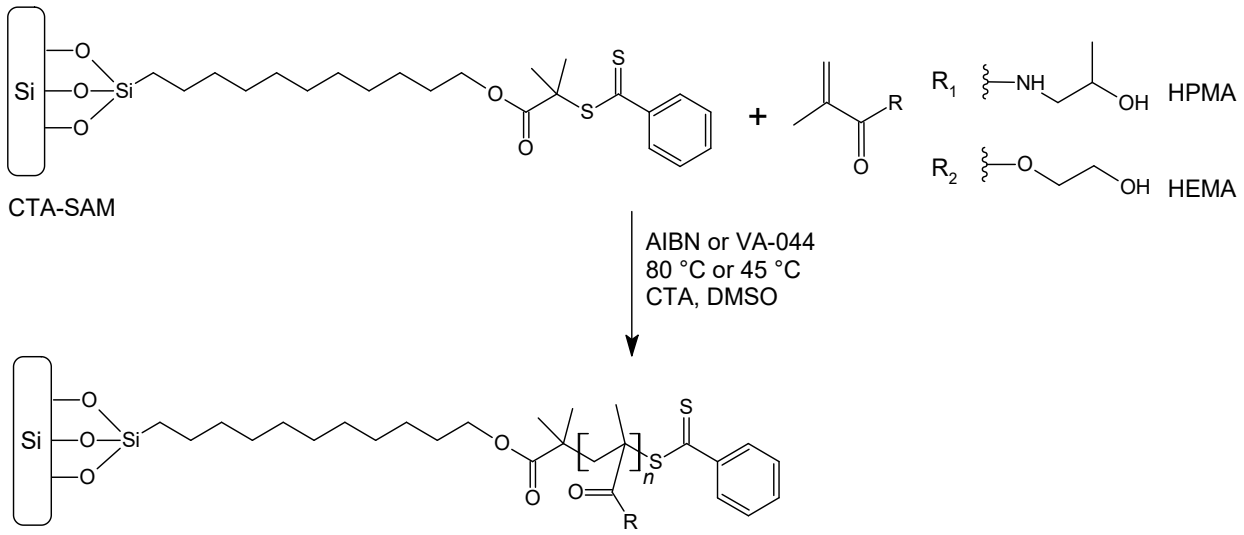

Scheme 6: Chemical structure and reaction mechanism of GF polymer-CTA.

3.2.6. Thiol-yne click reaction of peptide nucleic acids (PNAs)

The poly(HEMA) substrates containing thiol end group were immersed in the reactors under the solution of various concentration (0.01, 0.1, and 1 $mg \cdot mL^{-1}$) of peptide nucleic acids (PNAs) modified with alkyne groups with 1 hour incubation time. After the incubation time, the reactors containing substrates and solution were exposed to UV light with wavelength 254 nm for one min (see Scheme 7). Subsequently, the substrates coated with poly(HEMA)-PNAs were washed with methanol, acetone, and twice with ethanol and DI water. Finally, they were dried under a stream of nitrogen.

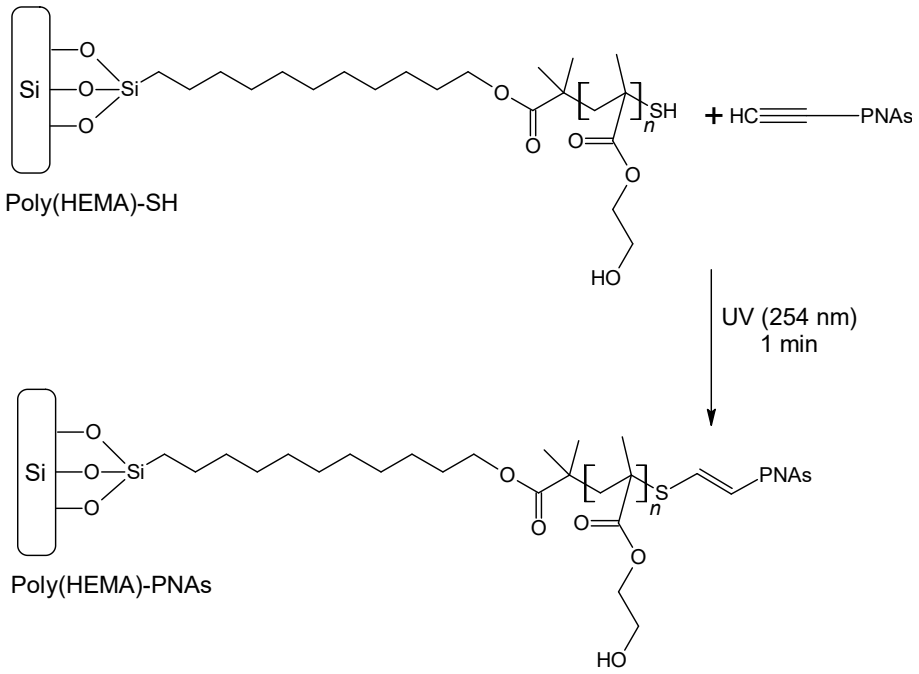

Scheme 7: Chemical structure and thiol-yne click reaction of poly(HEMA)-PNAs.

3.2.7. DLP 3D Printing incorporated with PET-RAFT polymerization

1) VAT polymerization

VAT Polymerization is a 3D printing method that employs photopolymerization, utilizing UV light to solidify liquid short polymers and their precursors for the purpose of producing precisely defined 3D objects. This process is facilitated through digital light processing technology, which plays a key role in the precise exposure of liquid resin to UV light for controlled polymerization. In the initial step of this 3D printing technique, a 3D design is crafted

using dedicated software. This digital representation serves as the blueprint for the subsequent fabrication process. Once the design is ready, the VAT polymerization system utilizes digital light processing to selectively solidify the liquid resin layer by layer, gradually building the desired 3D object. This method offers a precise and controlled approach to additive manufacturing, enabling the creation of intricate and detailed structures in the final printed product.

The study encompassed the preparation of a VAT solution, crafted by blending poly(ethylene glycol) diacrylate with varied molar masses of 700, 1000, and 2000 (referred to as DAPEG-700, DAPEG-1k, DAPEG-2k, functioning as crosslinkers), and HPMA, in addition to CTA, diphenyl(2,4,6-trimethylbenzoyl) phosphine oxide (TPO-L, employed as photo-initiators), and tetrazine (utilized as a photo-absorber) (see Scheme 8). All components were dissolved in DMSO. The formulation applied an optimized ratio of 300:100:1:25:0.6 for DAPEG-700, HPMA, CTA, TPO, and tetrazine, respectively, in DMSO. [79-82]

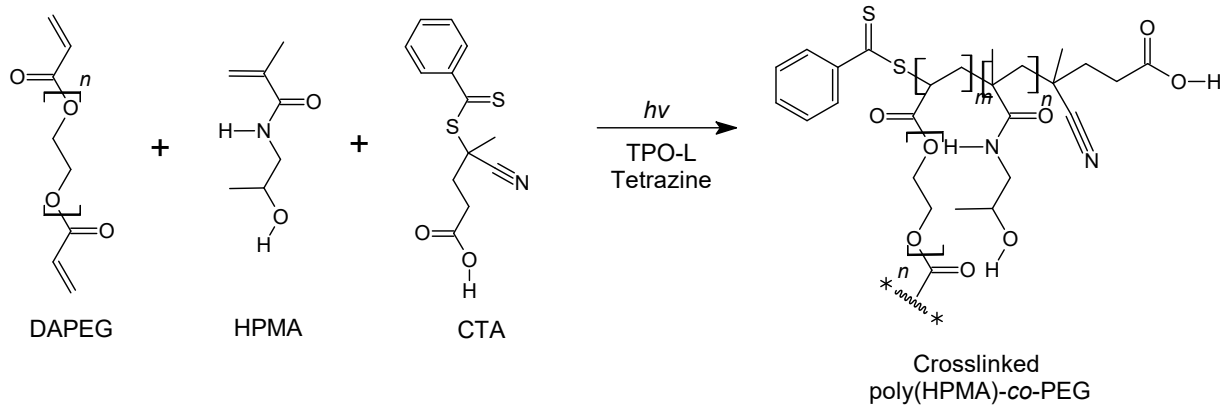

Scheme 8: Polymer hydrogel copolymerization through PET-RAFT polymerization using VAT polymerization.

2) 3D printed scaffold

The DLP (CellInk LumenX+) printing was performed under the following settings: an intensity of 34.84 mW·cm^{-2} at a wavelength (λ) of 405 nm, a printing temperature of 22 °C, and a curing time of 11 seconds per layer. Following the printing process, the hydrogel samples were thoroughly cleansed using DMSO to eliminate unreacted residues. Subsequently, a progressive washing procedure with a water/DMSO mixture was employed until reaching pure water. Finally, the printed hydrogel samples underwent a post-curing phase lasting 30 minutes,

accomplished by exposing the hydrogels to UV light with an irradiance of 6 watts and a wavelength (λ) of 365 nm. This procedure deactivates the free double bonds thus cancelling possible adverse post-polymerization reactions. We had planned to explore the DL) method for fabricating composite materials incorporating ZnO (Zn-SAM-CTA) components. However, due to time constraints, we were unable to pursue this avenue.

3) Post-polymerization of printed scaffold

First, we initiated the aminolysis of the printed hydrogel-CTA (referred to as [poly(HPMA)-*co*-PEG]-CTA) according to the procedure outlined in Section 3.2.3. Subsequently, the hydrogel, now containing thiol end groups (referred to as [poly(HPMA)-*co*-PEG]-SH), underwent thorough and regular washing with ethanol for a day. Following this, the hydrogel-SH was immersed in a quinine solution in ethanol, with a concentration of 5 mg·mL^{-1}, for an hour to allow for adequate penetration of quinine into the inner regions of the hydrogel-SH. Next, the reactor containing quinine solution and the hydrogel-SH was subjected to UV light with a wavelength of 365 nm for 1 hour (see Scheme 9). Meanwhile, a control of hydrogel without aminolysis (i.e.: [poly(HPMA)-*co*-PEG]-CTA) was also undertaken the same procedure as reference. Subsequently, both samples underwent extensive washing with methanol for a duration of 3 days, followed by regular washing with progressively higher concentrations of water until reaching full immersion in water for the final rinsing process.

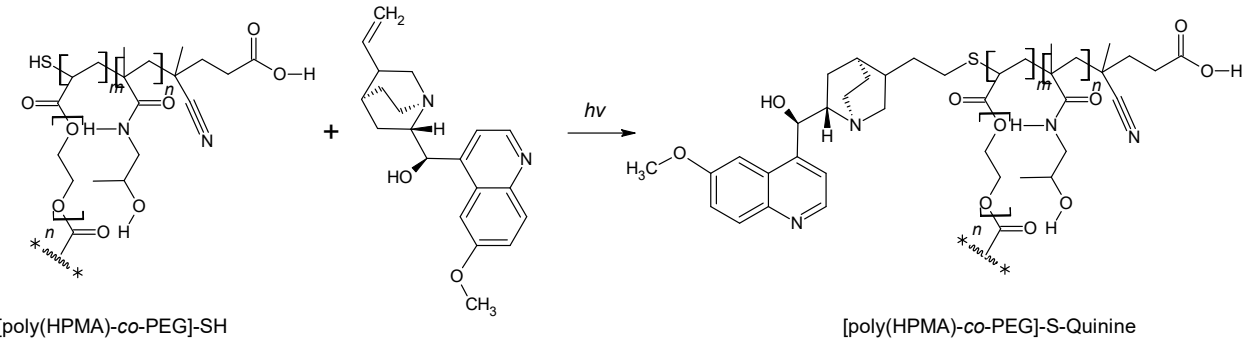

Scheme 9: : Chemical structure and thiol-ene click reaction of [poly(HPMA)-*co*-PEG]-S-Quinine.

In order to further exploit the CTA functional groups within the hydrogel, we implemented a chain growth polymerization technique and introduced DFEA as a chain extension agent. A solution containing DFEA in DMF, with a concentration of 250 mg·mL^{-1}, was applied for one hour to ensure thorough penetration of DFEA into the internal regions of the hydrogel.

Subsequently, post-polymerization was initiated by immersing the reactor containing the polymerization solution and hydrogel in a temperature-controlled oil bath set at 80 °C for 3 hours (see Scheme 10). Upon completion of the reaction time, the reactor was promptly cooled in an ice bath and opened to expose the sample to the ambient atmosphere. Following this, the hydrogel underwent extensive washing with DMF for a duration of 3 days, followed by regular washing with progressively higher concentrations of water until it was fully immersed in water for the final rinsing step.

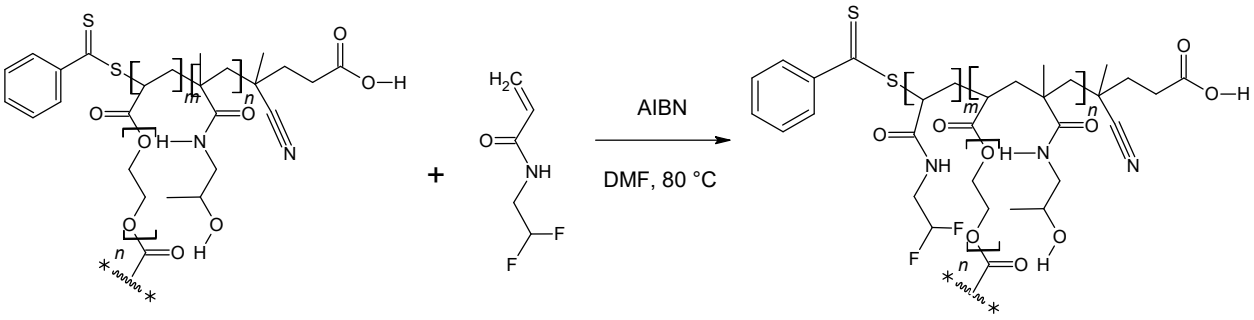

Scheme 10: Chemical structure and chain growth reaction of [poly(HPMA)-*co*-PEG]-*b*-poly(DFEA).

3.3. Characterization

3.3.1. Equipment

1) Nuclear magnetic resonance (NMR)

All samples were measured by ^{1}H-NMR (Bruker Avance III spectrometer operating at 300.13 MHz (^{1}H) in d-$CDCl_3$, D_2O, or d-DMSO) to determine their chemical shift or monomer conversion.

2) SEC-multiple angle laser light scattering (SEC-MALS)

In the SEC analysis using aqueous solution, the system was equipped with a Superose 12 or Superose 6 column, an online UV detector (Shimadzu). The detection included a DAWN HELEOS II MALS detector (Wyatt Technology Corp.) with the laser operating at a wavelength λ=658 nm and an Optilab T-rEX differential refractometer (Wyatt Technology Corp.). For the measurements of water-soluble polymers, the utilized mobile phase was a 0.3 M sodium acetate

buffer with a pH of 6.5 and 1 $g \cdot L^{-1}$ of NaN_3, flowing at a rate of 0.5 $mL \cdot min^{-1}$. The specific refractive index increment (d*n*/d*c*) of poly(HPMA) was applied as 0.167 and poly(CBMAA) was applied as 0.163. Data were recorded using Astra software (Wyatt Technology Corp.), and $Đ$, M_w, and M_n values were determined.

The SEC analysis in an organic solvent was conducted using a Deltachrom SDS 030 pump (Watrex Ltd.) with a flow rate set at 0.5 $mL \cdot min^{-1}$, along with an autosampler MIDAS (Spark Ltd.). Two PLgel 10-µm mixed B LS columns (Polymer Laboratories) were arranged in series, each separating within the molecular weight range of approximately $5 \times 10^2 \leq M \leq 1 \times 10^7$ (relative to PS standards). The detection included a DAWN HELEOS II MALS detector (Wyatt Technology Corp.) with the laser operating at a wavelength λ=658 nm and an Optilab T-rEX differential refractometer (Wyatt Technology Corp.). The mobile phase, consisting of N,N-dimethylformamide (≥ 99.9%, for HPLC) with the addition of 0.1M LiCl (95%), was employed at ambient temperature. The specific refractive index increment (d*n*/d*c*) for poly(HEMA) was applied as 0.09. Data were recorded using Astra software (Wyatt Technology Corp.), and $Đ$, M_w, and M_n values were determined.

3) Spectroscopic ellipsometry (SE)

Ellipsometric data were collected utilizing a J.A. Woollam M-2000X spectroscopic ellipsometer, operating in rotating compensator mode, at an AOI range of 60–71° with a step of 1°. The spectral range covered wavelengths from λ = 250 to 1000 nm. In-house developed variable AOI immersion cell were utilized to obtain *in situ* ellipsometry data while operating in water. The immersion cell consists of a dish filled with the liquid or environment of interest, along with two optically flat plates (strain-free, with dimensions $\phi = 5$ mm and $h = 2$ mm, made of UV fused silica from UQG-Optics). These plates serve as entrance and exit windows and are rigidly connected to the polarizer and analyzer ellipsometer arms. Importantly, they do not make direct contact with the immersion dish and the sample, ensuring measurements at AOI. The windows, oriented orthogonally to the beam, achieve ideal beam orientation in both air and the liquid environment, thereby eliminating errors in AOI due to the presence of windows in the goniometer setup. The minimal optical retardation of the windows was determined in a straight-through configuration (AOI = 90°). All measurements were adjusted for the in-plane retardance effects of the windows on the ellipsometric angle Δ using the specified relation:

$$\Delta_{\text{Offsets}}(\lambda) = \Delta_{\text{Offset 1}} + \frac{\Delta_{\text{Offset 2}} \times \lambda^2}{100}$$

The values for $\Delta_{\text{Offset 1}}$ and $\Delta_{\text{Offset 2}}$ were determined to be -0.011 ± 0.001 and 0.021 ± 0.004, respectively, within the specified wavelength range. The consideration of Ψ_{Offsets} due to the presence of windows was omitted because these values fell within the precision limits of ellipsometric measurements in a straight-through configuration, specifically 45.000° ± 0.075°.

The acquired data were subjected to fitting using the CompleteEASE software employing a multilayer model. The optical dispersion function of the gold layers was determined using the multiple environment approach (MEA). Ellipsometric data for bare samples in both air and water were processed with a basis spline function, utilizing the complex refractive index of single crystal gold as the initial value at each measured wavelength. Since the optical properties of gold remain consistent across different environments, this approach enhances the analytical/fitting capabilities, resulting in more reliable outcomes for the complex refractive index of gold.

It is noteworthy that, in addition to the *in-situ* measurements at multiple AOI, employing MEA to ascertain the substrate's dispersion function is a crucial prerequisite for obtaining reliable ellipsometric data and results for the swollen layers. The optical dispersion function of water was extracted from the CompleteEase database. The thickness and refractive index of both dry and swollen poly(HPMA) layers were derived through simultaneous fitting of the obtained ellipsometric data using Cauchy dispersion functions:

$$n = A + \frac{B}{\lambda^2} + \frac{C}{\lambda^4}$$

The presented values represent averages calculated from three independent samples, expressed as mean ± standard deviation.

4) Fourier-transform infrared spectroscopy (FTIR)

FTIR measurements in reflection mode were conducted on dry polymer layers using a Nicolet Nexus 870 FTIR spectrometer (ThermoFisher Scientific). The instrument was equipped with both a grazing angle attenuated total reflection (GAATR) attachment featuring a Ge hemispherical crystal with an angle of incidence (AOI) range between 60–65° (VariGATR from Harrick Scientific Products) and a grazing angle specular reflection (GASR) attachment

(ThermoFisher Scientific). The measurement chamber of the spectrometer was consistently purged with dry air.

In the GAATR-FTIR mode, silicon substrates with polymer coatings were measured, while the GASR-FTIR mode was employed for polymer coatings on gold substrates. All spectra were recorded with 256 scans at a resolution of 2 cm^{-1} and processed using OMNIC software. The total acquisition time for each spectrum was approximately 3 minutes. All reported FTIR spectra are presented as absorbance values relative to reference spectra obtained from freshly cleaned silicon and gold substrates.

5) X-ray photoelectron spectroscopy (XPS)

Measurements were conducted using a K-Alpha$^+$ X-ray Photoelectron Spectrometer (XPS) from ThermoFisher Scientific, operating at a base pressure of 1.0×10^{-7} Pa. Thermo Avantage software was employed for data acquisition and processing. To mitigate X-ray-induced damage to the thin polymer films and enhance the signal-to-noise ratio, individual points were measured within areas covering 8×8 mm^2.

At each point, a high-energy resolution core-level spectrum was obtained using microfocused, monochromated Al Kα X-ray radiation, with a spot size of 400 μm and pass energy set at 150 and 50 eV for survey and high-resolution measurements, respectively. All reported XPS spectra represent averages of 24 individual measurements. The spectra were referenced to the C 1s peak of hydrocarbons at a binding energy of 285.0 eV, controlled using photoelectron peaks of polyethylene terephthalate (PET) and metallic Cu, Ag, and Au standards.

The atomic concentrations of different chemical moieties were determined from the respective photoelectron peak areas of levels Br 3d, Au 4f, Si 2p, S 2p, C 1s, N 1s, and O 1s high-resolution spectra, after Shirley's inelastic background subtraction modification. Assuming a simple model of a semi-infinite solid with homogeneous composition, the peak areas were corrected for photoelectric cross-sections, inelastic mean free paths of the electrons, and the transmission function of the spectrometer used.

Voigt profiles were employed for fitting all high-resolution spectra to unravel the presence of individual chemical species and extract the surface composition. The experimental uncertainties in the quantitative analysis of XPS were evaluated to be below 10%,

encompassing overall uncertainties related to sample preparation and XPS background subtraction.

6) AFM-based single molecule force spectroscopy (SMFS)

The SMFS measurements were conducted using an AFM setup (Bruker JPK Nanowizard) operating in Force Spectroscopy mode. Scanning was conducted over areas of 500 × 500 nm² and 2 × 2 μm², with each area being scanned by 512 × 512 points. Gold-coated tips (MikroMasch, HQ:CSC38/Cr-Au) with three cantilevers and a nominal tip radius of 35 nm were employed for the measurements. The SMFS experiments were carried out in DI water.

Following the mounting of the cantilever, calibration was performed for sensitivity and spring constant. The tip-sample separation was set to 500 nm, and the force curves were moved with a frequency of 0.5 Hz. The obtained data were analyzed using the Data Processing software of Bruker JPK. From the measured curves, those displaying rupture events were selected and fitted to the worm-like chain (WLC) model to determine the contour length (l_c) of the polymer chains.

7) Surface plasmon resonance (SPR)

Non-specific protein adsorption on various surfaces, including the bare SPR chip, SiO_2-coated SPR chip, polymers grafted-from SiO_2-coated SPR chip, and polymers grafted-to SPR chip, was assessed using an SPR instrument based on the Kretschmann geometry of attenuated total reflection and spectral interrogation. In this setup, the shift in the resonance wavelength was recorded, and the quantity of biomolecules adsorbed on the coating was estimated from the difference between the baselines in pure phosphate-buffered saline (PBS) at pH 7.4 before and after exposure to the tested solutions: human serum albumin (HSA) at 5 mg·mL^{-1} in PBS, fibrinogen (Fbg) at 1 mg·mL^{-1} in PBS, and undiluted pooled human blood plasma (HBP). The solutions were flowed through a 4-channel flow cell attached to an SPR chip for 15 minutes. The measurements were conducted at a flow rate of 25 μL·min^{-1} and a temperature of 25 °C (± 0.1 °C). The fouling adsorbed mass was determined using the calibration of the sensor response, as described in the next subsection.

8) Dynamic viscosity measurement

Dynamic viscosity measurements were conducted using a rotational rheometer, specifically the ARES G2 model from TA Instruments, USA. The shear flow experiments were carried out at 23 ℃ over a range of shear rates spanning from 1 to 10 s^{-1}. The measurements utilized a cone-plate geometry with a plate diameter of 25 mm and a cone angle of 0.1 rad in an open vesicle.

9) Electrokinetic measurement (EK)

Streaming current (I_{str}) measurements were performed at varying pressures (ΔP) across rectangular streaming channels (length L_o = 20 mm, width ℓ = 10 mm, height H = 30 μm) formed by two poly(HPMA) brush-coated silicon substrates using the Microslit Electrokinetic Set-up. The EK measurements were performed as a function of solution pH and were started from the alkaline pH. For each composition of the electrolyte the samples were equilibrated for about 30 min prior to measurement.

10) Neutron Reflectometry (NR)

Neutron reflectometry (NR) was conducted using SPATZ, the second implementation of a time-of-flight neutron reflectometer at OPAL research reactor. Experimental conditions involved setting the angle of incidence at 0.7 and 3.5, with Q values ranging from 0.0083 to 0.2740. The SLD superphase was 0 $Å^{-2}$, the subphase was $2.07*10^{-6}$ $Å^{-2}$, and the critical edge occurred at Q = 0.01020 $Å^{-1}$. This approach has been validated for examining dry and swollen brushes. NR experiments followed a similar protocol to ellipsometry experiments: initially, the dry state was measured in air. Subsequently, the brush was exposed to pure D_2O. [83-85]

11) Thermogravimetric analysis (TGA)

The analyses were carried out using a TGA Q50 instrument from TA Instruments. The samples were placed in a platinum pan and subjected to a nitrogen flow of 60 $mL \cdot min^{-1}$. Thermogravimetric analyses (TGA) were conducted over temperature range of 30 °C to 600 °C with a heating rate of 10 °C min^{-1}.

12) Differential Scanning Calorimetry (DSC)

DSC measurements were conducted utilizing a DSC Q2300 instrument from TA Instruments and an RSC 500 cooler located in Zellik, Belgium. The experiment involved 3 mg of the printed hydrogel sample, with a heating and cooling rate set at 10 °C min^{-1}. Each sample was analyzed in an aluminum Tzero pan under a nitrogen flow, with an empty pan serving as the reference. The DSC thermograms were then analyzed using the Q series software.

13) Cell viability- MTS assay

Fibroblasts were initially seeded in the wells and allowed to incubate for one day in standard culture medium. Subsequently, the culture medium was replaced with leaching medium, and metabolic activity evaluation took place a day later. The MTS absorbance at 490 nm, indicative of metabolic activity, had the background subtracted first. Following this, each printed hydrogel sample with leaching medium from various days was referenced against the tissue culture plate (TCP), serving as the positive control with no leaching medium.

3.3.2. Calculations

1) Utilization of the worm-like chain (WLC) model for SMFS data.

The curves depicting rupture events were subjected to fitting using the WLC model:

$$f(x) = \frac{k_b T}{l_p}\left[\frac{1}{4\left(1-\frac{x}{l_c}\right)^2} - \frac{1}{4} + \frac{x}{l_c}\right]$$

In the provided context, the variables are defined as follows: x represents the displacement length between the AFM tip and the surface, k_b is the Boltzmann constant, T is the absolute temperature, l_p is the persistence length, and l_c is the contour length. The corresponding molar mass of grafted-from poly(HPMA) chains was calculated by dividing the number-average l_c by the size of the repeat monomer unit (C–C–C bonds along the main chain, i.e., 2.73 Å). [50, 86]

2) Calculation of water content in swollen Poly(HPMA) layers

Ellipsometrically determined thicknesses in both the dry and swollen states were employed to calculate the swelling ratio:

$$r_{swelling} = \frac{h_{swollen}}{h_{dry}}$$

The volume fraction of water within the poly(HPMA) layers was assessed by:

$$f_h = \frac{h_{swollen} - h_{dry}}{h_{swollen}}$$

$$f_{L-L\ EMA} = \frac{\left(\frac{n^2_{swollen} - n^2_{dry}}{n^2_{swollen} + 2n^2_{dry}}\right)}{\left(\frac{n^2_{H2O} - n^2_{dry}}{n^2_{H2O} + 2n^2_{dry}}\right)}$$

In the provided equation, f_h represents the volume fraction derived from the thicknesses of the poly(HPMA) layer in the swollen ($h_{swollen}$) and dry (h_{dry}) states. Additionally, $f_{L\text{-}L\ EMA}$ denotes the volume fraction of water calculated through the Lorentz-Lorenz effective medium approximation (EMA) using the refractive indexes of water (n_{H2O}), dry (n_{dry}), and swollen ($n_{swollen}$) poly(HPMA) layers.

The close match of the calculated volume fractions $f_{L\text{-}L\ EMA}$ and f_h suggests a weak correlation between the model-derived thicknesses and the corresponding optical dispersion functions, indicating the consistency of their values and low correlation.

3) Calculation of SPR sensitivity

The sensitivity of SPR measurements is influenced by the thickness and refractive index of the polymer overlayer, as well as the resonance wavelength. To address this, the sensor responses were individually calibrated for each chip using a theoretical model. Initially, reflectivity calculations were carried out utilizing the transfer-matrix method implemented in the EWA toolbox in Matlab. The considered geometry involved a stack comprising a semi-infinite dielectric layer (glass, refractive index: 1.51), a metal layer (gold, thickness: 48 nm, refractive index: interpolated from experimental data), dielectric layers (SiO_2, thickness: 15 nm, refractive index: 1.49; poly(HPMA) polymer, thickness and refractive index: interpolated from ellipsometric data), a dielectric overlayer (biomolecular layer, thickness: 7 nm; refractive index: 1.40, only for sensitivity calculation), and a semi-infinite dielectric layer (buffer; refractive index: 1.33). Next, sensitivity was calculated based on the reflectivity obtained with and without the dielectric overlayer. Sensitivity correction factors of 1.28, 1.10, 1.16, and 1.68 were obtained and employed to recalibrate the sensor response of SiO_2-coated SPR chips, poly(HPMA)

grafted-to SPR chips under GS and PS conditions, and poly(HPMA) grafted-from SiO_2-coated SPR chips, respectively. To convert the surface refractive-index change to the surface mass density, an experimental factor of 18 ng·cm^{-2}·nm^{-1} was utilized (valid at the wavelength of 750 nm).

4) Calculation of grafting density

The grafting density was calculated by the mass balance equation (Equation 1, See introduction, $\sigma = \frac{h\rho N_A}{M_n}$), with the layer thickness (*h)* in the dry state as determined by SE, the bulk density (ρ) of poly(HPMA) was taken to be 1.1 g·cm^{-3}, and N_A is the Avogadro constant. To obtain the grafting density from the thickness h and the number-average molar mass $M_{n,\,sur}$ (obtained by SMFS), the mass balance equation can be rewritten as:

$$M_n = \frac{1}{\sigma}(\rho N_A)h$$

By plotting $M_{n,\,sur}$ as a function of h and performing linear regression fit of the dependence $M_{n,\,sur}$ *vs* h (imposing a null y-axis intercept) we can obtain the grafting density σ.

5) Calculation of apparent propagation rate

The (SI)-RAFT polymerization follows near-linear pseudo-first-order kinetic, i.e. the termination and transfer reaction are suppressed. Assuming a fast initiation step, the rate of polymerization is given by:

$$R_p = -\frac{d[M]}{dt} = k_p[P^*][M]$$

where [M] is the monomer concentration, k_p is the rate constant of propagation, and [P*] is the concentration of active chain ends. In the absence or suppression of termination, [P*] is constant, and the product k_p [P*] can be regarded as an apparent polymerization rate constant ($k_{p,\,app}$). Introducing monomer conversion, and integrating $-\frac{d[M]}{dt}$ leads to:

$$ln\frac{[M]_0}{[M]_t} = k_p[P^*]t = k_{p,app}t$$

6) Interpretation of streaming current measured from EK

The streaming data measured for the poly(HPMA) brushes were analyzed applying the theory for the electrohydrodynamics of diffuse soft interfaces developed on Teflon, polystyrene, polyethylene glycol, etc. [87-96] The transport of mobile charges at the poly(HPMA) solution interphase gives rise to the streaming current, I_{str}. The transport depends on the hydrodynamic flow field, $V(X)$, and the distribution of mobile ions in the interfacial region between the polymer brush and the solution. The hydrodynamic flow field $V(X)$ can be calculated from the generalized Brinkman equation which models the hydrodynamic flow within swollen polymer materials according:

$$\frac{d^2V(X)}{dX^2} - \frac{(\lambda_o H)^2 f(X) V(X)}{1+\frac{3}{4}\Phi_o f(X)\left[1-\left(\frac{8}{\Phi_o f(X)}-3\right)^{1/2}\right]} = -1$$

where, $v(x)$ is the local velocity, $X = x/H$, $V(X) = v(x) / v_0$, $v_0 = \Delta P \cdot H^2/(\eta \cdot L_0)$. The function $\Phi_o f(X)$ corresponds to the adopted segment density profile which can be obtained on the basis of self-consistent field theory. This can be utilized to model I_{str}, resulting from the convective transport of mobile ions is then given by:

$$\frac{I_{str}}{\Delta P} = \frac{2\ell F H^3}{\eta L_o} \int_0^{\frac{1}{2}} V(X) \sum_{i=1}^{N} z_i c_i \exp\left(-z_i y(X)\right) dX$$

where F is the Faraday constant, η the viscosity of the electrolyte, c_i the concentration, z_i the valence and N the total number of ion species i in the electrolyte. The local electrostatic potential $y(X) = Fy(X)/RT$ was evaluated from the non-linear Poisson-Boltzmann equation, with y being the potential, R the universal gas constant and T the temperature. To obtain the streaming current, the whole set of equations was solved numerically using COMSOL Multiphysics 5.3.

The most outer region of the polymer brush, determines the electrohydrodynamics at the interface, making the EK measurements very sensitive to the actual structure of the polymer chains constituting the layer. For this purpose, we adopted the procedures developed by Zimmermann et al. [87, 91] These consider the monomer density profile and polydispersity effects of the layers for the purpose of evaluating the streaming current data and proving the structure of the polymer chains. Therefore, we calculated the normalized density brush profile based on the results obtained by AFM-SMFS for cca. 20 nm thick poly(HPMA) brushes. The normalized

density profile for the poly(HPMA) brushes was approximated on the basis of the self-consistent field method elaborated in several works of Milner et al. [97-100] This was achieved on the basis on numerical solution of the self-consistent potential $U(x)$ (proportional to the self-consistent density profile $\Phi(x)$) according[100]:

$$\frac{dz}{dU}(U) = \begin{cases} \frac{2^{1/2}}{2\pi A^{1/2}} \int_0^U dU' \frac{dn}{d\sigma}\left(\sigma(U')\right) \times (U-U')^{-1/2}(A-U')^{-1/2} \\ ,melt \\ \frac{3(2^{1/2})\sigma}{2\pi A^{3/2}} \int_0^U dU' \frac{dn}{d\sigma}\left(\sigma(U')\right) \times (U-U')^{-1/2}(A-U')^{-1/2} \\ ,moderate\ density \end{cases}$$

The obtained normalized density profile was converted in real segment densities and implemented in the analysis of the electrohydrodynamics data on non-charged interfaces. [87, 90, 91] The following parameters for the poly(HPMA) brushes were used: number average molar mass M_n = 42851 Da, dispersity $Đ$ = 1.32, chain grafting density σ = 0.33 chains·nm^{-1} and the average number of monomer units per polymer chain N_{av} =299 monomer units, (all calculated based on the SMFS-AFM and spectroscopic ellipsometry data), excluded volume parameter v = 0.048 nm^3 and a segment length b = 0.27 nm.

4. Results and Discussion

4.1. Surface-grafted poly(HPMA): Grafting-to *vs* Grafting-from

Antifouling polymer brushes play a crucial role in biomedical applications by preventing non-specific interactions with biological fluids. [3, 101] These brushes consist of polymer chains tethered to surfaces, commonly formed through either chemisorption (grafted to, GT) or surface-initiated (SI) polymerization (grafted from, GF). Despite extensive research on antifouling polymer brushes, a comprehensive comparison between GT and GF methods regarding their ability to resist fouling remains open questions. In this investigation, we explore the physical and antifouling properties of poly(HPMA) brushes synthesized using RAFT polymerization through both GT and GF methods.

This study compares poly(HPMA) brushes obtained through the GT and GF methods, ensuring comparable polymer molar mass, to investigate the impact of the grafting method on the antifouling effectiveness of the coating and its correlation with brush character. The assessment utilized atomic force microscopy-based single-molecule force spectroscopy (AFM-SMFS) to evaluate the molar mass of polymer chains synthesized on the surface via the GF method. [50, 59, 77, 102, 103] Crucially, the molar mass of the polymer for the GT method (monitored by size exclusion chromatography equipped with multiangle light scattering, SEC-MALS) was adjusted to match the molar mass of the GF-polymer brush (see Scheme 11).

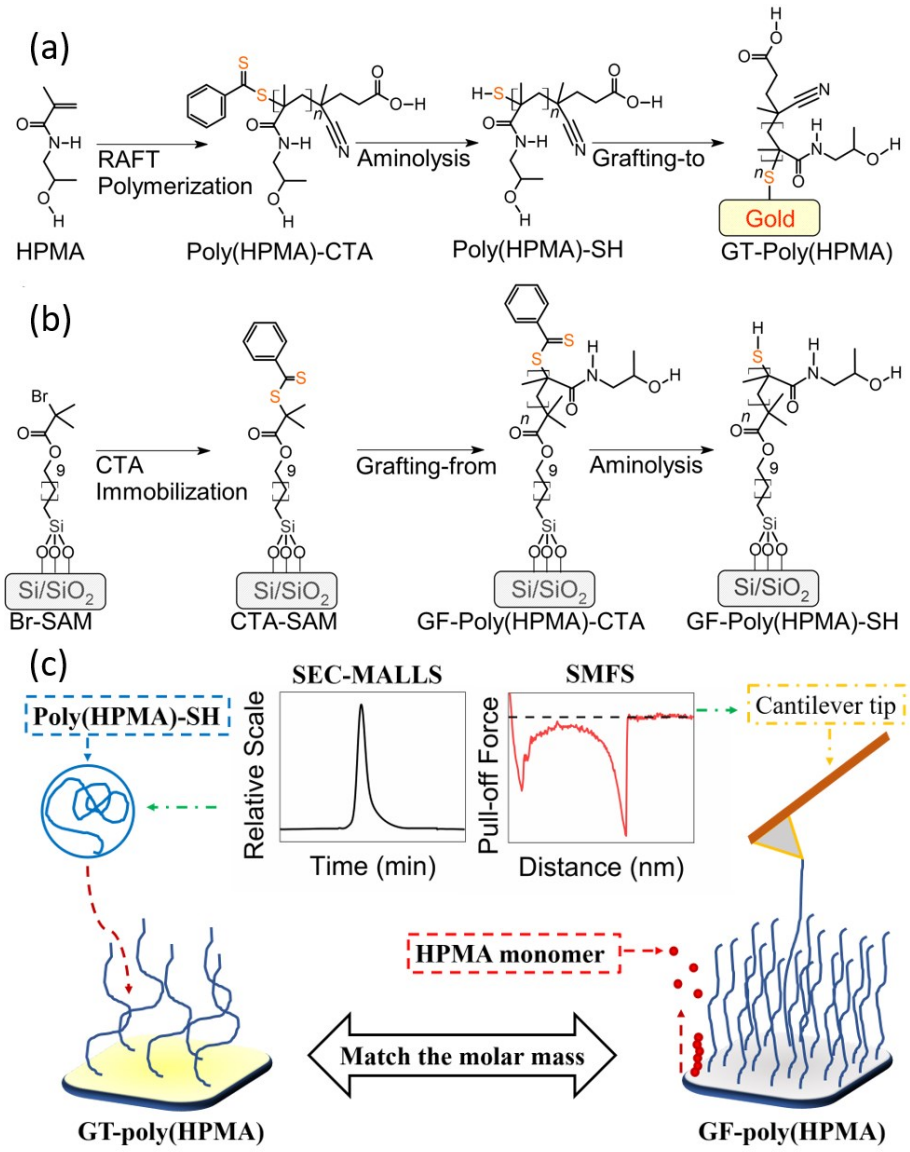

Scheme 11. Synthesis of poly(HPMA) brushes by (a) GT method and (b) GF method. (c) Comparison between GT and GF methods and respective molar mass characterization by SEC-MALS and SMFS. [59]

4.1.1. Poly(HPMA) brushes grafting-from surfaces

The GF-poly(HPMA) brushes were produced by initiating polymer chain growth through surface-initiated reversible addition−fragmentation chain-transfer (SI-RAFT) polymerization directly from a surface-bound CTA on a self-assembled monolayer (CTA-SAM) (see Scheme 11b). This CTA-SAM was derived by modifying a bromine-functional self-assembled monolayer (commonly used as an initiator in SI-ATRP polymerization, Br-SAM) through a straightforward

one-step reaction following a protocol based on the atom transfer radical addition mechanism. Due to the mechanism of SI-RAFT polymerization, poly(HPMA) simultaneously grows in solution from a sacrificial CTA, as well as from the surface. The course of polymerization was monitored by measuring the thickness of the polymer layer (via spectroscopic ellipsometry in the dry state) and the molar mass of the polymer in solution (via SEC-MALS). The polymer layer thickness increased with polymerization time, reaching 13.5 ± 0.2 nm at the reaction time of 24 hours (see Figure 8a). The molar mass of the polymer formed in solution increased with polymerization time, ranging from 4.8 to 47.0 kg·mol^{-1} between 1.5 and 24 hours, while maintaining a low dispersity ($Đ$) (see Figure 8b). Previous research on analogous brushes indicated that a layer thickness exceeding 10 nm imparts satisfactory resistance to fouling. Simultaneously, a thicker brush is linked to a higher molar mass of the grafted polymer. Consequently, we refrained from further increasing the thickness to avoid potential constraints associated with performing GT method using polymers with very high molar masses.

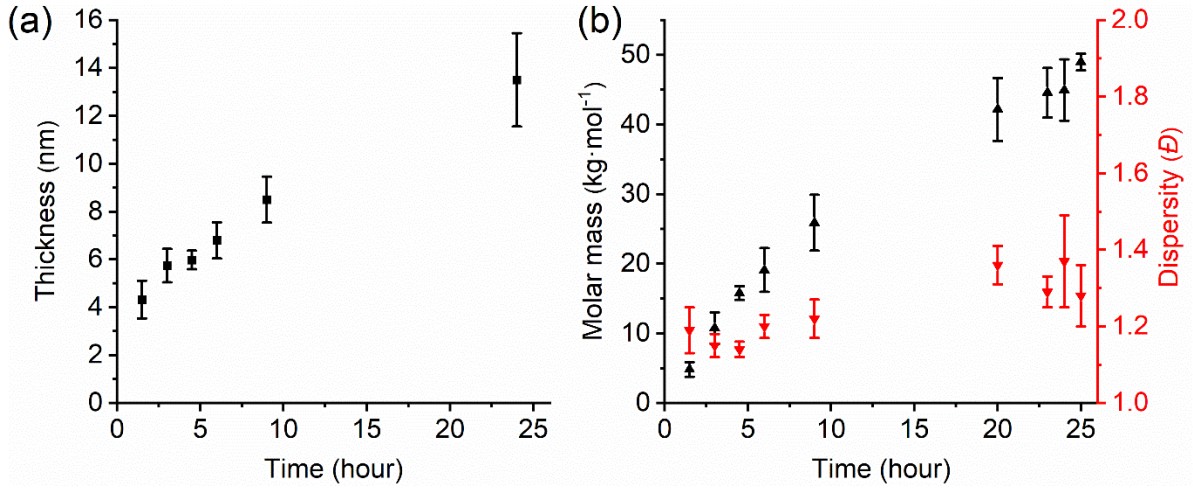

Figure 8. Kinetic plots: (a) thickness of GF-poly(HPMA) brushes in the dry state measured by spectroscopic ellipsometry. (b) Molar mass and $Đ$ of poly(HPMA) generated in the solution of (SI)-RAFT polymerization measured by SEC-MALS.

To precisely measure the molar mass of GF-poly(HPMA) grown from the surface, we utilized AFM-SMFS to obtain its contour length (l_c) for further calculation of molar mass (see Figure 9). In this technique, individual poly(HPMA) chains attach to the AFM tip from their end group, and the elastic force needed to stretch the chain is recorded as a function of the distance to the surface until the tip-polymer contact ruptures. The resulting curve can be fitted to the worm-like chain

(WLC) model (see Section 3.3.2(1)), enabling the determination of the l_c of polymer chains, which is then used to derive the number-average molar mass (M_n). To enhance binding with the gold-coated AFM cantilever tip during SMFS measurements, the CTA end groups in the initially prepared poly(HPMA) brushes were transformed into thiol (poly(HPMA)-SH) through aminolysis. In contrast, the CTA-capped end groups of the GF polymer brushes used for other measurements were not aminolyzed to prevent potential disulfide formation, which could lead to the creation of polymer loops and alter the layer architecture.

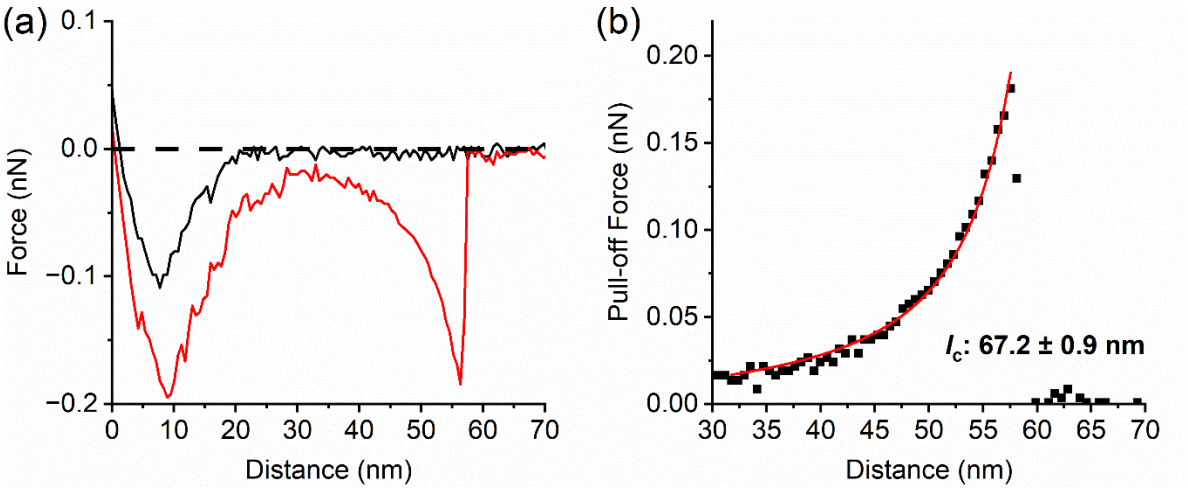

Figure 9. (a) Representative force–distance curve of selected clear unfolding and rupture event during approach (black) and retraction (red). (b) Characteristic pull-off force curve (black square symbol) with the fitting of WLC model (red line).

Directly measuring the molar mass of the polymer grown on the surface is crucial to ensuring the validity of the comparison between GF and GT-formed polymer layers. The GF-poly(HPMA) brushes, with a thickness of 13.5 ± 0.2 nm, exhibited a number-average l_c of 67.2 ± 0.9 nm, corresponding to an $M_{n,\,sur,\,24h}$ of 49.0 kg·mol^{-1} with a $Đ$ of 1.14. The molar mass of poly(HPMA) collected in solution at the same polymerization time during SI-RAFT polymerization was $M_{n,\,sol,\,24\,h}$ = 44.6 kg·mol^{-1} with a $Đ$ of 1.38. The molar mass discrepancy between the polymer formed on the surface and in solution was only around 10%. However, it is crucial to note that other studies have reported substantial variations in polymerization kinetics between surface and solution, leading to more significant discrepancy in molar mass. These differences were attributed to mass transport limitations and the crowded environment at the interface. Herein, we hypothesized that the slow polymerization kinetics of HPMA under the selected conditions, along with the

concomitant long polymerization time to achieve the targeted thickness, may have mitigated the limiting effect of diffusion observed in other GF polymerizations. A further discussion of the discrepancy between GF and solution-generated polymers during SI-RAFT polymerization was carried out at Section 4.2.

4.1.2. Poly(HPMA) brushes grafted-to surfaces

The poly(HPMA) synthesized for the GT method was produced through RAFT polymerization and subjected to NMR characterization to verify the success of the polymerization. Our aim was to achieve a molar mass for the GT-poly(HPMA) brushes that closely matched that of the GF-brushes ($M_{n,\,GF}$ = 49.0 kg·mol^{-1}). To achieve this, we slightly extended the RAFT polymerization time compared to the conditions used for the GF-poly(HPMA) brushes, collecting the poly(HPMA) formed in solution at 25 hours for use in the GT method.

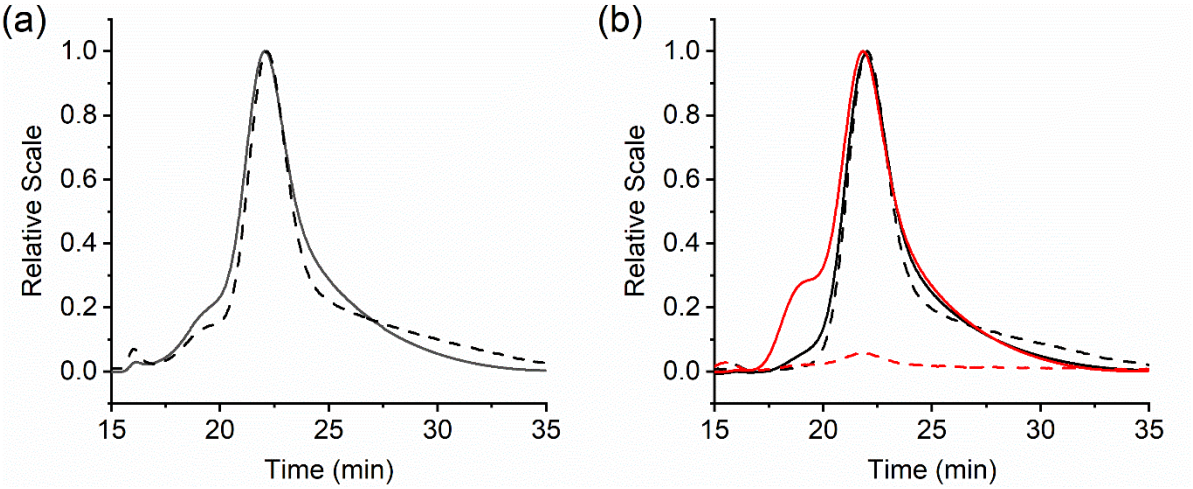

Figure 10: SEC-MALS chromatograms of poly(HPMA) (solid line: differential refractometer detector, dash line: UV detector). (a) Poly(HPMA) collected in solution during (SI-)RAFT (M_n = 47 kg·mol^{-1} with a $Đ$ = 1.46). (b) Poly(HPMA) (M_n = 49 kg·mol^{-1} with a $Đ$ = 1.18) prepared by RAFT polymerization for GT method before (black) and after aminolysis (red).

The molar mass of this polymer was determined via SEC-MALS analysis, yielding $M_{n,\,GT}$ = 49.0 kg·mol^{-1} with a $Đ$ of 1.18. Before the GT procedure, the CTA end groups of the obtained polymer underwent aminolysis to form thiols, known for their strong binding to gold surfaces, providing a stable attachment for the GT-poly(HPMA) brushes. Importantly, the aminolysis reaction did not induce any undesired changes in the molar mass or chemical structure, as

confirmed through SEC-MALS (see Figure 10) and NMR analyses (see Figure 11). At Figure 11, we successfully observe the phenyl group of CTA moiety disappeared after aminolysis while remaining the other chemical shift unchanged.

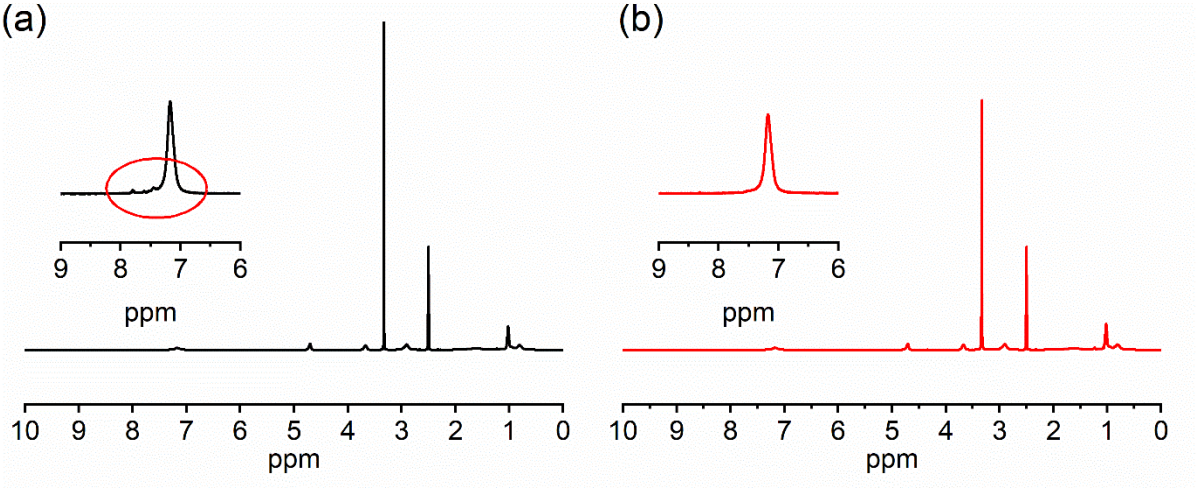

Figure 11: NMR spectra of (a) poly(HPMA)-CTA and (b) poly(HPMA)-SH. Note: The molar mass of poly(HPMA) presented here is M_n 17.0 kg·mol^{-1} instead of M_n 49.0 kg·mol^{-1} because of the relatively low proton integral value of phenyl group of CTA moiety to be observed at 7.5- 8 ppm for the disappearance.

Poly(HPMA)-SH was grafted onto gold surfaces under two distinct sets of conditions, characterized by the thermodynamic quality of the solvent concerning poly(HPMA): "good solvent" (GS) and "poor solvent" (PS, *Note*: *not to be confused with polystyrene* which has not been used in this dissertation). In the GS conditions, the gold surfaces were immersed for 20 hours in a poly(HPMA)-SH solution in Milli-Q water with concentration of 1 mg·mL^{-1}. This straightforward method serves as a reference for comparing with other polymer brush coatings. In contrast, grafting under PS conditions is anticipated to result in a smaller packing distance and higher grafting density. As the polymer chains shrink and adopt a more compact conformation, they can densely pack on the surface during grafting due to reduced steric hindrance. PS conditions were achieved by adjusting the solvent quality with the addition of salt (Na_2SO_4) and raising the temperature until turbidity appeared, reaching the so-called "cloud point". Although similar PS conditions have been reported for PEG, they are rarely applied to other polymers. Grafting of PEG under PS conditions

in other literature indicated a higher grafting density and led to an enhanced fouling resistance. [78] Therefore, it is expected that PS-grafted poly(HPMA) brushes will exhibit higher grafting density and superior antifouling performance compared to GS grafting. The key question is how these properties compare to chemically comparable brushes obtained via SI-RAFT polymerization. By comparing these two grafting systems with grafted chains of comparable molar mass, we can gain insights into the impact of the grafting method on fouling resistance and surface physical parameters.

4.1.3. Comparison of their physical parameters and fouling resistance

4.1.3.1. The comprehensive physicochemical characterization of GT- and GF-poly(HPMA) brushes by X-ray photoelectron spectroscopy and Fourier-transform infrared spectroscopy

The chemical characterization of the grafted poly(HPMA) layers was conducted using X-ray photoelectron spectroscopy (XPS). In the high-resolution XPS spectra of the C 1s region (see Figure 12), all three types of poly(HPMA) brush coatings exhibited identical features, including C–C and C–H (285.0 eV), C–C=O (285.4 eV), C–N (286.1 eV), C–O (286.4 eV), and N–C=O (288.1 eV). In the poly(HPMA) brushes prepared via the GF method, XPS measurements also identified the presence of CTA end groups. The reduction in sulfur content following the aminolysis reaction before SMFS measurements indicated the successful removal of CTA, with thiol remaining as the polymer end group (see Figure 13). Moreover, the overall composition of poly(HPMA) remained unchanged, confirming that the aminolysis process did not introduce any undesired alterations to the polymer layer intended for SMFS analysis. In addition to the observations in the C 1s region for GT-poly(HPMA) brushes, high-resolution XPS spectra of the S 2p region further confirmed the covalent attachment of thiol end groups to the gold substrate. Specifically, after the GT anchoring reaction, shifts in binding energies were observed from the characteristic free C–S–H thiol contribution at 163.4 eV to C–S–Au thiolate at 161.9 eV.

Fourier-transform infrared spectroscopy (FTIR) provided additional confirmation of the successful achievement of the targeted chemical modifications of polymer brushes prepared by different methods (see Figure 14).

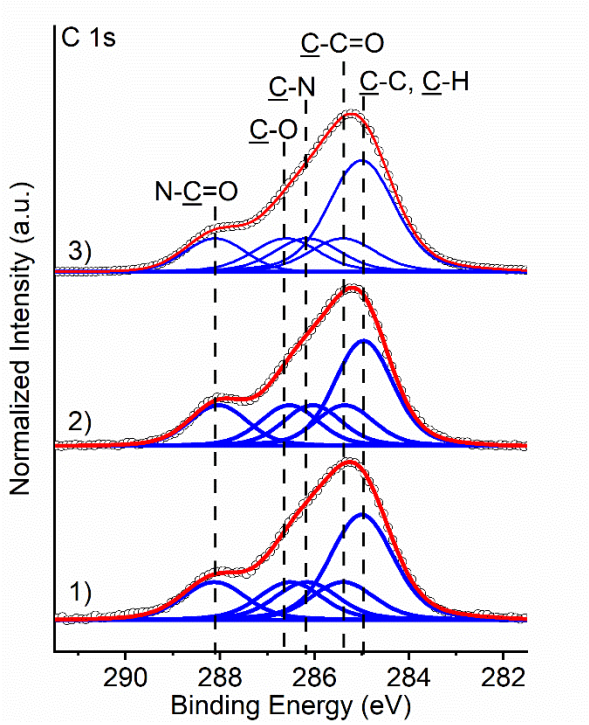

Figure 12. XPS characterization of each grafted poly(HPMA) layer. High-resolution XPS spectra of C 1s region for the GT-GS-poly(HPMA) on gold substrates (1), GT-PS-poly(HPMA) on gold substrates (2), and GF-poly(HPMA) on silicon substrates (3). (*Note: Measured high-resolution C 1s spectra are presented with open circles, while their corresponding fitted envelopes are presented with red lines. The individual contributions of different functional groups are represented with blue lines.)*

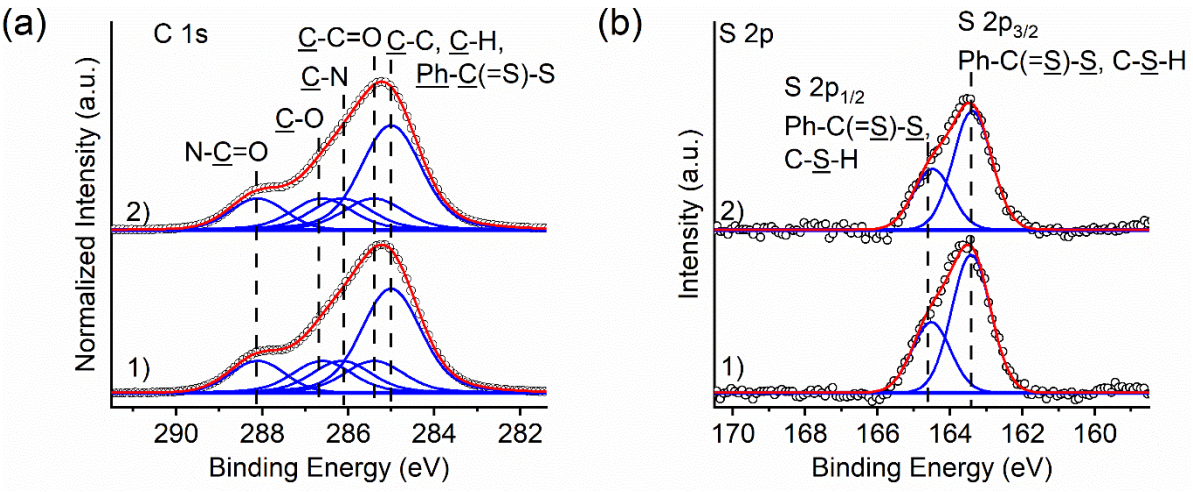

Figure 13: XPS proves the preserved chemical structure of the GF-poly(HPMA) brush and points to the successful aminolysis of CTA to thiol at the distal chain-end. The high resolution XPS spectra of (a) C 1s and (b) S 2p regions for the GF-poly(HPMA)-CTA (1) and GF-poly(HPMA)-SH (2).

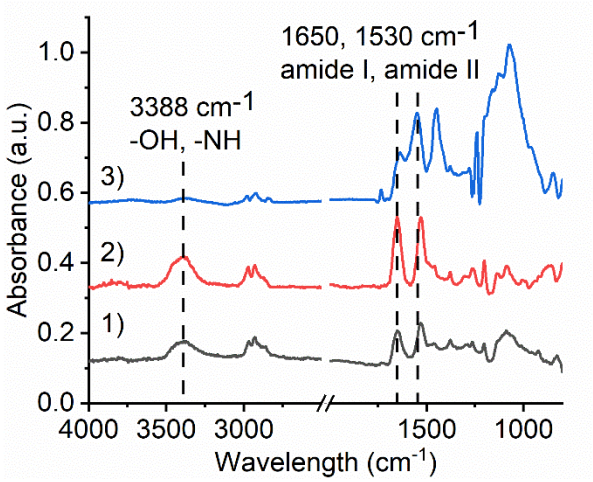

Figure 14. FTIR spectra of GT-GS-poly(HPMA) on gold substrates (1), GT-PS-poly(HPMA) on gold substrates (2), and GF-poly(HPMA) on silicon substrates (3). (*Note: the GF-poly(HPMA) brushes were measured in the GAATR mode, while the GT were obtained in the GASR mode)*.

4.1.3.2. The physical parameters and swelling behavior of poly(HPMA) prepared by GT and GF methods

Spectroscopic ellipsometry was employed to measure the thickness of GT- and GF-poly(HPMA) brushes in both the dry (h_{dry}) and swelling ($h_{swollen}$) states. Since the molar mass of poly(HPMA) is consistent across the three brush types, a greater thickness indicates a higher number of polymer chains per unit area, indicating an increased grafting density. In the case of GT-GS-poly(HPMA), the dry thickness measured 2.0 ± 0.1 nm, corresponding to 0.02 polymer chains per nm^2, and a grafting distance (D) of 7.2 nm. This distance is smaller than the dimensions of the polymer coil in solution, suggesting slight chain stretching in this layer. Conversely, GT-PS-poly(HPMA) exhibited a larger dry thickness (4.1 ± 0.4 nm), reflecting a higher grafting density and a more stretched chain conformation, indicative of a pronounced brush character. Evidently, the poly(HPMA) chains in GT were more closely packed due to the influence of added salt and elevated temperature. This phenomenon can be attributed to the collapse of the poly(HPMA) conformation under PS conditions, reducing steric hindrance during grafting, similar to previous findings reported for PEG.

The dry thickness of GF-poly(HPMA) brushes measured 13.5 ± 0.2 nm, with a grafting density of 0.18 chains per nm^2, which is over three times higher than that of the GT-PS brush. The more densely packed GF-layer, even compared to the optimized GT method, is attributed to the fundamentally different mechanism governing the formation of polymer brushes in the GF process. Unlike GT, where fully formed polymer chains must diffuse to the surface for their end groups to react with the substrate, GF involves only the monomers reaching the surface and contributing to polymerization growing centers. The faster diffusion of monomers, facilitated by their small size and high concentration, explains the closer packing observed in the GF-layer.

The effectiveness of polymer brush layers in resisting fouling in aqueous solutions also relies on their hydrophilicity. To assess this, we conducted *in situ* ellipsometry to measure the water uptake of poly(HPMA) brushes. The swelling ratio ($h_{swollen}/h_{dry}$) reflects the balance between enthalpic gain from favorable water-polymer interactions and entropic penalties from an increasingly stretched polymer conformation (see Section 3.3.2(2)). Remarkably, the swelling ratio in water varies across different brush layers: 6.5 for GT-GS, 4.4 for GT-PS, and 2.1 for GF-poly(HPMA) (Table 1), despite all layers consisting of chemically identical chains with

comparable molar mass. This discrepancy arises from differences in grafting density influenced by grafting methods. In denser GF brushes, grafting sites are closer, resulting in a more stretched polymer conformation even in the dry state. In contrast, GT-layer polymer chains can swell more upon water contact, as they are stretched less in the dry state. The higher swelling ratio in GT layers is coupled with a lower refractive index in the swollen state, approaching that of water, indicating a lower polymer volume fraction in swollen layers. This underscores the significant impact of the grafting method on the behavior of surface-bound polymer chains in an aqueous environment, as revealed through the physical characterization of poly(HPMA) layers prepared by GT and GF methods.

Table 1. Polymer surface parameters of grafted poly(HPMA) layers by different grafting methods.

Poly(HPMA)	M_n[a, b] (kg·mol^{-1})	h_{dry} (nm)	σ (chain·nm^{-2})	D (nm)	$D/2R_g$	$h_{swollen}$ (nm)	Swelling Ratio
GT-GS	49.0	2.0 ± 0.1	0.02	7.2	0.49	13.2 ± 0.4	6.5 ± 0.3
GT-PS	49.0	4.1 ± 0.4	0.05	5.0	0.34	18.1 ± 2.1	4.4 ± 0.4
GF	49.0	13.5 ± 0.2	0.18	2.6	0.18	27.2 ± 0.3	2.1 ± 0.1

[a] Number-average molar mass was measured by SEC-MALLS. [b] Number-average molar mass was calculated from the contour length obtained by SMFS.

Note: The degree of polymerization of utilized poly(HPMA) is 340.

4.1.3.3. Fouling resistance of GT- and GF-poly(HPMA) brushes

We conducted a comprehensive investigation into the antifouling performance of poly(HPMA) coatings prepared by GT and GF fully characterized at previous sections. We utilized surface plasmon resonance (SPR) to quantify the mass of protein adsorbed from various single-protein solutions and blood plasma. Employing SI-RAFT polymerization along with simultaneous characterization through SEC-MALS and SMFS enabled a direct comparison between GT- and GF-poly(HPMA) brushes while maintaining comparable molar mass. This approach sheds light on the impact of the chosen grafting methods on the antifouling properties of the polymer brushes.

We conducted measurements of adsorption from solutions containing human serum albumin

(HSA, 5 mg·mL^{-1}), human fibrinogen (Fbg, 1 mg·mL^{-1}), and undiluted human blood plasma (HBP, pooled from 5 donors) using SPR. This technique relies on detecting changes in the refractive index in the immediate vicinity of a bare or coated sensor surface, indicating the deposition of proteins. However, the sensitivity of SPR is influenced by the presence of a SiO_2 and/or polymer layer, as protein adsorption occurs farther away from the SPR sensor's gold surface. To ensure a valid comparison of fouling on poly(HPMA) coatings of various thicknesses with the bare gold and SiO_2 sensor surfaces, we employed modeling to account for changes in sensitivity for each type of coating (see Section 3.3.2(3)). The resulting corrections allowed us to obtain the actual value of adsorbed protein mass on the surface, facilitating an accurate assessment of protein adsorption on different surfaces.

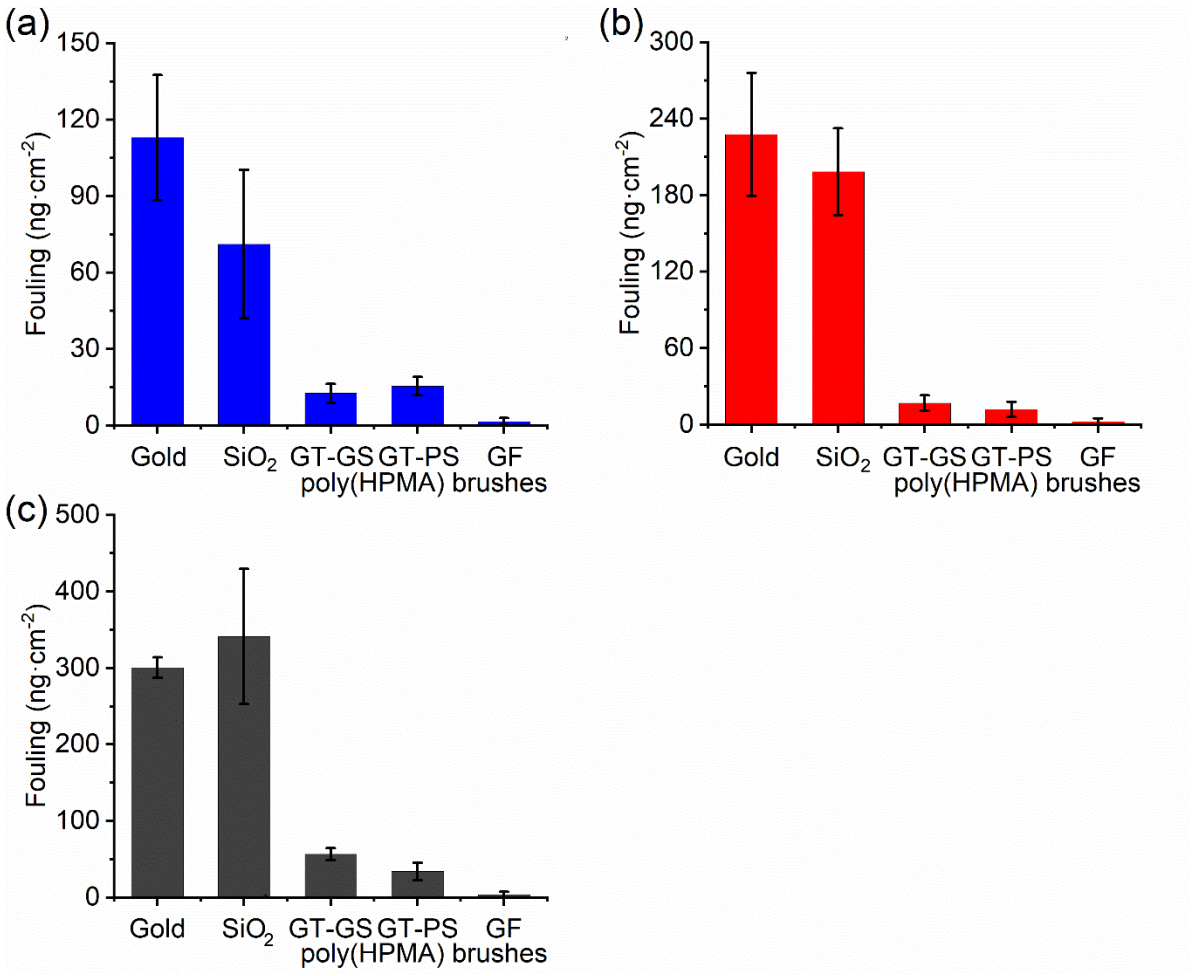

Figure 15. Non-specific protein adsorption of (a) human serum albumin (HSA, 5 mg·mL^{-1}), (b) fibrinogen (Fbg, 1 mg·mL^{-1}), and (c) human blood plasma (HBP).

Both HSA and Fbg solutions quickly led to fouling of the bare gold SPR chips (see Figure 15a and b). SiO_2-coated SPR chips exhibited lower adsorption of individual proteins compared to gold, possibly due to their strong hydrophilic character and negative charge, with isoelectric points of 4.9, 5.8, and 3.9 for HSA, Fbg, and SiO_2, respectively. Remarkably, poly(HPMA) brushes prepared using the GT-GS method significantly reduced fouling by 89% and 93% for HSA and Fbg, respectively, compared to bare gold, despite being only 2-nm-thin in the dry state. GT-PS-brushes demonstrated a similar performance, achieving reductions of 86% and 95% for HSA and Fbg, respectively. In the challenging case of HBP, both bare gold and SiO_2 exhibited substantial fouling at the level of a protein monolayer (see Figure 15c). SiO_2's hydrophilicity was insufficient to reduce HBP fouling compared to gold. Conversely, GT-GS- and GT-PS-brushes suppressed fouling by 81% and 89%, respectively, even in the complex HBP environment. The superior antifouling performance of GT-PS, likely due to over two-fold higher grafting density, stood out against HBP.

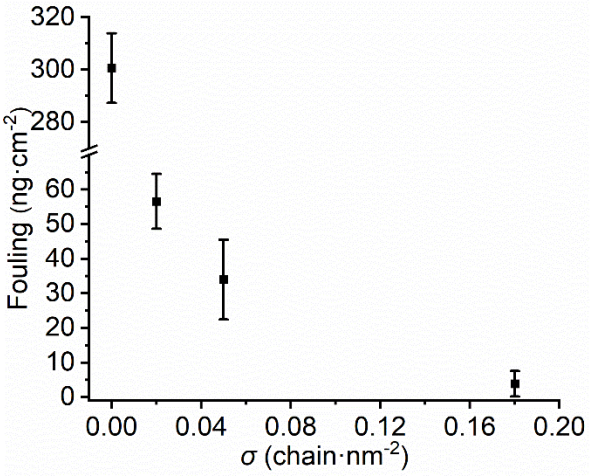

Figure 16. Dependence of resistance to fouling from HBP with increasing grafting densities of poly(HPMA) brushes.

Poly(HPMA) brushes prepared by SI-RAFT polymerization in the GF approach remarkably reduced fouling from single-protein solutions by 99% compared to bare gold. When compared to GT-coatings, the fouling on GF-coatings from HSA and Fbg solutions was 5 and 8 times lower, respectively, reflecting the significantly higher grafting density of GF-coatings despite the comparable polymer molar mass. This difference was even more pronounced for HBP, where the GF-coating reduced non-specific adsorption by over 99%, rivaling the best antifouling surfaces reported in the literature and outperforming GT-GS by 15 times and GT-PS by 9 times. This

underscores the crucial role of the much higher grafting density achievable in the GF method in enhancing fouling resistance (see Figure 16). The comparison of antifouling properties between poly(HPMA) brush layers prepared using the GT and GF methods underscores the critical role of the grafting method in defining coating properties. With identical polymer chemical structure and molar mass, the grafting method emerges as the decisive factor in achieving a high grafting density. The results clearly demonstrate that this difference results in markedly superior fouling resistance for GF-poly(HPMA) brushes. On the flip side, GT-derived layers offer a much lower thickness, potentially advantageous for specific applications, and are easily obtained through a straightforward method.

4.1.4. Summary

We investigated the impact of grafting methods on the fouling properties of poly(HPMA) brushes prepared through both conventional and surface-initiated RAFT polymerization. These brushes comprised polymer chains of comparable chemical composition and polymer molar mass, as confirmed by measurements using SEC-MALS and AFM-SMFS. While both types of coatings significantly reduced fouling from blood plasma, the GF method exhibited much greater efficacy in suppressing fouling compared to the GT method.

The superior antifouling performance observed with the GF method was attributed to a higher grafting density of the polymer brush. This increased grafting density correlated with a substantially lower swelling in water, a consequence of reduced polymer conformational freedom. In summary, the findings reveal that the choice of the grafting method has a significant impact on the maximum achievable grafting density and, consequently, the resistance to non-specific protein adsorption.

4.2. Solvent Effects during SI-RAFT Polymerization of poly(HPMA)

For years, there has been ongoing debate regarding the discrepancy in molar mass between grafted-from and solution-born polymers concomitantly produced during SI polymerization. Previous study (Section 4.1) have shown minimal differences between solution-born and grafted-from poly(HPMA) chains via SI-RAFT under polar and protic solvent conditions. However, experimental studies have revealed significant disparities between the molar masses of surface-grafted polymers and those grown concurrently in solution during SI polymerization, contrary to

the assumption of some researchers. [104] Genzer's and Spencer's groups have linked this contrast to "crowding," a phenomenon observed during SI-ATRP polymerization, especially under conditions of high grafting densities and/or rapid propagation rates. [60, 61] Crowding hampers mass transfer at the surface, resulting in a slower propagation rate compared to that in the solution phase. Integrating the crowding effect phenomenon with these findings, we hypothesize that the limited discrepancy arises from a sluggish propagation rate in solution under previous conditions. Consequently, we propose an experimental strategy to monitor the variance between polymers obtained on surfaces and in solution during SI-RAFT polymerization by manipulating the propagation rate through solvent effects.

4.2.1. Strategy of utilizing solvent effects on kinetic relationship by DMF/Water systems

Our focus was on the influence of solvent composition, given the critical role demonstrated by Thang and colleagues in conventional solution-based RAFT polymerization of HPMA. [105] By adjusting the solution propagation rate through solvent effects, we observed differences in molar mass between polymers grown in solution and on the surface. The conditions employed for SI-RAFT polymerization of HPMA varied only in the composition of the solvent, utilizing mixtures of water with either DMF (polar, aprotic) or 1,4-dioxane (non-polar, aprotic) (refer to Table 2; pure 1,4-dioxane was excluded due to incomplete solubility of the monomer).

Table 2. Solvent conditions of SI-RAFT polymerization of HPMA.[*, **]

Entry	Solvent composition		Designation	k_{app} (min^{-1})
1	DMF 100%	Water 0 %	DMF 100%	0.0013
2	DMF 75%	Water 25%	DMF 75%	0.0023
3	DMF 50%	Water 50%	DMF 50%	0.0026
4	DMF 25%	Water 75%	DMF 25%	0.0035
5	1,4-dioxane 75%	Water 25%	1,4-Dioxane 75%	0.0028
6	1,4-dioxane 50%	Water 50%	1,4-Dioxane 50%	0.0046
7	1,4-dioxane 25%	Water 75%	1,4-Dioxane 25%	0.0039

*AIBN and CTA are insoluble in pure water

**HPMA monomer is only partially soluble in pure 1,4-dioxane

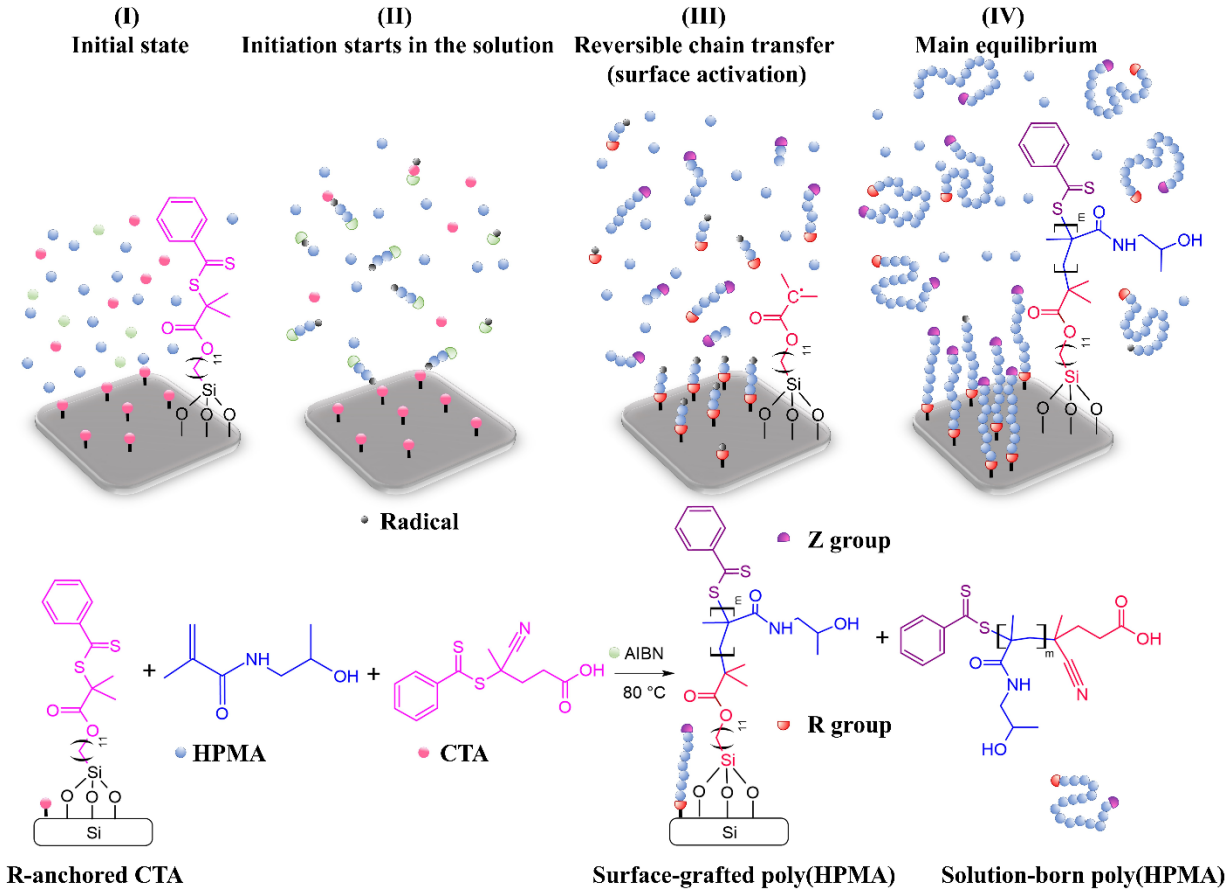

Scheme 12. Illustration and chemical structure of the concomitant propagation on the surface and in the solution during SI-RAFT polymerization of HPMA.

During the process, poly(HPMA) was simultaneously grown in solution and on the surface from sites of CTA attachment. While the solution-phase RAFT polymerization follows a well-established mechanism, on the surface, the initiation process slightly differs. In our study, the R-group of the CTA was covalently bonded to the surface (I). Initially, radicals are formed in solution (II) and transfer reversibly to the thiocarbonylthio (S=C-S) moiety of the surface-bound CTA, leaving behind a radical in the surface-anchored R-group (II). Subsequently, surface propagation (III) commences, involving the diffusion of HPMA monomer to the radical-bearing R-group on the surface. Through this mechanism, grafted-from and solution-born polymers grow concurrently (IV) via SI-RAFT polymerization (see Scheme 12).

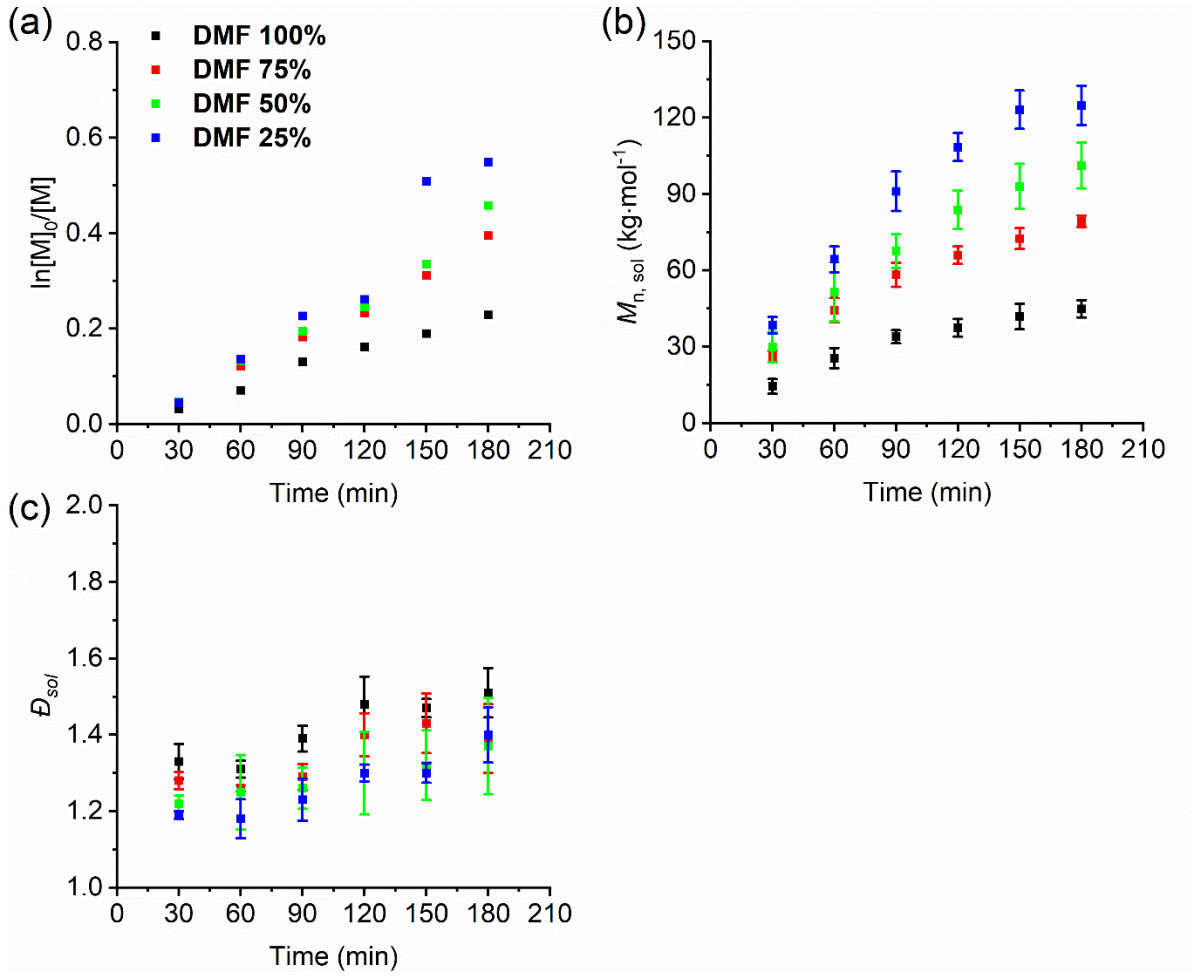

Figure 17. Kinetic plots of the solution-born poly(HPMA) via SI-RAFT polymerization in the DMF/water system: (a) conversion, (b) $M_{n,\,sol}$, and (c) dispersity against time.

Initially, our focus was on primarily altering the proticity of the solvent by employing mixtures of DMF and water (refer to Table 2, entries 1-4). We monitored the molar mass and dispersity of the polymer grown in solution using SEC-MALS. For each DMF/water composition, the solution polymerization exhibited nearly linear pseudo-first-order kinetics, indicating controlled radical polymerization (refer to Figure 17a and b) with narrow dispersity (refer to Figure 17c). Compared to pure DMF, the conversion increased by 1.6, 1.8, and 2.1 times, and the molar mass increased by 1.5, 2.3, and 2.8 times in the solution when the water content changed to 25%, 50%, and 75%, respectively. We conducted a linear regression fit of the conversion plots to obtain the apparent propagation rate constant, k_{app} (see Section 3.3.2(5)). k_{app} gradually increased with the rise in solvent proticity, i.e., a higher percentage of water present in the polymerization mixture (refer to

Table 2). These findings align with Thang's study, indicating that a higher water content in the solution is advantageous for controlling the RAFT polymerization of HPMA. Their research included temperature-dependent NMR experiments and computational simulations, which provided evidence that in an aprotic solvent, intra- and intermolecular hydrogen bonding between polymer chains and monomer leads to retardation due to hindered fragmentation of the RAFT adduct. Increasing the water content in the solution alleviates this retardation effect.

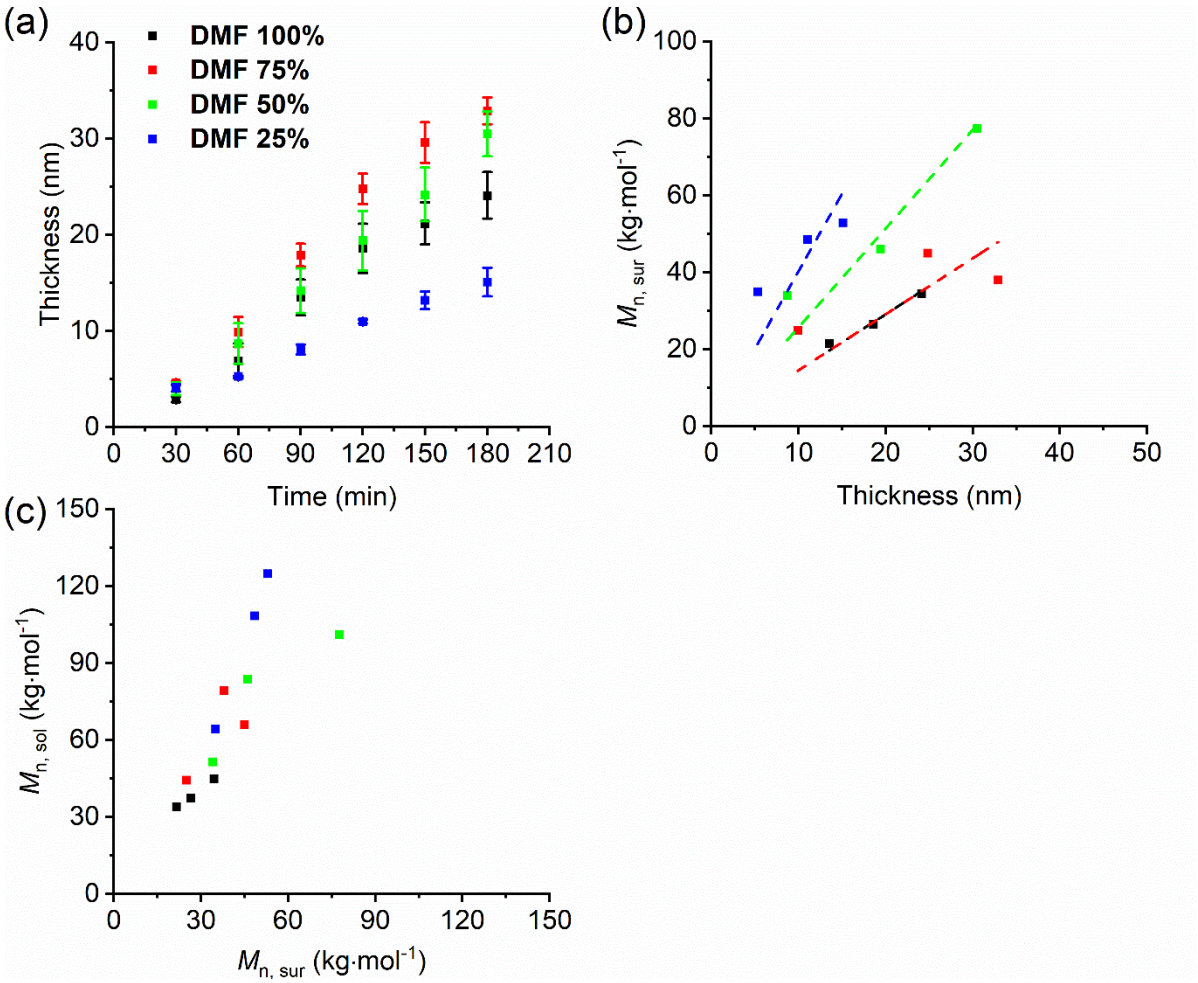

Figure 18. Kinetic plots of the grafted-from poly(HPMA) via SI-RAFT polymerization in the DMF/water system: (a) dry thickness against time, (b) $M_{n,\,sur}$ as a function of dry thickness (the dash lines represent the linear regression fits intercepting zero), and (c) the relation between $M_{n,\,sol}$ and $M_{n,\,sur}$.

To analyze the surface-grafted polymers, we monitored the progress of polymerization on the surface by measuring the dry thickness of the polymer layer using spectroscopic ellipsometry (refer

to Figure 18a). Indeed, the thicknesses obtained after 180 minutes under conditions of DMF 75% (32.2 nm) and DMF 50% (25.6 nm) were 1.3 and 1.1 times higher than for DMF 100% (24.2 nm), respectively. However, at the highest water content, DMF 25% (14.8 nm), the thickness was thinner than that of DMF 100% by 0.6 times. This indicates that there is less polymer formed on the surface at the highest solvent water content than in pure DMF, despite the enhanced propagation rate observed in solution.

To characterize the molar mass of the grafted-from polymers, we utilized AFM-SMFS to obtain the contour length distribution from each solvent condition. The force-distance curves depicting rupture events during retraction of the AFM tips were fitted according to WLC model (see Section 3.3.2(1)) to obtain the contour length, l_c for each sampled polymer chain and calculate the number-average molar mass, $M_{n,\,sur}$. Increasing the water content in the polymerization mixture leads to an increase in $M_{n,\,sur}$, consistent with the observed faster propagation in solution. However, $M_{n,\,sur}$ exhibited a decreased propagation rate at condition DMF 25% compared to DMF 50%. This could be attributed to mass transfer limitations: while the propagation rate increases both in solution and on the surface, the high local concentration of growing polymer chains on the surface rapidly depletes the monomer concentration in the interface region. As propagation rates increase, the diffusion of reactants to the surface likely creates a bottleneck for the continued growth of polymer on the surface, causing it to lag behind solution propagation as solvent proticity increases. Additionally, increasing water content in the polymerization leads to increased conversion in solution, which could be associated with an increase in solution viscosity.

We hypothesized that this increase in viscosity could further limit mass transfer to the surface, as the rate of diffusion has an inverse dependence on viscosity, which poses a frictional resistance to diffusion. To explore this possibility, we measured the dynamic viscosity of the DMF/water polymerization system. Figure 19 depicts the shear rate dependence of the dynamic viscosity in various poly(HPMA) DMF/water solutions at various polymerization times. We observed an increase in dynamic viscosity with increased reaction time and water content progressively, suggesting that higher conversion and associated larger viscosity could contribute to increased mass transfer limitations at high water contents. Moreover, the shear-thinning behavior of the solutions at high DMF/low water content may indicate interactions such as hydrogen bonding between the polymer, monomer, and solvent molecules. At higher water contents, these

interactions are disrupted, as evidenced by a shift in the dependence of dynamic viscosity on shear rate, transitioning from shear-thinning behavior (DMF 100% and DMF 75%) to Newtonian fluid behavior (DMF 50% and DMF 25%). This observation aligns with the conclusions from Thang and colleagues regarding solution RAFT polymerization of HPMA, where the disruption of these hydrogen-bonding interactions was found to be the primary mechanism by which water alleviates retardation and promotes faster propagation.

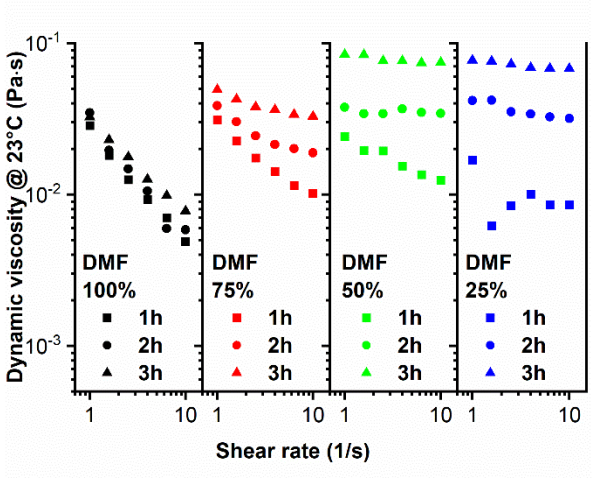

Figure 19. Shear rate dependence of dynamic viscosity in various poly(HPMA) DMF/water solutions at 23 °C.

The paradoxical tendency of thickness, reaching a maximum for condition DMF 75% but decreasing for conditions DMF 50% and DMF 25%, despite faster propagation in solution, cannot be solely explained by $M_{n,\,sur}$. The amount of polymer formed on the surface is determined not only by $M_{n,\,sur}$ but also by the number of chains on a given surface area, i.e., the polymer grafting density. We calculated the grafting density in each condition by plotting $M_{n,\,sur}$ against the dry thickness and performing a linear regression fit using mass balance equation (see Section 3.3.2(4)). Interestingly, conditions DMF 100% and DMF 75% provided a comparable grafting density of 0.45 but increasing water content led to lower grafting densities of 0.26 and 0.16 for DMF 50% and DMF 25%, respectively (see Figure 18b). In addition to its influence on the propagation rate, increased solvent proticity may also affect the polymerization on the surface through a distinct mechanism. By disrupting polymer-polymer and polymer-monomer hydrogen bonding interactions on the surface, increased water content promotes solvent interactions with the grafted polymer. Consequently, the grafted poly(HPMA) chains would swell and stretch more due to

increased uptake of solvent molecules, creating more steric hindrance with increasing water content (see Scheme 13). This limits the ability of the poly(HPMA) chains to grow in close proximity to each other, lowering the grafting density. On the other hand, in pure DMF, the poly(HPMA) chains would tend to form hydrogen bonds between the side chains and adopt a more compact conformation. Thus, the polymer chains can grow closely together and reach a high grafting density. The lower grafting density in conditions DMF 50% and DMF 25% explains the decreasing thickness despite the faster polymerization kinetics in solution.

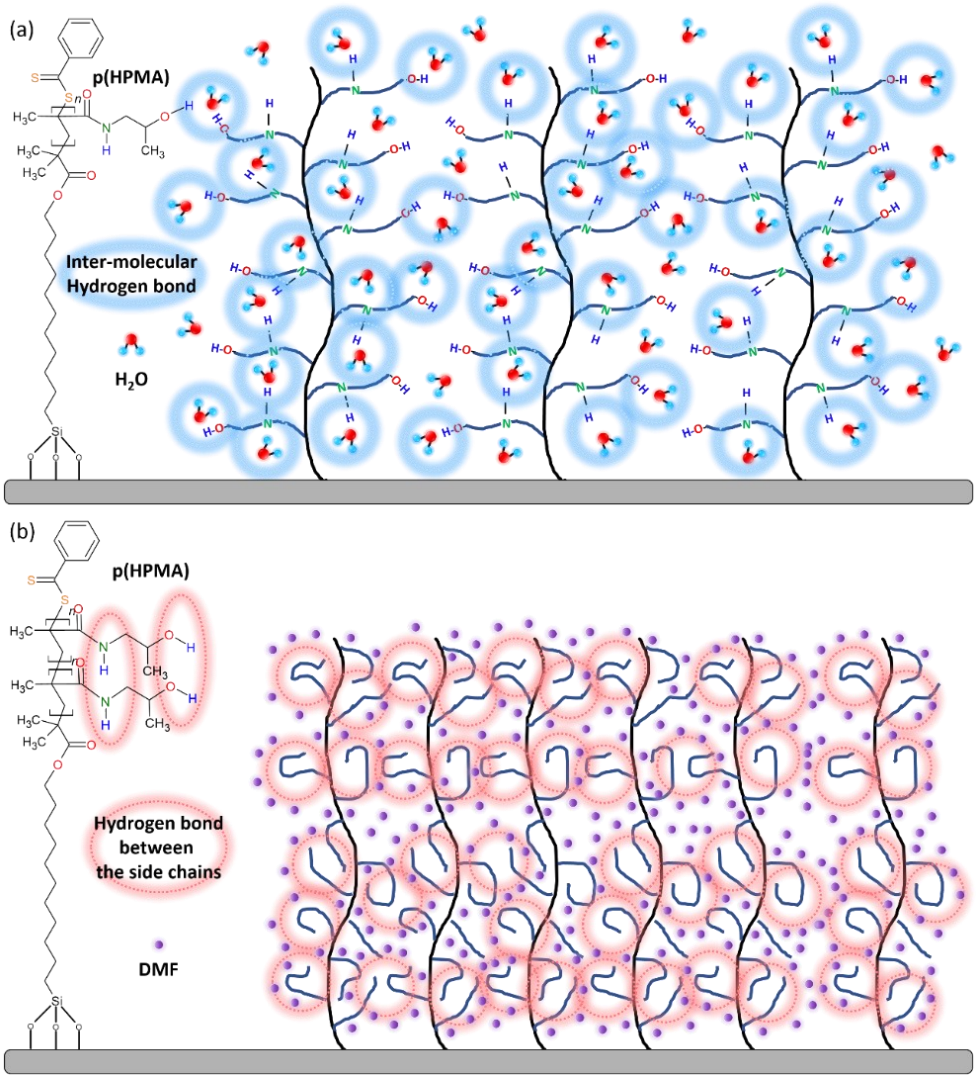

Scheme 13. Chemical structure of the grafted-from poly(HPMA) and illustration of inter- and intramolecular hydrogen bonding. (a) The inter-molecular hydrogen bonding between the water molecules and the side chains of the poly(HPMA). (b) The hydrogen bonding between the side chains of the poly(HPMA) in aprotic solvent.

4.2.2. Verification of solvent effects on kinetic relationship by 1,4-Dioxane/Water systems

To further investigate the solvent effects on the SI-RAFT of HPMA, we utilized mixtures of 1,4-dioxane and water at varying ratios (refer to Table 2, entries 5-7). Given that 1,4-dioxane is less polar than DMF, we anticipated a distinct effect of the solvent mixture composition on the grafting density. The conversion plot exhibited a near-linear pseudo-first-order kinetic (see Figure 20a). However, the molar mass reached a plateau after approximately 120 minutes for 1,4-dioxane 75% and 1,4-dioxane 50% (see Figure 20b), with slightly increased dispersity compared to the DMF/water systems (see Figure 20c). In comparison with the DMF/water system, we observed that the 1,4-dioxane/water system displayed an overall faster propagation rate but wider dispersity.

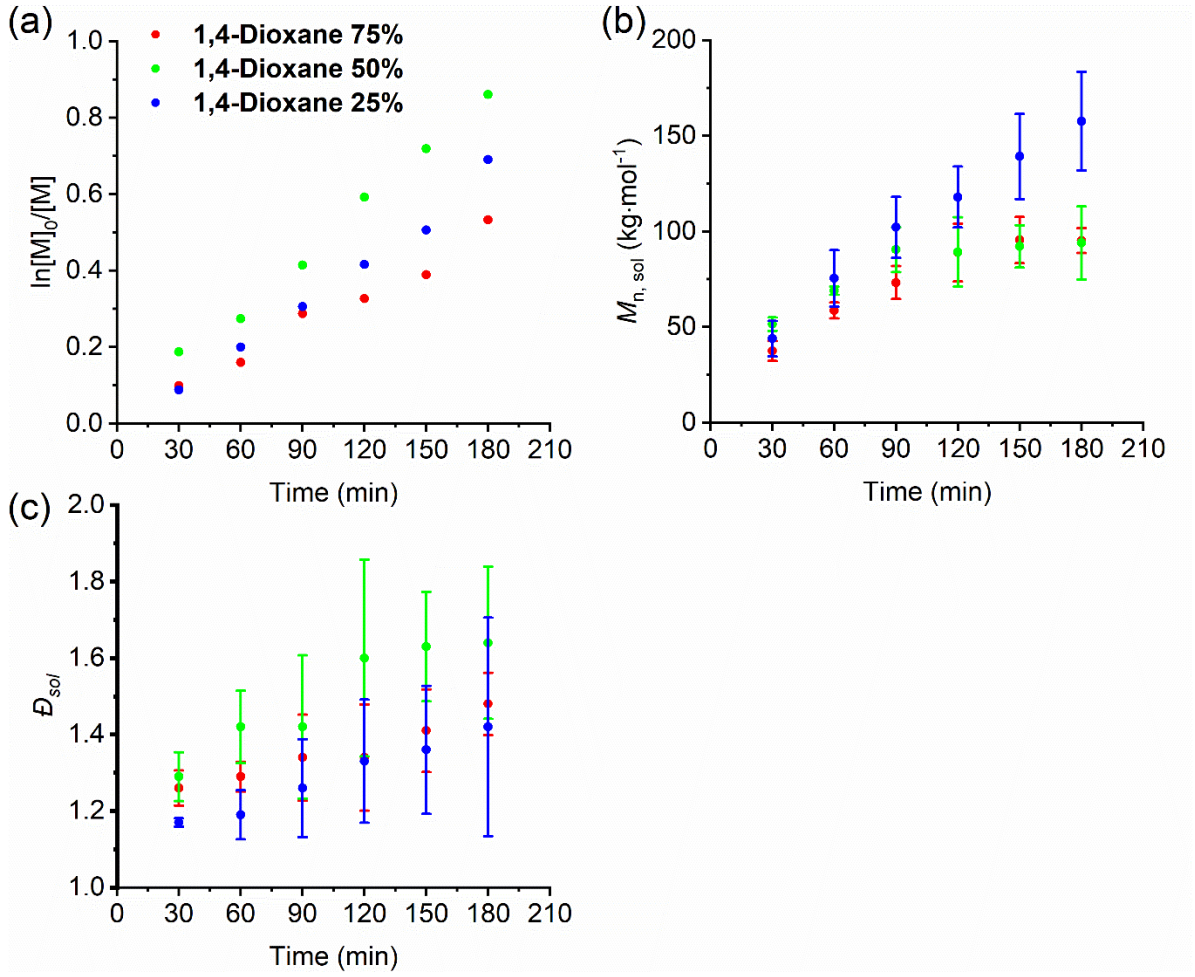

Figure 20. Kinetic plots of the solution-born poly(HPMA) via SI-RAFT polymerization in the 1,4-dioxane/water system: (a) conversion, (b) $M_{n,\ sol}$, and (c) dispersity against time.

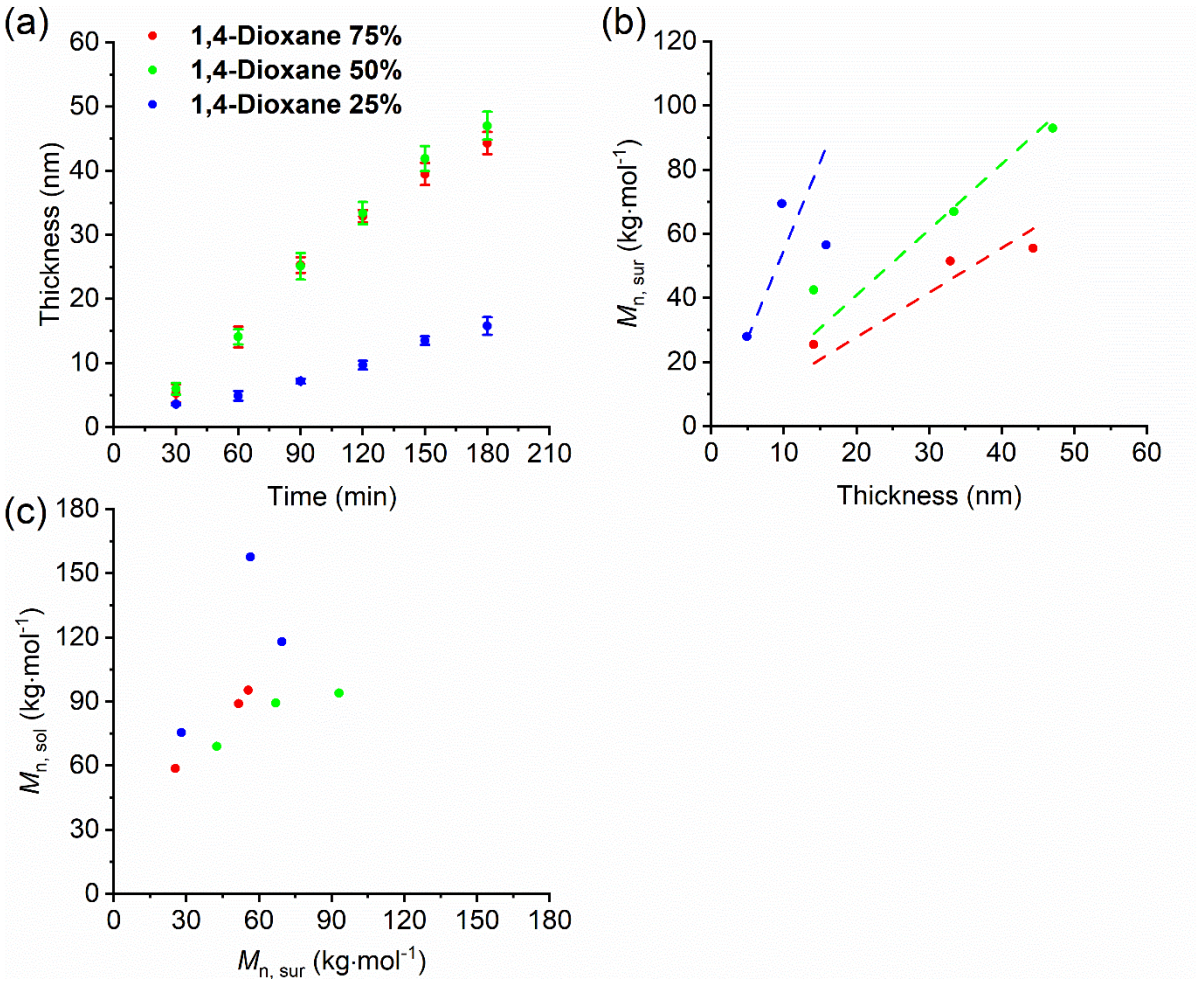

Figure 21. Kinetic plots of the grafted-from poly(HPMA) via SI-RAFT polymerization in the 1,4-dioxane/water system: (a) dry thickness against time, (b) $M_{n,\,sur}$ as a function of dry thickness (the dash lines represent the linear regression fits intercepting zero), and (c) the relation between $M_{n,\,sol}$ and $M_{n,\,sur}$.

Examining the thickness of the concomitantly formed polymer layers (see Figure 21a), we found that 1,4-dioxane 75% and 1,4-dioxane 50% reached higher thicknesses than those of DMF/water mixtures. Importantly, increasing the water content to 75% (1,4-dioxane 25%) led to a much lower thickness, comparable to DMF 25%. This aligns with observations in the DMF mixtures, but in the 1,4-dioxane/water system, the difference in thickness was even more pronounced. To assess the grafting density, we employed AFM-SMFS to determine $M_{n,\,sur}$. We also plotted $M_{n,\,sur}$ against the dry thickness and performed a linear regression fit using mass balance equation (see Section 3.3.1(5)) to obtain the grafting density of 1,4-dioxane/water systems. The

grafting density of the poly(HPMA) layer in 1,4-dioxane systems substantially decreased with increasing water content in the polymerization mixture, consistent with the results obtained for the DMF/water system (refer to Figure 21b), supporting our hypothesis.

Finally, we conducted comparisons between $M_{n,\,sol}$ and $M_{n,\,sur}$ under various conditions, commencing with the DMF/water system, and confirmed their discrepancy. While both $M_{n,\,sol}$ and $M_{n,\,sur}$ increased with higher water percentages, the absolute values depicted a widening gap (see Figure 18c). At the maximum water content (condition DMF 25%), the most significant difference between $M_{n,\,sol}$ and $M_{n,\,sur}$ became apparent in comparison to the other three conditions, with the $M_{n,\,sol}/M_{n,\,sur}$ ratio peaking at 2.4. Similarly, in ATRP polymerizations, the accelerated propagation rate emerged as a pivotal factor in the discrepancy between the M_n of the polymer obtained in solution versus on the surface. Solvent polarity and water content play pivotal roles in ATRP, altering the K_{ATRP} value. The escalated propagation noted in solution RAFT with increasing water content stemmed from the facilitated fragmentation of the RAFT adduct via hydrogen bonding with the solvent. Consequently, the mechanistic distinctions between ATRP and RAFT are crucial in understanding the solvent's effect and the observed variances in M_n between surface and solution. Our study's comparison empirically demonstrated that a higher propagation rate led to a greater discrepancy in molar masses between grafted-from and solution-born polymers. We theorized that the increased discrepancy between surface-grafted and solution-born polymers was induced by mass transfer limitations accompanying the higher solution propagation rate. The heightened viscosity due to increased conversion and $M_{n,\,sol}$ for the highest water content further retards diffusion to the surface, constraining surface propagation and causing it to lag behind propagation in solution. In the case of 1,4-dioxane/water systems, the most substantial difference between the molar masses of the polymer formed in solution and on the surface was also observed at the highest water content, i.e., condition 1,4-dioxane 25%, where the ratio reached 2.8 (see Figure 21c).

4.2.3. Summary

In summary, increasing the water content in the solvent accelerates the propagation rate of the solution, resulting in a greater difference between the molar masses of the polymer grown on the surface and in solution. Additionally, we observe that the solvent's proticity and polarity directly impact the achievable grafting density of poly(HPMA), a phenomenon elucidated through SMFS. This effect is likely due to reduced polymer-polymer interactions on the surface, causing the

surface chains to adopt a more extended conformation. Consequently, despite the faster propagation rate, the thickness of the poly(HPMA) layer decreases with higher solvent proticity and polarity. Therefore, to optimize the synthesis of poly(HPMA) brushes via SI-RAFT polymerization, it's advisable to use an aprotic solvent, ensuring a well-controlled CRP in the solution, potentially by adding a small amount of water. Notably, while high conversions are typically targeted in solution RAFT polymerization, the resulting increase in viscosity leads to mass transfer limitations in surface polymerization, creating disparities between solution and surface conditions. This study underscores the significance of solvent effects on SI-RAFT polymerization, which act through multiple mechanisms simultaneously, exerting a complex influence on polymer grafting. It's important to note that the solvent effects discussed herein are specific to the HPMA monomer and its SI-RAFT polymerization in aprotic and water-containing solvent mixtures. Further research on other monomers and SI-polymerizations could offer valuable insights into tuning molar mass and grafting density of surface-grafted polymers, particularly pertinent for coating applications such as biomaterials.

4.3. Density profile of surface-grafted polymer chains via SI-RAFT

4.3.1. Streaming current measurements of the GF-poly(HPMA) brush

Polymer brushes exhibit a distinct monomer density profile. [106] The analysis of the actual density profile of the monomer segments constituting the brush can be performed using various theoretical approximations (initially suggested by Alexander-de Gennes and further approached by Semenov-Milner-Witten) and experimental techniques, such as electrokinetics (EK) and neutron reflectometry (NR).

Alexander-de Gennes approximation assumes that the chains are uniformly stretched, with the free-ends of each chain at the top of the brush. [107] This is closely related to the thickness determined by spectroscopic ellipsometry according to a Cauchy-layer box-model. This assumes uniform refractive index and thickness, representing uniform extension of the bushes and an averaged segment distribution in the direction normal to the surface. In reality, the brushes show a gradually decreasing polymer segment density with increasing distance from the supporting surface. A more accurate solution was developed through the self-consistent field theory initially developed by Semenov and by Milner and Witten. The segment density profile is parabolic in the ideal case, i.e. in the case of monodisperse brush. The increase in dispersity of the surface confined polymer

chains leads to significant changes in the distribution profile. Namely, in cases of dispersity values $Đ > 1$, the segment distribution decreases more gradually in the outermost brush region, forming a pronounced tailing region (see Figure 22a).

The polymer brush segment density directly determines the penetration of the tangential flow of solution into the brush. The transport of mobile charges at the GF-poly(HPMA) solution interphase gives rise to the streaming current. The magnitude of the current highly depends on the hydrodynamic flow field and the distribution of mobile ions in the interfacial region between the polymer brush and the solution. Thus, the implementation of the segment distribution obtained through the self-consistent field theory into EK data can be utilized to test and verify the accuracy of the extracted density profile.

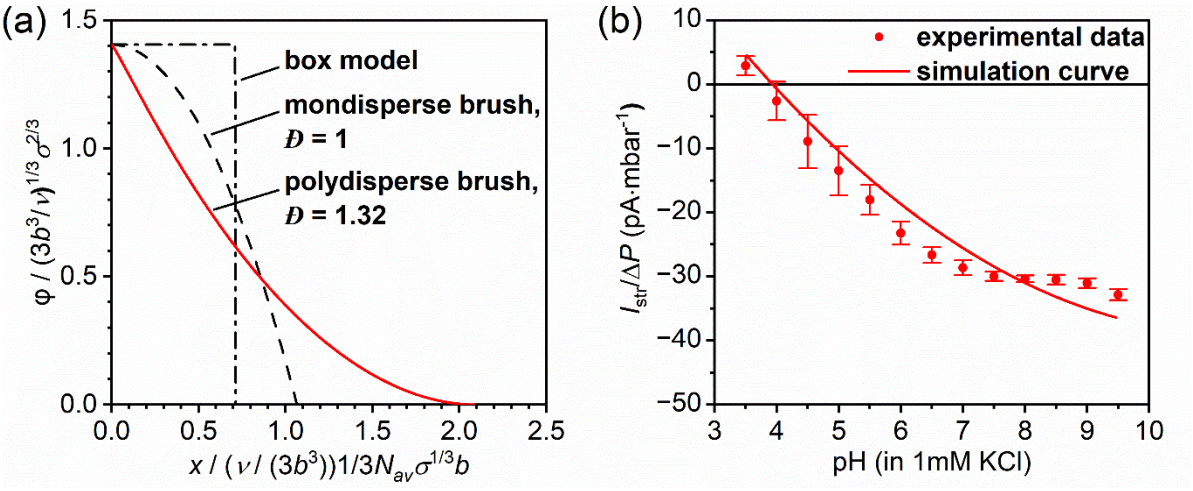

Figure 22. Summary of theoretical considerations and EK data. (a) Normalized segment density for monodisperse ($Đ = 1$) and disperse ($Đ = 1.32$) GF-poly(HPMA) brushes in rescaled units. The step-function at equal density and number average of monomer units is reported for comparison. (b) Measured streaming current over applied pressure, $I_{str}/\Delta P$, as a function of pH in 1 mM KCl solution for the 21.0 ± 0.7 nm thick GF-poly(HPMA) brushes. The solid line represents the obtained simulation results obtained by adjustment of the hydrodynamic penetration length in the brush, i.e. Brinkman length, $1/\lambda_o = 23.0$ nm and molecular parameters of the brushes obtained through combining the results from SE, SMFS-AFM and self-consistent theory. Parameters used: number average molar mass M_n = 42851 Da, dispersity $Đ = 1.32$, chain grafting density σ = 0.33 chains·nm^{-1}, average number of monomer units per polymer chain $N_{av} = 299$ monomer units, excluded volume parameter $\nu = 0.048$ nm^3, segment length b = 0.27 nm, channel length L_o = 20

mm, channel width, ℓ = 10 mm, channel height: H = 30 µm, viscosity of electrolyte solution η = 0.954 mPa·s^{-1} and relative dielectric permittivity of the solution: ε_r = 79.5.

Figure 22 b presents the streaming current data measured on GF-poly(HPMA) brushes in 1 mM KCl solution as function of the electrolyte pH. The brush films show a point of zero streaming current (PZSC) at pH of about 4.0, above which the layer is negatively charged. This is typical for interfacial charge formation by unsymmetrical water ion adsorption, which has been observed on various amphoteric surfaces. The degree of hydrodynamic screening depends on the extension of the brushes as compared to the extension of the diffuse layer (~9.7 nm in 1 mM KCl) and the segment density which determines the penetration of the tangential flow into the brush. The experimental data shown in Figure 22 b was reconstructed by implementing the theory of EK, assuming that the interfacial charge formation is not altered by the presence of the GF-poly(HPMA) brushes. The hydrodynamic penetration length, $1/\lambda_o$ = 23.0 nm, was fitted according to the least-squares method to recover the experimental data. As EK has been proven to be very sensitive in the analysis of the charge and structure of soft interfaces, the correlated evaluation of segment density distribution in the swollen GF-poly(HPMA) brushes enables the reliable determination of thickness of swollen brushes. Notably, this analysis also circumvents the main problems connected with *in situ* SE analysis for the determination of thickness of swollen films, i.e. strong correlation of thickness and optical parameters of the swollen layer, as well as the minor optical contrast between the swollen brush and the medium at measured wavelength range. [59, 90] The determined extension of the brushes upon swelling is 44 nm, i.e. the hydrodynamic flow field penetrates the brushes to less than 30% of their maximum extension in the direction normal to the supporting surface. Finally, the direct recovery of the EK experimental data by implementing the segment density profile obtained by self-consistent field theory, points to the attained polymer brush structure of the poly(HPMA) chains and the validity of the AFM-SMFS measurements.

4.3.2. Neutron reflectometry measurements of GF-poly(HPMA) brushes

Neutron reflectivity (NR) was measured on silicon discs coated with a GF-poly(HPMA) layer of 17.5 nm thickness, placed in a flow cell, which allowed to control the sample environment. Data were first collected in air and then the flow cell was filled with D_2O for subsequent collection. Additionally, NR was measured on bare Si discs to confirm the thickness and roughness of the native SiO_2 layer (data not shown). The obtained reflectivity curves were fitted to obtain the

corresponding scattering length density (SLD) profiles with multilayer models including interfacial roughness using refnx software (see Figure 23 a).

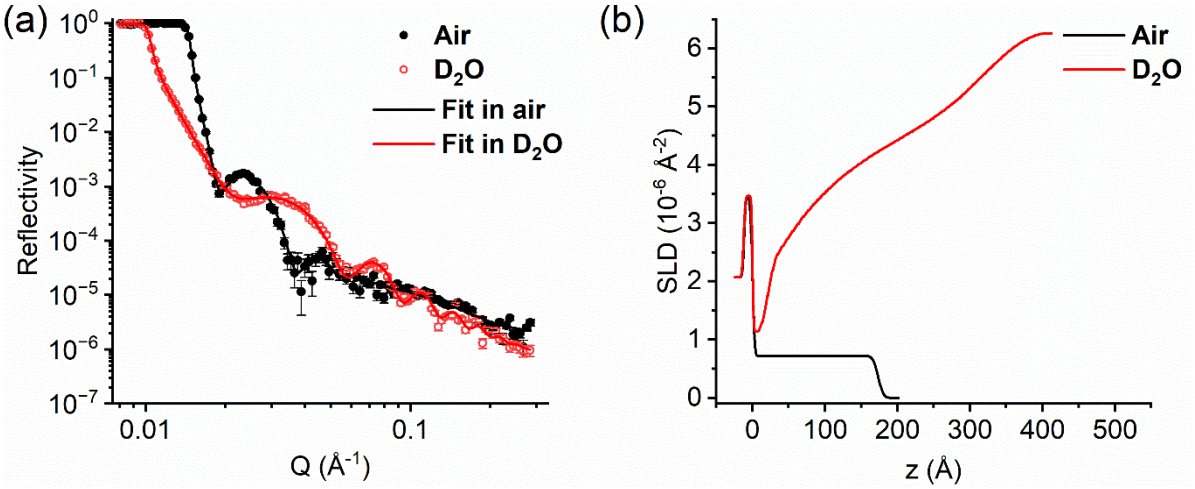

Figure 23. Summary of NR data analysis. a) NR curves of GF-poly(HPMA) coatings on Si discs in air and in D_2O. b) SLD profiles obtained for GF-poly(HPMA) in air and in D_2O from the fitting of the corresponding NR curves. *(Note: the measurement in air was performed under frontside incidence, while backside incidence was employed for the measurement in D_2O.)*

The models included the Si substrate (SLD_{Si} = 2.07·10^{-6} A^{-2}) and a native oxide layer ($SLD_{nat\ oxide}$ = 3.47·10^{-6} A^{-2}). The SLD profiles obtained from the fitting of the measured NR curves are shown in Figure 23 b. In the dry state, the NR curve displays clear Kiessig fringes and could be fitted with single slab of uniform SLD ($SLD_{poly(HPMA)}$ = 0.7223·10^{-6} A^{-2}) and thickness of 174 Å (17.4 nm), in excellent agreement with the preliminary measurement by spectroscopic ellipsometry of 175 Å (17.5 nm). For the GF-poly(HPMA) swollen in D_2O, the best fit was obtained with a model that included a slab to account for the polymer proximal layer/SAM of CTP and a spline component which accounts for the decaying volume fraction profile of the polymer layer, extending in total 408 Å (40.8 nm) beyond the native oxide layer. It can be seen that the SLD in swollen layer drops close to the substrate due to the presence of the dense organic layer and then increases, first rapidly and then gradually, to SLD_{D2O}. The obtained SLD profiles were used to calculate the polymer volume fraction profile φ as a function of the distance to the substrate z based on the equation:

$$SLD(z) = \varphi(z) \cdot SLD_{poly(HPMA)} + \big(1 - \varphi(z)\big) \cdot SLD_{solvent}$$

where $SLD_{solvent}$ is zero for the measurement in air and SLD_{D2O} for the measurement in D_2O.

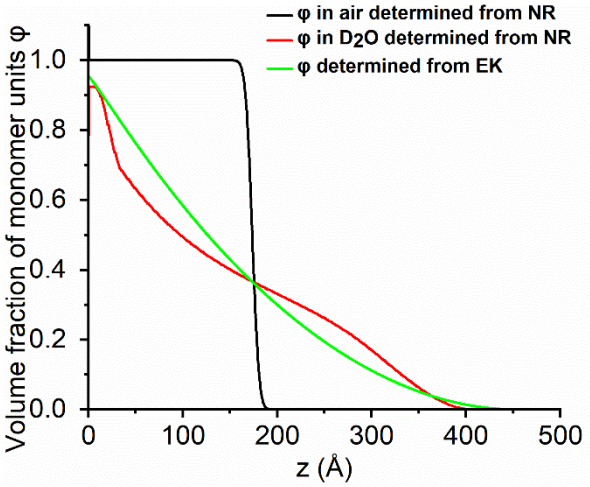

Figure 24. Comparison of the volume fraction profiles of GF-poly(HPMA) in air and in water as obtained from the NR analysis. The volume fraction profile of GF-poly(HPMA) brush obtained by EK is shown for comparison.

The obtained volume fraction profiles obtained by NR are shown in Figure 24. In the dry state, the polymer layer shows uniform density. In contrast, the layer shows clear swelling in the aqueous environment (D_2O), seen as a marked increase in the layer extent, due to uptake of solvent molecules within the layer. As previously noted, for a polymer brush consisting of monodisperse end-grafted chains, a parabolic volume fraction profile would be expected. The calculated volume fraction profile departs from this model as it displays two inflection points. Close to the substrate, a very high and rapidly dropping volume fraction is probably caused by the presence of the SAM, which bears the CTA groups enabling surface-initiated growth of polymer, as well as presumably a proximal layer of short polymer chains. Following the gradual drop, at large distance from the substrate the volume fraction decays slowly. This is probably a result of slight dispersity in the layer, allowing the longer chains to extend further than would correspond to a parabolic profile. The extracted NR and EK volume profiles do not completely match. This might arise from the differences in the layers performed in separate batches but might also be connected to the higher sensitivity of the EK analysis to the outer-swollen layer exposed to the tangential flow, while the NR is sensitive to the whole stack.

Integration of the volume fractions with respect to z yields the polymer interfacial volume. In air, this matches the thickness of the polymer layer of 174 Å (17.4 nm). In the swollen state, a

slightly lower interfacial volume of 140 Å (14.0 nm) is obtained from the NR data and 153 Å (15.3 nm). This discrepancy results from imperfections in the data modeling. Due to the lack of sharp features and measurement noise in the NR curves and intrinsic sensitivity mainly to the tailing region of the polymer brush layer, the utilized models for NR and EK data treatment may not account for all features of the layer precisely. Further analysis of the NR data should apply a fitting algorithm which can enforce the constraints of interfacial volume known *a priori*, as introduced by Gresham *et al.* [85, 108, 109] Finally, combining the AFM-SMFS, EK and NR data and further refining of the results will undoubtedly result is a more comprehensive understanding of the distinct polymer brush features of the surface-grafted chains obtained via grafting-from methods utilizing SI-RAFT.

4.4. Supplementary control of polymer coatings and their influence on biomaterials

4.4.1. The antifouling ability and hemocompatibility of polymer coatings with comparable repeat unit grafting to surfaces

In the preceding Section 4.1, we elucidated the pivotal role of the employed grafting technique in determining the antifouling ability of poly(HPMA) brushes to have a direct contract based on utilizing comparable molar mass. In this subsequent section, our focus shifts to employing various common candidates for antifouling coatings with comparable repeat units, aimed at evaluating their respective antifouling effectiveness. Furthermore, alongside their antifouling attributes, the blood compatibility of these coatings assumes significance for potential medical or clinical applications.

According to the enthalpic perspective, hydrophilic polymers are thermodynamically unfavored for protein adhesion to the surface. Consequently, we selected the hydrophilic polymers, poly(HPMA), poly(CBMAA), and PEO, which are commonly applied to resist the fouling from contacting with biological fluids. In this study, we grafted each of the selected polymers with a repeat unit of 50 on gold substrates via GT method (referred to as GT-poly(HPMA)$_{50}$, GT-poly(CBMAA)$_{50}$, and GT-PEO$_{50}$), individually, and acquired their corresponding physical and macromolecular parameters of polymer coatings (Table 3). Initially, we performed measurements of adsorption using SPR with polymer coatings and a pure gold substrate, utilizing undiluted HBP pooled from 5 donors. Our observations revealed varying degrees of fouling compared to the gold substrate (considered as 100% fouling). Specifically, GT-poly(HPMA)$_{50}$ exhibited 54%, GT-

poly(CBMAA)$_{50}$ exhibited 61%, and GT-PEO$_{50}$ exhibited 43% fouling individually (see detailed value of adsorbed mass at Figure 25). Notably, Section 4.1 (refer to Figure 16) presented the GF-poly(HPMA)$_{340}$ coatings with much higher fouling reduction which was attributed to much higher grafting density and larger molar mass by the perspective of increased entropic barrier effects.

Table 3. Physical and macromolecular parameters of selected polymer coatings with comparable number of repeat units.

Polymer	Repeat unit	M_n (kg·mol^{-1})	h_{dry} (nm)	σ (chain·nm^{-2})	Fouling (%)
GT-Poly(HPMA)$_{50}$	49	6619	2.1 ± 0.1	0.22 ± 0.02	54
GT-Poly(CBMAA)$_{50}$	56	12910	1.5 ± 0.2	0.08 ± 0.01	61
GT-PEO$_{50}$	45	2000	3.8 ± 0.2	1.25 ± 0.07	40

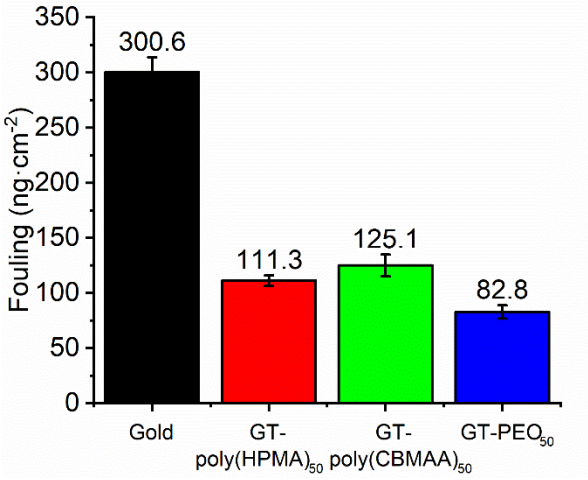

Figure 25. Non-specific protein adsorption of human blood plasma (HBP) with gold, GT-poly(HPMA)$_{50}$, GT-poly(CBMAA)$_{50}$, and GT-PEG$_{50}$. Kindly refer to Figure 16 for the fouling on GF- and GT- brushes of poly(HPMA)$_{340}$.

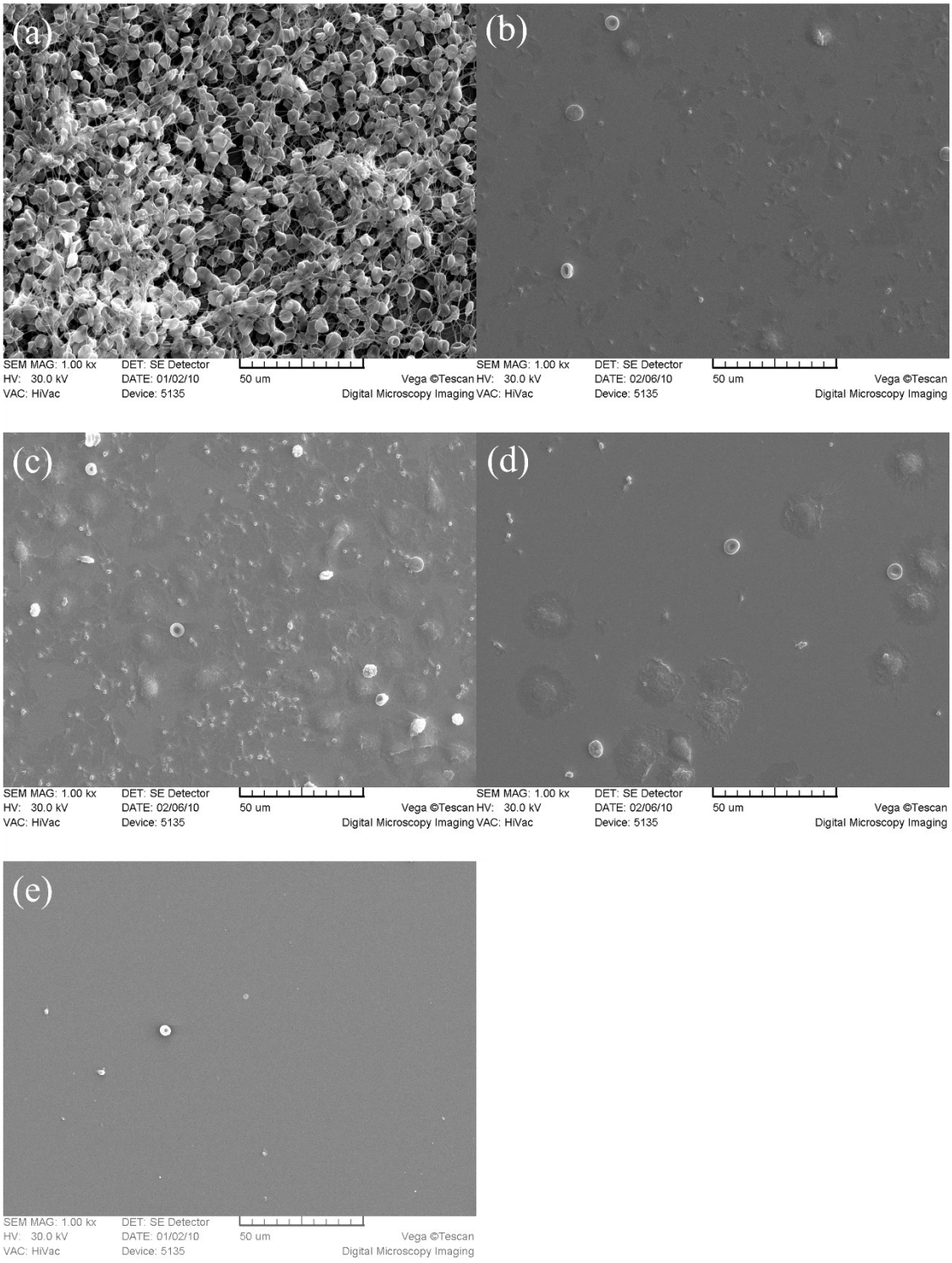

Figure 26. SEM image after 1h heparinized blood contact at 37°C under mild shaking: (a) glass substrate as reference, (b) GT-poly(HPMA)$_{50}$, (c) GT-poly(CBMAA)$_{50}$, (d) GT-PEG$_{50}$, and (e) GF-poly(HPMA)$_{340}$ coatings on glass substrates.

After referencing their fouling reduction to pure gold, these selected polymer coatings on glass underwent exposure to heparinized blood within a dynamic model designed to mimic the interaction of blood with a graft inserted into a patient's cardiovascular system. Heparin is commonly used as an anticoagulant during various surgical procedures such as those involving cardiopulmonary bypass or hemodialysis. The study analyzed the adherence of key cellular components (red blood cells, platelets, and leukocytes) to the surface, as well as the activation of the coagulation cascade leading to fibrin/thrombus formation with scanning electron microscopy (SEM). [110] Figure 26 illustrates the deposition observed on the samples following exposure to heparinized blood under dynamic conditions. Utilizing SEM, the adhesion of blood components (red blood cells, leukocytes, and platelets) was evaluated after a 1-hour incubation period. On glass surfaces, complete coverage was noted, forming a three-dimensional clot entrapping numerous leukocytes, platelets, and red blood cells, with a predominance of the latter. In contrast, the application of a polymer coating significantly mitigated cell adhesion, with significant reduction of leukocyte spreading and platelet adherence observed (see Figure 27). Notably, the poly(HPMA) brushes prepared by GF method following the previously elaborated procedures (Kindly refer to section 4.1.3.2, Table 1) showed superior performance due to the more pronounced polymer brush structure and higher entropic penalty exerted for the proteins to adsorb on the surface.

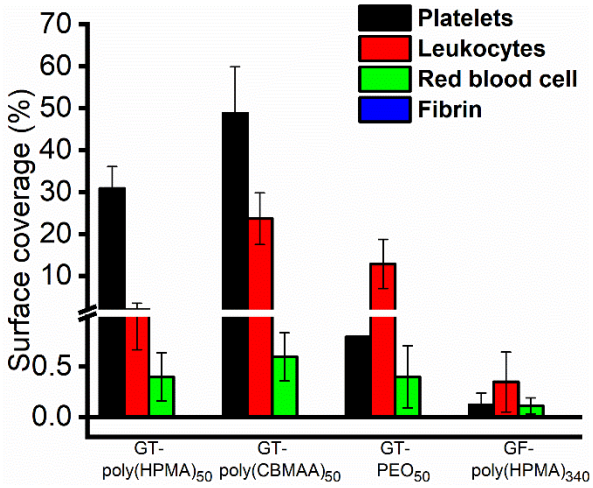

Figure 27. Imagine analysis by SEM with surface coverage of platelets (black), leukocytes (red), red blood cell (green), and fibrin (blue) on GT-poly(HPMA)$_{50}$, GT-poly(CBMAA)$_{50}$, GT-PEG$_{50}$, and GF-poly(HPMA)$_{340}$ coatings.

The adhesion of leukocytes and platelets holds significant importance in assessing the interaction between biomaterials and blood, as it influences the subsequent fate of the material. Platelet adhesion triggers activation and aggregation, initiating the coagulation cascade and thrombus formation, while leukocytes provoke an inflammatory response, leading to a foreign body reaction upon encountering foreign materials. The foreign body reaction is an inherent process occurring when any material is implanted within the body. Conversely, the presence of red blood cells in the deposited samples lacks informative value, as their primary biological function is oxygen transport, and their presence in deposits is primarily attributed to entrapment (e.g., within fibrin in thrombi) or inadequate washing procedures.

In general, the grafting of polymer coatings has been observed to minimize platelet and leukocyte adhesion while preventing thrombus formation. Preventing fouling from blood plasma presents an effective strategy for enhancing hemocompatibility. However, interaction with whole blood is highly intricate due to significant variability not only in the quantity but also in the composition of protein deposits, as well as potential conformational changes and enzymatic activity activation. In this context, protein identification emerges as a crucial element in comprehending these interactions toward the development of hemocompatible artificial surfaces. Part of this study targeted this, and the actual protein deposits have been analyzed to observe possible patterns of their appearance/presence in the adsorbed protein layers. For instance, the glass surface exhibited the highest protein adsorption, particularly proteins involved in the coagulation cascade. These proteins experienced significant reduction or elimination from fouling on alternative polymer coatings, thereby effectively preventing activation of the contact pathway. This study emphasized the significance of employing hydrophilic polymer coatings to mitigate the effects of fouling and underscored the importance of the hemocompatibility of chosen materials.

4.4.2. SI-RAFT polymerization of HPMA employing varying grafting site densities and its end group fidelity

The influence of grafting density on antifouling ability or hemocompatibility is often evaluated using the grafting-to (GT) method, typically incorporating comparable molar mass of the utilized polymers (for example, the GT method with GS and PS conditions detailed in Section 4.1). However, there is a paucity of direct inquiries utilizing the grafting-from (GF) method to explore the effect of grafting density on fouling reduction, largely due to the difficulties in measuring the

molar mass of surface-grafted polymers prepared by the GF method.

In the preceding section, we integrated our prior research to delve deeper into the experimentally validated variations in grafting densities of GF-poly(HPMA) and the fidelity of its CTA end group through the continuous construction of second block copolymers. This methodology enables a direct comparison of GF-poly(HPMA) across different grafting densities in this subsection. Moreover, the versatility of its block copolymer brushes extends their potential applications, particularly in biomaterial modification, enhancing their relevance and utility in diverse contexts.

Table 4. XPS surface composition of CTA-SAM layers at each dilution condition.

Peaks	**Br 3d5**	**Si 2p**	**C1s C-C**	**C1s C-O**	**C1s C=O**	**O1s**
	Atomic %					
Br-SAM	1.12	45.83	21.27	3.96	1.87	25.94
CTA-SAM 100%	0.20	44.40	24.73	3.17	1.98	25.53
CTA-SAM 10%	0.22	44.97	24.09	3.28	1.97	25.47
CTA-SAM 1%	0.32	45.47	22.94	3.28	1.87	26.12
CTA-SAM 0.1%	1.12	45.26	21.69	4.01	2.05	25.88
CTA-SAM 0.01%	1.14	45.48	21.52	4.01	2.02	25.83
CTA-SAM 0.001%	1.12	45.59	21.62	3.98	1.83	25.85

To achieve a dilution series of grafting sites and control the density of CTA, the stock solution prepared in the previous step was diluted with pure DMSO. This dilution series was carried out in the range of 100% to 0.01%. Br-SAM was then placed within the range of 100% to 0.01% dilution solution and subjected to the same conditions to obtain various degrees of CTA immobilization coverage on the substrates. Confirmation of the successful immobilization of the CTA group was obtained through XPS analysis. In the XPS spectrum of the Br-SAM surface, the C 1s region reveals contributions from C-C and C-H (285.0 eV), C-O and C-Br (286.6 eV), O-C=O (289.3 eV), and distinctive C-Br features in the Br 3d region (spin–split Br $3d_{5/2}$–Br $3d_{3/2}$ doublet components

centered at 70.3 eV and 71.3 eV, respectively). In Table 4, it was noted that the Br 3d5 signal decreased to 0.2 atomic % when compared to Br-SAM at 100% concentration of the stock solution for original CTA-SAM preparation (referred to as CTA-SAM 100%). Upon diluting the stock solution to 0.001%, the Br 3d5 signal remained consistent with that of Br-SAM. Additionally, a noteworthy disparity in the atomic % of Br 3d5 was observed between CTA-SAM 1% (0.32 atomic %) and CTA-SAM 0.1% (1.12 atomic %).

Table 5. Physical and macromolecular parameters of GF-poly(HPMA) layers synthesized via SI-RAFT polymerization in DMF 100% condition at 2h with varying grafting density of CTA-SAM.

Sample	$M_{n,\,sol}$ **(kg·mol^{-1})**	$Đ$	$M_{n,\,sur}$[a] **(kg·mol^{-1})**	h_{dry} **(nm)**	σ[a] **(chain·nm^{-2})**
Br-SAM	44.5	1.34		1.8[b]	NA
CTA-SAM 100%	44.5	1.34		22.5	0.56
CTA-SAM 10%	46.0	1.31		22.1	0.55
CTA-SAM 1%	42.5	1.38	26.5	21.3	0.55
CTA-SAM 0.1%	4.50	1.34		3.5	0.09
CTA-SAM 0.01%	42.0	1.43		2.3	0.06
CTA-SAM 0.001%	43.0	1.36		2.4	0.06

[a] the $M_{n,\,sur}$ was obtained from Section 4.2 since it's under the same condition.

[b] the thickness of Br-SAM was its original thickness of the monolayer.

To delve deeper into controlling the variability in grafting density at the grafting sites, we conducted SI-RAFT polymerization of HPMA under the conditions outlined in Section 4.2, utilizing 100% DMF as per the specified conditions, to investigate its impact on polymer dry thickness and the fidelity of its CTA end group. In this study, we obtained both the molar mass of solution-born polymer and the dry thickness of grafted-from polymer, as detailed in Table 5. Consistent with the XPS results indicating a lower CTA immobilization rate, we observed minimal growth in the thickness of poly(HPMA) at CTA-SAM 0.1%. This suggests a successful reduction

in grafting site density, resulting in a thinner grafted-from poly(HPMA). To further discern the critical concentration of the atom-transfer radical addition process, we proceeded to investigate varying grafting densities between CTA-SAM 1% and CTA-SAM 0.1%.

Table 6 showcases additional experimental trials wherein we introduced diverse dilutions to achieve varied grafting densities and observe their resultant polymer thickness. In line with our hypothesis, we pinpointed the critical concentration range of the stock solution to lie between 0.8% and 0.2%, resulting in a reduction in both polymer thickness and the corresponding grafting density of the polymer. This study significantly highlights the potential to manipulate the initial quantity of grafting sites and regulate the final grafting density of polymer coatings. While higher grafting density is advantageous for antifouling ability due to increased conformational freedom of the polymer structure on the surface, it is also crucial to attain sufficient modification to minimize chemical wastage. Moreover, establishing a comprehensive database of polymer coatings with varying grafting densities is essential to cater to different application requirements effectively. Having preserved the Br-initiating groups, the method can be utilized for the subsequent synthesis of other functional polymers from the bottom of the brush via ATRP.

Table 6. Physical and macromolecular parameters of GF-poly(HPMA) layers synthesized via SI-RAFT polymerization in DMF 100% condition at 2h with varying grafting density of CTA-SAM.

Sample	$M_{n,\,sol}$ (kg·mol^{-1})	$Đ$	$M_{n,\,sur}$[a] (kg·mol^{-1})	h_{dry} (nm)	σ[a] (chain·nm^{-2})
CTA-SAM 1%	46.5	1.33	26.5	19.3	0.48
CTA-SAM 0.8%	43.0	1.35		19.3	0.48
CTA-SAM 0.6%	46.5	1.34		15.2	0.38
CTA-SAM 0.4%	44.0	1.41		15.7	0.39
CTA-SAM 0.2%	44.5	1.41		4.7	0.12
CTA-SAM 0.1%	45.0	1.42		2.3	0.06

[a] the $M_{n,\,sur}$ was obtained from Section 4.2 since it's under the same condition.

To enhance the adaptability of poly(HPMA) coatings, we designed a hierarchical structure incorporating poly(HPMA) and poly(HEMA) arranged in varying sequences to further prove that the integrity of the CTA end groups is preserved. Thus, these experiments go beyond the XPS analyses reported in Subsection 4.1.3.1., Figure 13 showing the preservation of the CTA distal-chain-end group and directly proves their ability to undergo subsequent polymerizations or specific reactions.

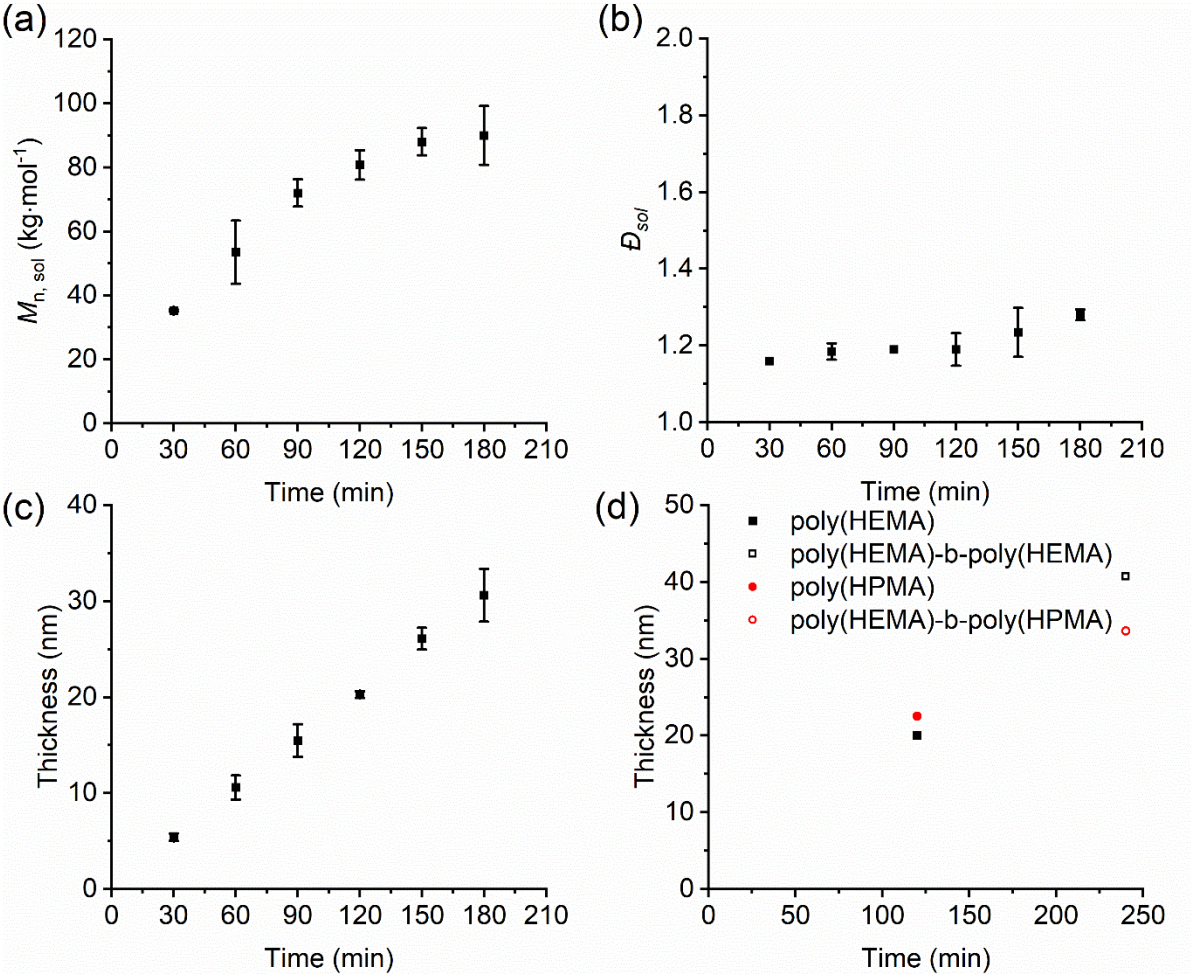

Figure 28. Kinetic plots of the GF-poly(HEMA) via SI-RAFT polymerization in the DMF 100% condition: (a) $M_{n,\,sol}$, (b) dispersity, and (c) thickness against time. Extension experiment: (d) SI-RAFT polymerization of HEMA on macro-CTA-SAM of poly(HEMA) (black solid square) and poly(HPMA) (red solid circle) and their diblock copolymer as poly(HEMA)-*b*-poly(HEMA) (black open square) and poly(HPMA)-*b*-poly(HEMA) (red open circle).

Initially, we carried out SI-RAFT polymerization of HEMA from a silicon substrate in DMF under 100% conditions, varying the reaction time, and plotted the kinetics, as depicted in Figure 28. Poly(HPMA) coating was synthesized under the same conditions outlined in Section 4.2. To further probe its CTA end group integrity, we applied each sample, with a thickness of 20 nm, to construct a second block of poly(HEMA) as poly(HEMA)-*b*-poly(HEMA) and poly(HPMA)-*b*-poly(HEMA). We employed SI-RAFT polymerization of HEMA in DMF under 100% conditions for 2 hours to anticipate a second block of 20 nm of poly(HEMA). Poly(HEMA)-*b*-poly(HEMA) exhibited continuous growth of poly(HEMA) with an additional thickness of 20.7 nm, indicating fidelity of the CTA end groups after the initial SI-RAFT polymerization (see Figure 28d). However, poly(HPMA)-*b*-(HEMA) demonstrated less growth of poly(HEMA) with an additional thickness of 11.1 nm. We hypothesize that this discrepancy may be attributed to either partial loss of CTA end groups after the initial SI-RAFT polymerization or inference from the methacrylamide group of HPMA. Nevertheless, this study showed the potential of building hierarchical structure of polymer brushes via SI-RAFT polymerization, showcasing its capability to use second blocks of other reactive monomers bearing azide, propargyl, glycidyl, etc. to be further utilized for the conjugation of bio-markers for use as a bioactive and biosensing platforms.

Peptide nucleic acids (PNAs) have emerged as versatile molecules in biosensing platforms due to their unique properties. PNAs are synthetic ribonucleic acid analogs composed of a peptide backbone to which nucleobases are attached. They emulate the structure of micro-RNAs, short noncoding ribonucleic acids that have been linked with a multitude of human diseases including lung, breast, and hematological cancers. Unlike, the RNAs which have ribose-phosphate backbone, the peptide backbone of PNAs provides remarkable stability, resistance to enzymatic degradation, and high binding affinity to complementary nucleic acid sequences. These attributes make PNAs ideal candidates for various biosensing applications, including nucleic acid detection, gene expression analysis, and diagnostic assays. By exploiting the specific binding capability of PNAs to target nucleic acid sequences, biosensing platforms can achieve high sensitivity, specificity, and versatility in detecting a wide range of diseases connected to micro-RNA either secreted in the blood or present in various compartments of the cell membrane. Additionally, PNAs can be easily functionalized with various labels or probes, enabling the development of diverse detection strategies for biomolecular analysis. As such, the integration of PNAs into biosensing platforms holds great promise for advancing the field of molecular diagnostics and biomedical research. It

was found that miR-125b plays a crucial role in the regulation of tumorigenesis, various cancers and myelodysplastic syndromes. [111, 112] Thus, PNAs can be potentially used in the diagnosis, prognosis and clinical treatment of tumors, cancers and various rare blood diseases.

Table 7. XPS analysis of cPNA-125b conjugated with poly(HEMA)-SH at different concentrations for thiol-yne click reaction.

Peaks		**Si 2p**	**C 1s C-C**	**C 1s C-C=O**	**C 1s C-O**	**C 1s C=O**	**N 1s**	**O 1s**
		Atomic %						
Poly(HEMA)-SH		2.8	22.5	11.3	22.6	9.8	0	31.1
cPNA$_{11}$-125b	0.01 mg·mL^{-1}	5.6	19.2	11.1	22.2	9.6	2.0	30.4
	0.1 mg·mL^{-1}	5.7	19.4	11.1	22.2	9.5	2.1	30.1
	1 mg·mL^{-1}	4.6	18.9	12.0	23.9	9.0	2.2	29.4
cPNA$_{22}$-125b	0.01 mg·mL^{-1}	5.0	19.0	11.2	22.5	9.8	1.6	30.9
	0.1 mg·mL^{-1}	4.3	19.2	11.5	23.1	9.6	1.3	31.0
	1 mg·mL^{-1}	3.2	19.3	11.9	23.9	9.5	1.3	31.0

As a result of our efforts, we introduced modifications to the complementary PNA stemming from the structure of miR-125b emulating a specific upregulated blood circulating marker of myelodysplastic syndromes (cPNA-125) by incorporating an alkyne group. This facilitated their conjugation with the poly(HEMA)-SH polymer coating by exposing the substrates under UV irradiation for a short time in the presence of the cPNA-125 solutions, often referred as thiol-yne click. We tested cPNA-125 comprising of 22 and 11 peptide nucleic acid units (sequences of TCAC AAG TTA GGG TCT CAG GGA and GG TCT CAG GGA, respcetively). Through XPS analysis, we were able to detect the N 1s signal (as shown in Table 7), providing conclusive evidence of the successful conjugation between the poly(HEMA)-SH coating and cPNA-125. This achievement marks a significant milestone in the development of PNAs-based biosensing platforms, particularly in the realm of clinical applications. However, it's worth noting that while this study

yielded promising results, it remains ongoing, with its progress limited by the constraints of the PhD program timeframe.

4.5. Biocompatible scaffold prepared through DLP incorporating PET-RAFT polymerization

Hydrogels, cryogels and hybrid biomaterials are highly promising in the realm of biomedical engineering due to their versatile advantages. These materials can amalgamate diverse components such as polymers, ceramics, or metals to achieve superior mechanical properties and tailored biocompatibility. By leveraging the strengths of different materials, hybrid biomaterials offer improved mechanical strength, flexibility, and compatibility, crucial for applications like orthopedic implants and tissue engineering scaffolds. Furthermore, their flexibility in design and manufacturing facilitates customized adjustments to meet specific biomedical needs, ensuring optimal performance across a spectrum of applications.

Some proof-of-concept studies have been performed to visualize tailorable polymeric scaffold as potential hybrid biomaterials. The incorporation of diacrylate polyethylene glycol (DAPEG) and HPMA using photoinduced electron transfer reversible addition fragmentation chain transfer (PET-RAFT) polymerization represents a method to create a "living" biomaterial, which has significant applications in various fields, including biomedicine and materials science with tailored properties. [82, 113, 114] The integration of macromolecular chemistry with printing technology represents a significant advancement in the field of biomaterial fabrication. The presence of CTA within a polymeric scaffold introduces the possibility of self-healing properties, while the addition of selected growth factors post-polymerization holds promise for inducing regeneration along the scaffold.

Table 8. The gelation time of varying feeding ratio of VAT solution performed under FRP and RAFT polymerization. (*Kindly note, that the table is reported here, and not in Material section for better referencing and guidance through obtained results)*

Feeding ratio of VAT solution				**Designation**	**Gelation Time (s)**
DAPEG	HPMA	CTA	TPO-L		
300	100	0	25	FRP-300:100	1.5
200	200	0	25	FRP-200:200	3.0
100	300	0	25	FRP-100:300	11.0
300	100	1	25	RAFT-300:100	3.5
200	200	1	25	RAFT -200:200	7.0
100	300	1	25	RAFT -100:300	17.0

Our preliminary investigation focused on evaluating the printability of specific materials, namely DAPEG as a crosslinker and HPMA as inbuilt non-fouling polymer segment, through the change between their storage modulus and loss modulus using a photo-rheometer (Table 8). Through the measurement of photo rheometer, we sought to elucidate the rheological behavior of the materials during the printing process. Upon analysis, we discerned a notable effect upon the addition of a CTA, which manifested in an extended gelation time. This temporal extension was particularly evident at the point of intersection between the storage and loss moduli, indicative of the gelation process (see Figure 29). This observation underscores the intricate kinetics underlying the RAFT polymerization mechanism. The heightened gelation time can be attributed to the modulating effect exerted by the CTA on the polymerization kinetics, altering the propagation and chain termination rates, thereby influencing the gelation dynamics.

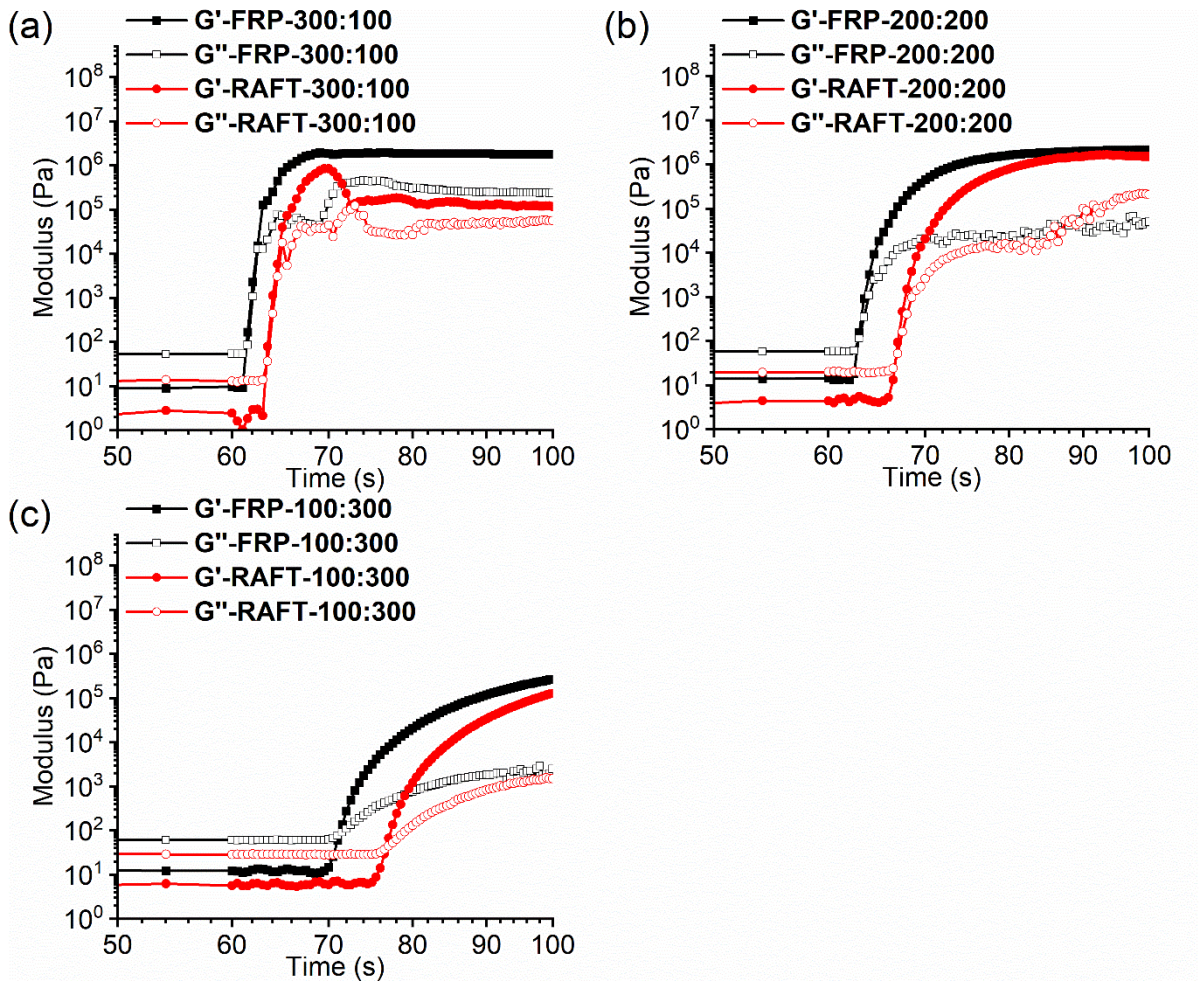

Figure 29. Representative curves of storage modulus and loss modulus between FRP and RAFT polymerization with the same feeding ratio. The light exposure started at 60 s.

We conducted characterization of the printed hydrogel utilizing FTIR techniques to validate their chemical composition. As illustrated in Figure 30, we effectively observed heightened absorbance peaks corresponding to the amide I and amide II bands at 1635 and 1525 cm^{-1}, respectively, indicative of the presence of the methacrylamide group inherent in HPMA, alongside increased absorbance signals attributed to characteristic functional groups from PEG within both FRP and RAFT polymerized hydrogels.

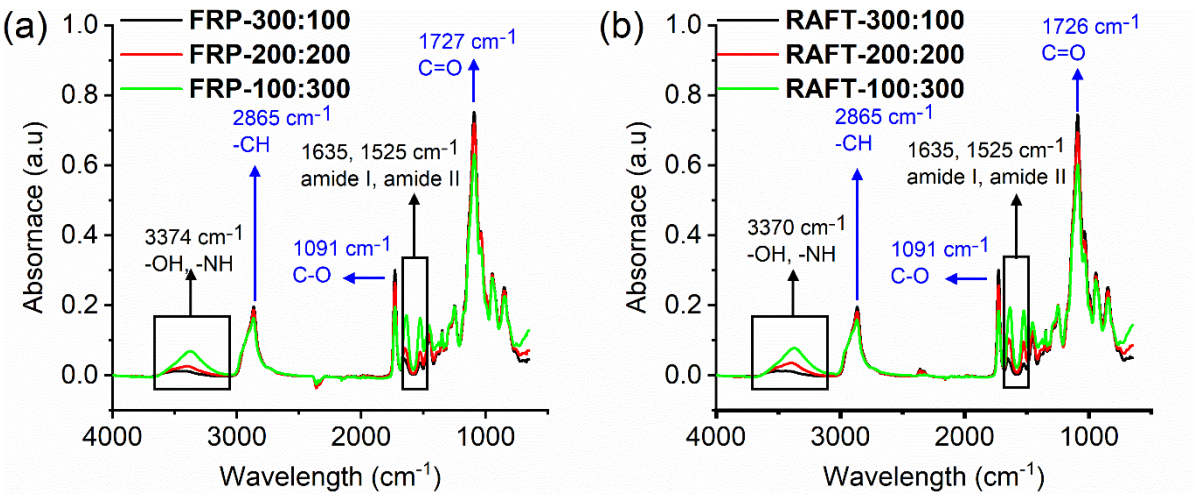

Figure 30. FTIR spectra of poly(HPMA)-*co*-PEG hydrogel prepared by DLP. Coding what does it mean.

Subsequently, each sample exposed to the leaching solution for varying durations underwent normalization against a tissue culture plate (TCP) used as a positive control, devoid of any leaching solution. Metabolic activity assessment was conducted one day later, and the outcomes are presented in Figure 31. Remarkably, the results demonstrate a highly favorable biocompatibility, particularly noteworthy is the comparable viability observed in the RAFT hydrogel, akin to that of the TCP.

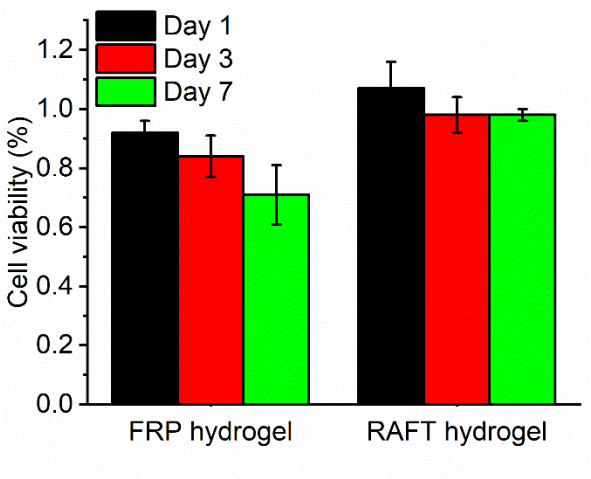

Figure 31. MTS assay of fibroblasts on DLP printed hydrogel via RAFT polymerization and FRP related to TCP.

Ultimately, leveraging the optimized printing parameters and VAT solution, we crafted a computer-aided design (CAD) featuring the logos of PBM UGent and IMC. The refined conditions facilitated precise integration of CAD and computer-aided manufacturing (CAM), achieving an impressive integration rate of 99.7% for the IMC logo and 97.9% for the PBM UGent logo, as illustrated in Figure 32).

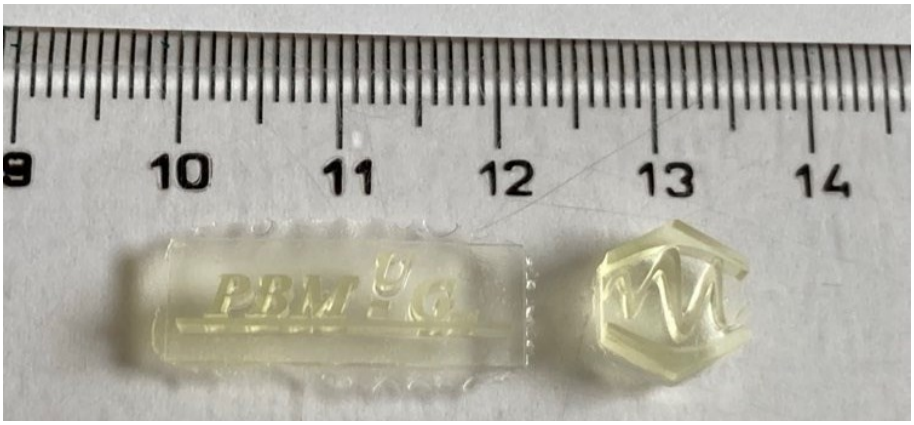

Figure 32. Printed poly(HPMA)-*co*-PEG hydrogel logo of PBM UGent and IMC by DLP.

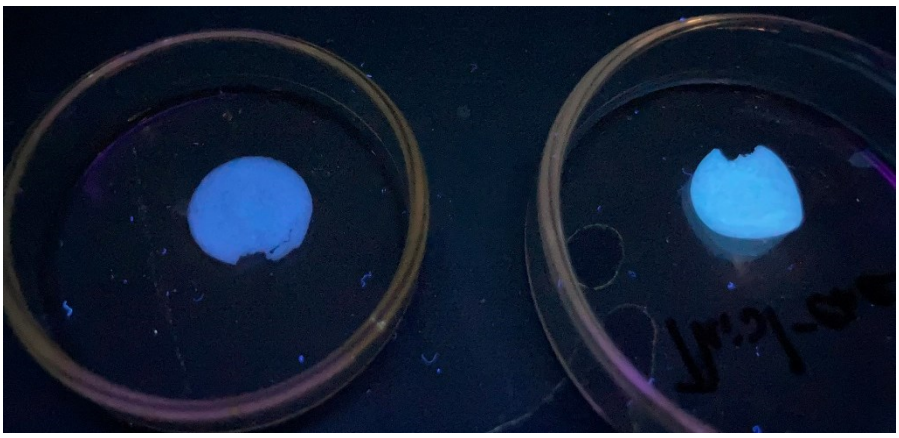

Figure 33. Comparison of post-polymerization thiol-ene click reactions in printed hydrogels with quinine. The hydrogel on the left serves as the reference, having undergone no aminolysis, while the one on the right underwent aminolysis. This photo depicts the hydrogels after the click reaction and exposure to a 6-Watt UV lamp emitting light at 365 nm.

The inclusion of RAFT polymerization offers a significant advantage due to its capability for post-polymerization modifications, thereby enhancing the versatility of hydrogel synthesis. In Figure 33, our observations indicate a notable contrast: only the hydrogel that underwent

aminolysis exhibited successful click reactions with quinine, evident through the manifestation of fluorescence. This outcome highlights the importance of post-polymerization strategies facilitated by RAFT polymerization in tailoring hydrogel properties for specific applications.

In addition to the thiol-ene click post-polymerization, we conducted a chain growth post-polymerization using *N*-(2,2-difluoroethyl) methacrylamide (DFEA), recognized as an MRI imaging agent. In Figure 34, we achieved successful acquisition of the F^{19} MRI image, confirming the incorporation of DFEA into the hydrogel through post-polymerization. These findings underscore the versatility enabled by integrating RAFT polymerization into 3D printing, offering various post-polymerization approaches such as thiol-ene click reactions or chain growth polymerization.

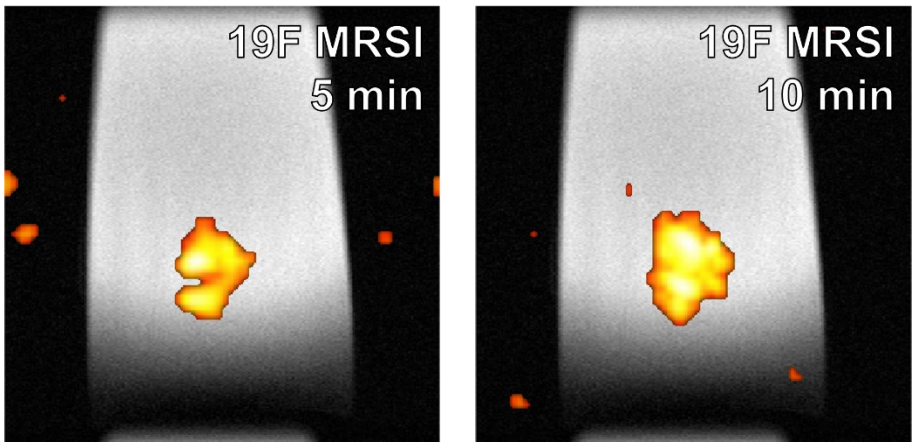

Figure 34. The MRI imagine of hydrogel containing DFEA after post-polymerization.

In our pursuit of further advancements in the field, we contemplated synthesizing composite materials through the integration of DLP PET-RAFT polymerization and surface modifications of ZnO nanocolumns (ZnO NC) with various doping. [115, 116] Notably, ZnO NC, transparent and employed as light-guiding materials, were anticipated to seamlessly integrate without compromising the DLP process. The envisioned incorporation of ZnO NC aimed not only to maintain the biocompatibility of poly(HPMA)-based scaffolds but also to introduce antibacterial properties and potentially enhance the metabolic activity of fibroblasts and endothelial cells. [117-121] The possibility of doping ZnO NC with molybdenum was considered as a means to target the immunometabolism and mitochondrial function of macrophages. [122]

Initially, we embarked on two simultaneous research projects focused on ZnO NC and DLP printing, intending to merge them into a third project to produce the ultimate hybrid biomaterials. However, due to time limitations, only the results concerning ZnO NC were published, while the remaining projects could not be completed.

5. Conclusions

Throughout the course of this thesis, an extensive array of methodologies and investigations into the realm of polymer brushes and biomaterials has been elaborately detailed. Specifically, the utilization of reversible addition-fragmentation chain transfer (RAFT) polymerization has been elucidated to offer profound and adaptable impacts when integrated into surface coating and three-dimensional (3D) printing processes. The employment of RAFT polymerization has facilitated the precise manipulation of both the physical and macromolecular properties inherent to surface coatings, achieved through the nuanced adjustment of grafting methodologies and careful consideration of solvent effects during surface-initiated (SI)-RAFT polymerization. This exhaustive inquiry has culminated in the establishment of a comprehensive set of fundamental principles, poised to not only augment surface coating techniques but also to offer promising applications within the realm of soft material research, biomedicine, and applications in which the enhancement of antifouling capabilities is of primary interest. Furthermore, the inherent tailoring characteristic of RAFT polymerization has unveiled a myriad of avenues for further modifications, thereby significantly broadening the spectrum of potential applications across diverse domains.

Besides, this thesis has introduced several innovative and unique techniques for the characterization of polymer brushes synthesized via grafting-from method, including atomic force microscopy-based single molecule force spectroscopy (AFM-SMFS), electrokinetic (EK), and neutron reflectometry (NR). The incorporation of AFM-SMFS has effectively surmounted the challenges associated with the retrieval of de-grafted polymer chains from surfaces, facilitating the determination of molar mass and dispersity. The dissemination of findings within this thesis has also advocated for the widespread adoption and popularization of AFM-SMFS as a novel characterization method. Moreover, the amalgamation of AFM-SMFS, EKP, and NR holds promise in enriching our comprehension of the distinctive attributes of polymer brushes. This lays the groundwork for the comparison and demonstration of density profiles and volume fractions for poly(HPMA) coatings measured by both techniques for the first time.

Moreover, following an in-depth exploration of polymer brushes, the fabrication of biomaterials incorporating RAFT polymerization and digital light processing (DLP) 3D printing in the context of hydrogel scaffolds adorned with antifouling polymers has been delineated within this thesis. The amalgamation of RAFT polymerization and DLP 3D printing prompted the inclusion of an

additional chapter in this thesis. This chapter successfully elucidates the printability of the selected methods and materials, underscoring precise control over the printed objects with high biocompatibility. These findings position the synthesized materials as compelling candidates for biomedical applications.

6. References

(1) Ricordon, J.; Sovij, D.; Sanner, S.; Sinton, D.; Young, E. W. K. Deep Learning with Microfluidics for Biotechnology. *Trends Biotechnol.* **2019**, *37*, 310-324.

(2) Bixler, G. D.; Bhushan, B. Biofouling: lessons from nature. *Phil. Trans. R. Soc. A* **2012**, *370*, 2381–2417.

(3) Wu, J.; Chen, J.; Liu, K.; Luo, S. Engineering Antifouling Conducting Polymers for Modern Biomedical Applications. *ACS Appl. Mater. Interfaces* **2019**, *11*, 21294-21307.

(4) Holmlin, R. E.; Chen, X.; Champman, R. G.; Takayam, S.; Whitesides, G. M. Zwitterionic SAMs that Resist Nonspecific Adsorption of Protein from Aqueous Buffer. *Langmuir* **2001**, *17*, 2841-2850.

(5) Sigal, G. B.; Mrksich, M.; Whitesides, G. M. Effect of Surface Wettability on the Adsorption of Proteins and Detergents. *J. Am. Chem. Soc.* **1998**, *120*, 3464-3473.

(6) Prime, K. L.; Whitesides, G. M. Adsorption of proteins onto surfaces containing end-attached oligo(ethylene oxide): a model system using self-assembled monolayers. *J. Am. Chem. Soc.* **1993**, *115*, 10714-10721.

(7) Emmenegger, C. R.; Brynda, E.; Riedel, T.; Sedlakova, Z.; Houska, M.; Alles, A. B. Interaction of Blood Plasma with Antifouling Surfaces. *Langmuir* **2009**, *25*, 6328-6333.

(8) Vorobii, M.; de los Santos Pereira, A.; Ognen Pop-Georgievski, O.; Kostina, N. Y.; Rodriguez-Emmenegger, C.; Percec, V. Synthesis of non-fouling poly[N-(2-hydroxypropyl)methacrylamide] brushes by photoinduced SET-LRP. *Polym. Chem.* **2015**, *6*, 4210-4220.

(9) de los Santos Pereira, A.; Sheikh, S.; Blaszykowski, C.; Pop-Georgievski, O.; Fedorov, K.; Thompson, M.; Rodriguez-Emmenegger, C. Antifouling Polymer Brushes Displaying Antithrombogenic Surface Properties. *Biomacromolecules* **2016**, *17*, 1179-1185.

(10) Pop-Georgievsk, O.; Rodriguez-Emmenegger, C.; Pereira, A. d. l. S.; Proks, V.; Brynda, E.; Rypáček, F. Biomimetic non-fouling surfaces: extending the concepts. *J. Mater. Chem. B* **2013**, *1*, 2859-2867.

(11) Alves, P.; Gomes, L. C.; M, M. V.; Rodriguez-Emmenegger, C.; Mergulhão, F. J. The potential advantages of using a poly(HPMA) brush in urinary catheters: effects on biofilm cells and architecture. *Colloids Surf., B* **2020**, *19*, 110976.

(12) Zhao, W.; ye, Q.; Hu, H.; Wang, X.; Zhou, F. Grafting zwitterionic polymer brushes via electrochemical surface-initiated atomic-transfer radical polymerization for anti-fouling applications. *J. Mater. Chem. B* **2014**, *2*, 5352-5357.

(13) Gao, X.; Kučerka, N.; Nieh, M.; Katsaras, J.; Zhu, S.; Brash, J. L.; Sheardown, H. Chain Conformation of a New Class of PEG-Based Thermoresponsive Polymer Brushes Grafted on Silicon as Determined by Neutron Reflectometry. *Langmuir* **2009**, *25*, 10271-10278.

(14) Advincula, R. C.; Brittain, W. J.; Caster, K. C.; Rühe, J. *Polymer Brushes: Synthesis, Characterization and Applications*; 2004.

(15) Szleifer, I. Protein adsorption on surfaces with grafted polymers: A theoretical approach. *Biophys. J.* **1997**, *72*, 595-612.

(16) Szleifer, I. Polymers and proteins: interactions at interfaces. *Curr. Opin. Solid State Mater. Sci.* **1997**, *2*, 337-344.

(17) Szleifer, I. Statistical thermodynamics of polymers near surfaces. *Curr. Opin. Solid State Mater. Sci.* **1996**, *1*, 416-423.

(18) Michalek, L.; Barner, L.; Barner-Kowollik, C. Polymer on Top: Current Limits and Future Perspectives of Quantitatively Evaluating Surface Grafting. *Adv. Mater.* **2018**, *30*, 1706321.

(19) Jesmer, A. H.; Huynh, V.; Wylie, R. G. Fabrication of low-fouling, high-loading polymeric surfaces through pH-controlled RAFT. *RSC Adv.* **2020**, *10*, 20302-20312.

(20) Emilsson, G.; Schoch, R. L.; Feuz, L.; Höök, F.; Lim, R. Y. H.; Dahlin, A. B. Strongly Stretched Protein Resistant Poly(ethylene glycol) Brushes Prepared by Grafting-To. *ACS Appl. Mater. Interfaces* **2015**, *7*, 7505-7515.

(21) Han, Y.; Cui, J.; Jin, J.; Jiang, W. Hydrogen bonding induced protein adsorption on polymer brushes: a Monte Carlo study. *J. Mater. Chem. B* **2017**, *5*, 8479-8486.

(22) Kim, M.; Schmitt, S. K.; Choi, J. W.; Krutty, J. D.; Gopalan, P. From Self-Assembled Monolayers to Coatings: Advances in the Synthesis and Nanobio Applications of Polymer Brushes. *Polymers* **2015**, *7*, 1346-1378.

(23) Wertz, C. F.; Santore, M. M. Fibrinogen Adsorption on Hydrophilic and Hydrophobic Surfaces: Geometrical and Energetic Aspects of Interfacial Relaxations. *Langmuir* **2002**, *18*, 706-715.

(24) Sun, M.; Deng, J.; Tang, Z.; Wu, J.; Li, D.; Chen, H.; Gao, C. A correlation study of protein adsorption and cell behaviors on substrates with different densities of PEG chains. *Colloids Surf., B* **2014**, *122*, 134-142.

(25) Liu, D.; Guo, J.; zhang, J. Chain mobility and film softness mediated protein antifouling at the solid–liquid interface. *J. Mater. Chem. B* **2016**, *4*, 6134-6142.

(26) Otsuka, H.; Nagasaki, Y.; Kataoka, K. Characterization of Aldehyde-PEG Tethered Surfaces: Influence of PEG Chain Length on the Specific Biorecognition. *Langmuir* **2004**, *20*, 11285-11287.

(27) Norde, W.; Gage, D. Interaction of Bovine Serum Albumin and Human Blood Plasma with PEO-Tethered Surfaces: Influence of PEO Chain Length, Grafting Density, and Temperature. *Langmuir* **2004**, *20*, 4162-4167.

(28) Wang, S.; Wang, Z.; Li, J.; Li, L.; Hu, W. Surface-grafting polymers: from chemistry to organic electronics. *Mater. Chem. Front.* **2020**, *4*, 692-714.

(29) Pino-Ramos, V. H.; Ramos-Ballesteros, A.; López-Saucedo, F.; López-Barriguete, J. E.; Varca, G. H. C.; Bucio, E. Radiation Grafting for the Functionalization and Development of Smart Polymeric Materials. *Top. Curr. Chem.* **2016**, *374*, 63.

(30) Bhosale, R. R.; Gangadharappa, H. V.; Moin, A.; Gowda, D. V.; Osmani, R. A. M. Grafting Technique with Special Emphasis on Natural Gums: Applications and Perspectives in Drug Delivery. *Nat. Prod. J.* **2015**, *5*, 124-139.

(31) Suresh, D.; Goh, P. S.; Ismail, A. F.; Hilal, N. Surface Design of Liquid Separation Membrane through Graft Polymerization: A State of the Art Review. *Membranes* **2021**, *11*, 832.

(32) Bousquet, A.; Awada, H.; Hiorns, R. C.; Dagron-Lartigau, C.; Billon, L. Conjugated-polymer grafting on inorganic and organic substrates: A new trend in organic electronic materials. *Prog. Polym. Sci.* **2014**, *39*, 1847-1877.

(33) Eck, G. C. R. v.; Chiappisi, L.; Beer, S. d. Fundamentals and Applications of Polymer Brushes in Air. *ACS Appl. Polym. Mater.* **2022**, *4*, 3062-3087.

(34) Svoboda, J.; Luisiani, N.; Sivkova, R.; Pop-Georgievski, O.; Sedlacek, O. Antifouling Properties of Poly(2-Oxazoline)s and Poly(2-Oxazine)s: Direct Comparison of Polymer-Coated Surfaces with the Same Coating Parameters. *Macromol. Rapid Commun.* **2023**, *44*, 2300168.

(35) Pop-Georgievski, O.; Popelka, Š.; Houska, M.; Chvostová, D.; Proks, V.; Rypáček, F. Poly(ethylene oxide) Layers Grafted to Dopamine-melanin Anchoring Layer: Stability and Resistance to Protein Adsorption. *Biomacromolecules* **2011**, *12*, 3232-3242.

(36) Popelka, Š.; Houska, M.; Havlíková, J.; Proks, V.; Kučka, J.; Šturcová, A.; Bačáková, L.; Rypáček, F. Poly(ethylene oxide) brushes prepared by the "grafting to" method as a platform for the assessment of cell receptor–ligand binding. *Eur. Polym. J.* **2014**, *58*, 11-22.

(37) Svoboda, J.; Sedláček, O.; Riedel, T.; Hrubý, M.; Pop-Georgievski, O. Poly(2-oxazoline)s One-Pot Polymerization and Surface Coating: From Synthesis to Antifouling Properties Out-Performing Poly(ethylene oxide). *Biomacromolecules* **2019**, *20*, 3453-3463.

(38) Pop-Georgievski, O.; Verreault, D.; Diesner, M.-O.; Proks, V.; Heissler, S.; Rypáček, F.; Koelsch, P. Nonfouling Poly(ethylene oxide) Layers End-Tethered to Polydopamine. *Langmuir* **2012**, *28*, 14273-14283.

(39) Roling, O.; Mardyukov, A.; Krings, J. A.; Studer, A.; Ravoo, B. J. Polymer Brushes Exhibiting Versatile Supramolecular Interactions Grown by Nitroxide-Mediated Polymerization and Structured via Microcontact Chemistry. *Macromolecules* **2014**, *47*, 2411-2419.

(40) Wei, W.; Balamurugan, A.; Dwyer, J. H.; Gopalan, P. Substrate-Independent Approach to Dense Cleavable Polymer Brushes by Nitroxide-Mediated Polymerization. *ACS Macro Lett.* **2018**, *7*, 100-104.

(41) Schmidt, A. C.; Turgut, H.; Le, D.; Beloqui, A.; Delaittre, G. Making the best of it: nitroxide-mediated polymerization of methacrylates via the copolymerization approach with functional styrenics. *Polym. Chem.* **2019**, *11*.

(42) Yamago, S.; Yahata, Y.; Nakanishi, K.; Konishi, S.; Kayahara, E.; Nomura, A.; Goto, A.; Tsujii, Y. Synthesis of Concentrated Polymer Brushes via Surface-Initiated Organotellurium-Mediated Living Radical Polymerization. *Macromolecules* **2013**, *46*, 6777-6785.

(43) Layadi, A.; Kessel, B.; Yan, W.; Romio, M.; Spencer, N. D.; Zenobi-Wong, M.; Matyjaszewski, K.; Benetti, E. M. Oxygen Tolerant and Cytocompatible Iron(0)-Mediated ATRP Enables the Controlled Growth of Polymer Brushes from Mammalian Cell Cultures. *J. Am. Chem. Soc.* **2020**, *142*, 3158-3164.

(44) Sivkova, R.; Svoboda, J.; Pánek, J.; Appelhans, D.; Pop-Georgievski, O. Polymer brushes based on N-methacryloxysuccinimide as platform for versatile post-polymerization modification. *Prog. Org. Coat.* **2023**, *178*, 107447.

(45) Ko, Y.; Truong, V. K.; Woo, S. Y.; Dickey, M. D.; Hsiao, L.; Genzer, J. Counterpropagating Gradients of Antibacterial and Antifouling Polymer Brushes. *Biomacromolecules* **2022**, *23*, 424-430.

(46) Yamamoto, S.; Ejaz, M.; Tsujii, Y.; Matsumoto, M.; Fukada, T. Surface Interactoin Forces of Well-Defined, High-Demsity Polymer Brushes Studies by Atomic Force Microscopy. 1. Effects of Chain Length. *Macromolecules* **2000**, *33*, 5602-5607.

(47) Yamamoto, S.; Ejaz, M.; Tsujii, Y.; Fukada, T. Surface Interactoin Forces of Well-Defined, High-Demsity Polymer Brushes Studies by Atomic Force Microscopy. 2. Effects of Grafting Density. *Macromolecules* **2000**, *33*, 5608-5612.

(48) Rodriguez-Emmenegger, C.; Schmidt, B. V. K. J.; Sedlakova, Z.; Šubr, V.; Alles, A. B.; Brynda, E.; Barner-Kowollik, C. Low Temperature Aqueous Living/Controlled (RAFT) Polymerization of Carboxybetaine Methacrylamide up to High Molecular Weights. *Macromol. Rapid Commun.* **2011**, *32*, 958-965.

(49) Zamfir, M.; Rodriguez-Emmenegger, C.; Bauer, S.; Barner, L.; Rosenhahn, A.; Barner-Kowollik, C. Controlled growth of protein resistant PHEMA brushes via S-RAFT polymerization. *J. Mater. Chem. B* **2013**, *1*, 6027-6034.

(50) Tischer, T.; Gralla-Koser, R.; Trouillet, V.; Barner, L.; Barner-Kowollik, C.; Lee-Thedieck, C. Direct Mapping of RAFT Controlled Macromolecular Growth on Surfaces via Single Molecule Force Spectroscopy. *ACS Macro Lett.* **2016**, *5*, 498-503.

(51) Kuzmyn, A. R.; Nguyen, A. T.; Teunissen, L. W.; Zuilhof, H.; Baggerman, J. Antifouling Polymer Brushes via Oxygen-Tolerant Surface-Initiated PET-RAFT. *Langmuir* **2020**, *36*, 4439-4446.

(52) Roeven, E.; Kuzmyn, A. R.; Scheres, L.; Baggerman, J.; Smulders, M. M. J.; Zuilhof, H. PLL-Poly(HPMA) Bottlebrush-Based Antifouling Coatings: Three Grafting Routes. *Langmuir* **2020**, *36*, 10187-10199.

(53) Kuzmyn, A. R.; van Galen, M.; van Lagen, B.; Zuilhof, H. SI-PET-RAFT in flow: improved control over polymer brush growth. *Polym. Chem.* **2023**, *14*, 3357-3363.

(54) Brittain, W. J.; Minko, S. A structural definition of polymer brushes. *J. Polym. Sci., Part A: Polym. Chem.* **2007**, *45*, 3505-3512.

(55) Hildebrandt, M.; Shin, E.; Yang, S.; Ali, W.; Altinpinar, S.; Gutmann, J. S. Investigation of Roughness Correlation in Polymer Brushes via X-ray Scattering. *Polymers* **2020**, *12*, 2101.

(56) Singh, M. K. Polymer Brush Based Tribology. In *Tribology in Materials and Applications.*, Katiyar, J., Ramkumar, P., Rao, T., Davim, J. Eds.; Springer, Cham., 2020; pp 15-32.

(57) chen, W.; Cordero, R.; Tran, H.; Ober, C. K. 50th Anniversary Perspective: Polymer Brushes: Novel Surfaces for Future Materials. *Macromolecules* **2017**, *50*, 4089-4113.

(58) Song, X.; Man, J.; Qiua, Y.; Wang, J.; Liu, J.; Li, R.; Zhang, Y.; Li, J.; Li, J.; Chen, Y. Design, preparation, and characterization of lubricating polymer brushes for biomedical applications. *Acta Biomater.* **2024**, *175*, 76-105.

(59) Wang, Y.; Kálosi, A.; Halahovets, Y.; Romanenko, I.; Slabý, J.; Homola, J.; Svoboda, J.; de los Santos Pereira, A.; Pop-Georgievski, O. Grafting density and antifouling properties of poly[N-

(2-hydroxypropyl) methacrylamide] brushes prepared by “grafting to” and “grafting from”. *Polym. Chem.* **2022**, *13*, 3815-3826.

(60) Kang, C.; Crockett, R.; Spencer, N. D. The influence of surface grafting on the growth rate of polymer chains. *Polym. Chem.* **2016**, *7*, 302-309.

(61) Patil, R. R.; Turgman-Cohen, S.; Šrogl, J.; Kiserow, D.; Genzer, J. On-Demand Degrafting and the Study of Molecular Weight and Grafting Density of Poly(methyl methacrylate) Brushes on Flat Silica Substrates. *Langmuir* **2015**, *31*, 2372-2381.

(62) Moh, L. C. H.; Losego, M. D.; Braun, P. V. Solvent Quality Effects on Scaling Behavior of Poly(methyl methacrylate) Brushes in the Moderate- and High-Density Regimes. *Langmuir* **2011**, *27*, 3698-3702.

(63) Mejis, G. F.; Rizzardo, E. Chain transfer by an addition-fragmentation mechanism. The use of α-benzyloxystyrene for the preparation of low-molecular-weight poly(methyl methacrylate) and polystyrene. *Macromol. Chem. Rapid. Commun.* **1988**, *9*, 547-551.

(64) Mejis, G. F.; Rizzardo, E.; Thang, S. H. Preparation of controlled-molecular-weight, olefin-terminated polymers by free radical methods. Chain transfer using allylic sulfides. *Macromolecules* **1988**, *21*, 3122-3124.

(65) Rizzardo, E.; Mejis, G. F.; Thang, S. H. Chain transfer by radical addition-fragmentation mechanisms: Synthesis of macromonomers and end-functional oligomers. *Macromol. Symp.* **1995**, *98*, 101-123.

(66) Cerda, M. M.; Newton, T. D.; Zhao, Y.; Collins, B. K.; Hendon, C. H.; Pluth, M. D. Dithioesters: simple, tunable, cysteine-selective H2S donors. *Chem. Sci* **2019**, *10*, 1773-1779.

(67) Lehnen, A.-C.; Gurke, J.; Bapolosi, A. M.; Reifarth, M.; Bekir, M.; Hartlieb, M. Xanthate-supported photo-iniferter (XPI)-RAFT polymerization: facile and rapid access to complex macromolecules. *Chem. Sci.* **2023**, *14*, 593-603.

(68) Moad, G. A Critical Survey of Dithiocarbamate Reversible Addition-Fragmentation Chain Transfer (RAFT) Agents in Radical Polymerization. *J. Polym. Sci., Part A: Polym. Chem.* **2019**, *57*, 216-227.

(69) Boyer, C.; Bulmus, V.; Davis, T. P.; Ladmiral, V.; Liu, J.; Perrier, S. Bioapplications of RAFT Polymerization. *Chem. Rev.* **2009**, *109*, 5402-5436.

(70) Pirrier, S. 50th Anniversary Perspective: RAFT Polymerization: A User Guide. *Macromolecules* **2017**, *50*, 7433-7447.

(71) Kalirajan, C.; Dukle, A.; Nathanael, A. J.; Oh, T.; Manivasagam, G. A Critical Review on Polymeric Biomaterials for Biomedical Applications. *Polymers* **2021**, *13*, 3015.

(72) Bagheri, A. Application of RAFT in 3D Printing: Where Are the Future Opportunities? *Macromolecules* **2023**, *56*, 1778-1797.

(73) Amorim, S.; Reis, C. A.; Reis, R. L.; Pires, R. A. Extracellular Matrix Mimics Using HyaluronanBased Biomateria. *Trends Biotechnol.* **2021**, *39*, 90-104.

(74) Rodriguez-emmenegger, C.; Janel, S.; Pereira, A. d. l. S.; Bruns, M.; Lafont, F. Quantifying bacterial adhesion on antifouling polymer brushes via single-cell force spectroscopy. *Polym. Chem.* **2015**, *6*, 5740-5751.

(75) Tsujii, Y.; Ejaz, M.; Sato, K.; Goto, A.; Fukuda, T. Mechanism and Kinetics of RAFT-Mediated Graft Polymerization of Styrene on a Solid Surface. 1. Experimental Evidence of Surface Radical Migration. *Macromolecules* **2001**, *34*, 8872-8878.

(76) K. Ulbrich; V. Šubr; J. Strohalm; D. Plocová; M. Jelínková; B. Říhová. Polymeric drugs based on conjugates of synthetic and natural macromolecules: I. Synthesis and physico-chemical characterisation. *J. Controlled Release* **2000**, *64*, 63-70.

(77) Kuzmyn, A. R.; Ypma, T. G.; Zuihof, H. Tunable Cell-Adhesive Surfaces by Surface-Initiated Photoinduced Electron-Transfer-Reversible Addition–Fragmentation Chain-Transfer Polymerization. *Langmuir* **2024**, *40*, 3354-3359.

(78) Kingshott, P.; Thissen, H.; Griesser, H. J. Effects of cloud-point grafting, chain length, and density of PEG layers on competitive adsorption of ocular proteins. *Biomaterials* **2002**, *23*, 2043-2056.

(79) Zhang, Z.; Corrigan, N.; Bagheri, A.; Jin, J.; Boyer, C. A Versatile 3D and 4D Printing System through Photocontrolled RAFT Polymerization. *Angew. Chem. Int. Ed.* **2019**, *58*, 17954-17963.

(80) Bainbridge, C. W. A.; Engel, K. E.; Jin, J. 3D printing and growth induced bending based on PET-RAFT polymerization. *Polym. Chem.* **2020**, *11*, 4084-4093.

(81) Zhang, Z.; Corrigan, N.; Boyer, C. Effect of Thiocarbonylthio Compounds on Visible-Light-Mediated 3D Printing. *Macromolecules* **2021**, *54*, 1170-1182.

(82) Lee, K.; Corrigan, N.; Boyer, C. Rapid High-Resolution 3D Printing and Surface Functionalization via Type I Photoinitiated RAFT Polymerization. *Angew. Chem. Int. Ed.* **2021**, *60*, 8839-8850.

(83) Brun, A. P. L.; Huang, T.; Pullen, S.; Nelson, A. R. J.; Spedding, J.; Holt, S. A. Spatz: the time-of-flight neutron reflectometer with vertical sample geometry at the OPAL research reactor. *J. Appl. Crystallogr.* **2023**, *56*, 18-25.

(84) James, M.; Nelson, A.; Holt, S. A.; Saerbeck, T.; Hamilton, W. A.; Klose, F. The multipurpose time-of-flight neutron reflectometer ‘‘Platypus’’ at Australia’s OPAL reactor. *Nucl. Instrum. Methods Phys. Res., Sect. A* **2011**, *632*, 112-123.

(85) Gresham, I. J.; Nurdoch, T. J.; Johnson, E. C.; Hobertson, H.; Webber, G. B.; Wanless, E. J.; Prescott, S. W.; Nelson, A. R. J. Quantifying the robustness of the neutron reflectometry technique for structural characterization of polymer brushes. *J. Appl. Cryst.* **2021**, *54*, 739-750.

(86) Goodman, D.; Kizhakkedathu, J. N.; Brooks, D. E. Evaluation of an Atomic Force Microscopy Pull-Off Method for Measuring Molecular Weight and Polydispersity of Polymer Brushes: Effect of Grafting Density. *Langmuir* **2004**, *20*, 6238-6245.

(87) Zimmermann, R.; Dukhin, S. S.; Werner, C.; Duval, J. F. L. On the use of electrokinetics for unraveling charging and structure of soft planar polymer films. *Curr. Opin. Colloid Interface Sci.* **2013**, *18*, 83-92.

(88) Zimmermann, R.; Osaki, T. Electrokinetic microslit experiments to analyse the charge formation at solid/liquid interfaces. *Microfluid. Nanofluid.* **2006**, *2*, 367-379.

(89) Zimmermann, R.; Kuckling, D.; Kaufmann, M.; Werner, C.; Duval, J. F. L. Electrokinetics of a Poly(N-isopropylacrylamid-co-carboxyacrylamid) Soft Thin Film: Evidence of Diffuse Segment Distribution in the Swollen State. *Langmuir* **2020**, *26*, 18169-18181.

(90) Pop-Georgievski, O.; Zimmermann, R.; Kotelnikov, I.; Proks, V.; Romeis, D.; Kučka, J.; Caspari, A.; Rypáček, F.; Werner, C. Impact of Bioactive Peptide Motifs on Molecular Structure, Charging, and Nonfouling Properties of Poly(ethylene oxide) Brushes. *Langmuir* **2018**, *34*, 6010-6020.

(91) Zimmermann, R.; Romeis, D.; Bihannic, I.; Stuart, M. C.; Sommer, J.-U.; Werner, C.; Duval, J. F. L. Electrokinetics as an alternative to neutron reflectivity for evaluation of segment density distribution in PEO brushes. *Soft Matter* **2014**, *10*, 7804-7809.

(92) Zimmermann, R.; Freudenberg, U.; Schweiß, R.; Küttner, D.; Werner, C. Hydroxide and hydronium ion adsorption — A survey. *Curr. Opin. Colloid Interface Sci.* **2010**, 196-202.

(93) Werner, C.; König, U.; Augsburg, A.; Arnhold, C.; Körber, H.; Zimmermann, R.; Jacobasch, H.-J. Electrokinetic surface characterization of biomedical polymers — a survey. *Colloids Surf., A* **1999**, *159*, 519-529.

(94) Zimmermann, R.; Birkert, O.; Gauglitz, G.; Werner, C. Electrosurface Phenomena at Polymer Films for Biosensor Applications. *ChemPhysChem* **2003**, *4*, 509-514.

(95) Zimmermann, R.; Norde, W.; Stuard, M. A. C.; Werner, C. Electrokinetic Characterization of Poly(Acrylic Acid) and Poly(Ethylene Oxide) Brushes in Aqueous Electrolyte Solutions. *Langmuir* **2005**, *21*, 5108-5114.

(96) Duval, J. F. L.; Zimmermann, R.; Cordeiro, A. L.; Rein, N.; Werner, C. Electrokinetics of Diffuse Soft Interfaces. IV. Analysis of Streaming Current Measurements at Thermoresponsive Thin Films. *Langmuir* **2009**, *25*, 10691-10703.

(97) Milner, S. T.; Witten, T. A.; Cates, M. E. Theory of the grafted polymer brush. *Macromolecules* **1988**, *21*, 2610-2619.

(98) Milner, S. T.; Witten, T. A.; Cates, M. E. Parabolic density profile for grafted polymers. *Europhys. Lett.* **1988**, *5*, 413-418.

(99) Milner, S. Polymer Brushes. *Science* **1991**, *251*, 905-914.

(100) Milner, S. T.; Witten, T. A.; Cates, M. E. Effects of polydispersity in the end-grafted polymer brush. *Macromolecules* **1989**, *22*, 853-861.

(101) Lowe, S.; O'Brien-Simpson, N. M.; Connal, L. A. Antibiofouling polymer interfaces: poly(ethylene glycol) and other promising candidates. *Polym. Chem.* **2015**, *6*, 198-212.

(102) Yamamoto, S.; Tsujii, Y.; Fukuda, T. Atomic force microscopic study of stretching a single polymer chain in a polymer brush. *Macromolecules* **2000**, *33* (16), 5995-5998.

(103) Al-Maawali, S.; Bemis, J. E.; Akhremitchev, B. B.; Leecharoen, R.; Janesko, B. G.; Walker, G. C. Study of the polydispersity of grafted poly(dimethylsiloxane) surfaces using single-molecule atomic force microscopy. *J. Phys. Chem. B* **2001**, *105*, 3965-3971.

(104) Zoppe, J. O.; Ataman, N. C.; Mocny, P.; Wang, J.; Moraes, J.; Klok, H.-A. Surface-Initiated Controlled Radical Polymerization: State-of-the-Art, Opportunities, and Challenges in Surface and Interface Engineering with Polymer Brushes. *Chem. Rev.* **2017**, *117*, 1105-1318.

(105) Pan, X.; Zhang, F.; Choi, B.; Luo, Y.; Guo, X.; Feng, A.; Thang, S. H. Effect of solvents on the RAFT polymerization of N-(2-hydroxypropyl) methacrylamide. *Eur. Polym. J.* **2019**, *115*, 166-172.

(106) Hamilton, W. A.; Smith, G. S.; Alcantar, N. A.; Majewski, J.; Toomey, R. G.; Kuhl, T. L. Determining the Density Profile of Confined Polymer Brushes with Neutron Reflectivity. *J. Polym. Sci. B Polym. Phys.* **2004**, *42*, 3209-3301.

(107) Rubinstein, M.; Colby, R. H. *Polymer physics*; Oxford University Press, 2003.

(108) Nelson, A. R. J.; Prescott, S. W. refnx: neutron and X-ray reflectometry analysis in Python. *J. Appl. Crystallogr.* **2019**, *52*, 193-200.

(109) Robertson, H.; Johnson, E. S.; Gresham, I. J.; Prescott, S. W.; Nelson, A.; Wanless, E. J.; Webber, G. B. Competitive specific ion effects in mixed salt solutions on a thermoresponsive polymer brush. *J. Colloid Interface Sci.* **2021**, *586*, 292-304.

(110) Riedelová, Z.; Pereira, A. d. l. S.; Svoboda, J.; Pop-Georgievski, O.; Májek, P. l.; Pečánková, K.; Dyčka, F.; Rodriguez-Emmenegger, C.; Riedel, T. The Relation Between Protein Adsorption andHemocompatibility of Antifouling Polymer Brushes. *Macromol. Biosci.* **2022**, *22*, 2200247.

(111) Wang, Y.; Zeng, G.; Jiang, Y. The Emerging Roles of miR-125b in Cancers. *Cancer Manage. Res.* **2020**, *12*, 1079-1088.

(112) Špringer, T.; Krejčík, Z.; Homola, J. Detecting attomolar concentrations of microRNA related to myelodysplastic syndromes in blood plasma using a novel sandwich assay with nanoparticle release. *Biosens. Bioelectron.* **2021**, *194*, 113613.

(113) Asadi-Eydivand, M.; Brown, T. C.; Bagheri, A. RAFT-Mediated 3D Printing of "Living" Materials with Tailored Hierarchical Porosity. *ACS Appl. Polym. Mater.* **2022**, *4*, 4940-4948.

(114) Zhang, Z.; Corrigan, N.; Boyer, C. A Photoinduced Dual-Wavelength Approach for 3D Printing and Self-Healing of Thermosetting Materials. *Angew. Chem. Int. Ed.* **2022**, *61*, e202114111.

(115) Buryi, M.; Babin, V.; Neykova, N.; Wang, Y.-M.; Remeš, Z.; Ridzoňová, K.; Dominec, F.; Davydova, M.; Drahokoupil, J.; Chertopalov, S. Changes to Material Phase and Morphology Due to High-Level Molybdenum Doping of ZnO Nanorods: Influence on Luminescence and Defects. *Materials* **2023**, *16*, 3294.

(116) Buryi, M.; Neykova, N.; Brik, M. G.; Wang, Y.; Remeš, Z.; Ridzoňová, K.; Babin, V.; Davydova, M.; Drahokoupil, J.; Chertopalov, S.; et al. Hydrothermally grown molybdenum doped ZnO nanorod arrays. The concept of novel ultrafast nanoscintillator. *Opt. Mater.* **2023**, *145*, 114445.

(117) Wiesmann, N.; Mendler, S.; Buhr, C. R.; Ritz, U.; Kämmerer, P. W.; Brieger, J. Zinc Oxide Nanoparticles Exhibit Favorable Properties to Promote Tissue Integration of Biomaterials. *Biomedicines* **2021**, *9*, 1462.

(118) Chong, W. J.; Shen, S.; Li, Y.; Trinchi, A.; Simunec, D. P.; Kyratzis, I.; Sola, A.; Wen, C. Biodegradable PLA-ZnO nanocomposite biomaterials with antibacterial properties, tissue engineering viability, and enhanced biocompatibility. *Smart Materials in Manufacturing* **2023**, *1*, 100004.

(119) Ringu, T.; Ghosh, S.; Das, A.; Pramanik, N. Zinc oxide nanoparticles: an excellent biomaterial for bioengineering applications. *Emergent Mater.* **2022**, *5*, 1629-1648.

(120) Weng, Z.; Xu, Y.; Gao, J.; Wang, X. Research progress of stimuli-responsive ZnO-based nanomaterials in biomedical applications. *Biomater. Sci.* **2023**, *11*, 76-95.

(121) Suryanarayanan, R. Zinc Oxide: From Optoelectronics to Biomaterial—A Short Review. In *ZnO Nanocrystals and Allied Materials*, Rao, M. S. R., Okada, T. Eds.; Springer India, 2014; pp 289-307.

(122) He, X.; Li, X.; Zhang, M.; Tian, B.; Sun, L.; Bi, C.; Deng, D.; Zhou, H.; Qu, H.; Wu, C.; et al. Role of molybdenum in material immunomodulation and periodontal wound healing: Targeting immunometabolism and mitochondrial function for macrophage modulation. *Biomaterials* **2022**, *283*, 121439.